Sperm Transport Mechanics in Female Yellow Dung Flies

Dissertation
zur
Erlangung der naturwissenschaftlichen Doktorwürde
(Dr.sc.nat.)
vorgelegt der
Mathematisch-naturwissenschaftlichen Fakultät
der
Universtät Zürich
von

Christian Wüst
aus Lupfig AG

Promotionskomitee
Prof. Dr. Stefan A. Sauter (Vorsitz), Institut für Mathematik, Universität Zürich
Prof. Dr. Wolf U. Blanckenhorn, Zoologisches Museum, Universität Zürich
Dr. Luc F. Bussière, School of Biological and Environmental Sciences, University of Stirling
Prof. Dr. Michel Chipot, Institut für Mathematik, Universität Zürich

Zürich, 2009

Abstract

The mechanisms regulating sperm transfer, storage, and use in insects are far from clear. Even in one of the most well-resolved systems for studying post-copulatory sexual selection, the yellow dung fly (*Scathophaga stercoraria*), the process of sperm transfer is not well understood. Our aim is to model the fluid dynamics of sperm flow in the reproductive tracts of female yellow dung flies to determine what aspects of female morphology may influence the flow of ejaculates.
We present a novel approach to simulate yellow dung fly sperm flow using computational fluid dynamics and numerical mathematics. We model fluid flow in a longitudinal section by solving the Stokes equations with finite elements using software specially developed for this problem. We then perform systematic parameter tests to investigate the geometric parameters duct length, duct width, duct wall roughness and duct curvature of influencing rates of ejaculate movement.
We realize one model refinement that we expect to lead to a more complete description of the transport process: the filament modelling. We apply a bead-spring model involving physical filament parameters that we determine in our analysis comparing stationary shapes of microphotographs to filament shapes resulting from simulations in a straight channel. We present an immersed boundary method based algorithm using finite elements which we implemented to simulate the modelled filament mechanics coupled to Stokes flow using the derived filament parameters.
In a laboratory experiment we validate the theoretically found results on duct length and duct width and discuss the indicated influences of duct wall roughness and duct curvature by counting sperm in the spermathecae after controlled matings. The results are used to propose future model refinements. We conclude the implications of our model and methods for research in sperm competition and sexual selection.

Zusammenfassung

Die Mechanismen, welche den Transfer, die Speicherung und den Einsatz von Spermien bei Insekten regulieren, sind alles andere als gründlich erforscht. Sogar in einem der meist untersuchten Systeme für nachkopulative sexuelle Selektion, in demjenigen der gelben Dungfliege (Scathophaga stercoraria), ist der Prozess der Spermienübertragung noch nicht vollständig bekannt. Unser Ziel ist, die Strömungsmechanik des Spermienflusses im Reproduktionstrakt von weiblichen gelben Dungfliegen zu modellieren, um zu bestimmen, welche Aspekte der weiblichen Morphologie den Fluss des Ejakulats beeinflussen können.
Wir modellieren den Strömungsfluss in einem Längsschnitt, indem wir Stokes-Gleichungen mit Finiten Elementen mit einer speziell für dieses Problem entwickelten Software lösen. Für dieses Modell führten wir systematische Parameter-Tests durch, um den Einfluss der geometrischen Parameter wie Länge, Weite, Wandbeschaffenheit und Krümmung des Reproduktionstrakts auf die Bewegung des Ejakulats zu erforschen.
Als ersten Schritt im Modellverfeinerungsprozess realisierten wir die Modellierung von Fäden. Wir verwendeten ein Kugel-Feder-Modell unter Einbezug physikalischer Faden-Parameter, welche wir in unserer Analyse des Vergleichs zwischen der stationären Geometrie auf Mikrofotografien und der Fadengeometrie aus Simulationen in einem geraden Kanal bestimmten. Zur mathematischen Beschreibung präsentieren wir eine problemangepasste Methode, basierend auf der Koppelungsmethode IBM (immersed boundary method) unter Verwendung von Finiten Elementen, welche wir implementierten, um die modellierte Fadenmechanik gekoppelt mit der Stokes Strömung mit abgeleiteten Faden-Parametern zu simulieren.
In einem Laborexperiment validierten wir die theoretischen Resultate betreffend Länge und Breite des Kanals und untersuchten die angedeuteten Einflüsse der Wandbeschaffenheit und der Krümmung des Kanals. Die Resultate können verwendet werden, um das präsentierte Modell weiter zu verfeinern und als Anstoss für eine Vielzahl weiterer Experimente und Forschung in den Bereichen *sperm competition* und *sexual selection*.

Acknowledgements

I would like to thank everybody who helped creating this multi-faceted project.
For the mathematical part, I would like to thank my adviser, Prof. Sauter, for his support, encouragement and always being the anchor, when I was lost in interdisciplinarity. Then I would like to thank Thomas Götz for inviting me to Kaiserslautern and introducing me to filament modelling and having lots of fruitful discussions. Thanks to Marco Buck, Daniel Peterseim and Anton Smolianski for feedback and help on validating the implementation. For the technical support I am much obliged to Carsten Rose and Phillip Thomann.
In biology, it was Luc Bussière who introduced me to the fascinating field of evolutionary biology. Thanks to a good friend and an amazing scientist for contributing lots of constructive ideas to this work. Thanks to Marco Demont and Claudia Buser for their help with the lab study. Without them this project never could have been a success. In addition, thanks to Wolf Blanckenhorn, Sonja Sbilordo and all other colleagues of the zoological museum. Finally I like to thank Paul Ward, who regrettably died last year, for initiating this thesis and for several discussions and support.
Last, but not least, I am deeply obliged to all my friends and to my family, who supported me all the time.

Table of Contents

Introduction

Charles Darwin (1859) proposed natural selection as a mechanism to explain the evolution of traits that promote survival and reproduction. In addition, he outlined a process that he called sexual selection (Darwin, 1859, 1871), which could account for traits that might seem maladaptive in the context of natural selection, but were nevertheless favoured because they provided an advantage during intrasexual competition for reproductive success. He acknowledged two main categories of sexual selection: intrasexual selection (often called male-male competition) features contests between individuals within a sex (usually males) for access to members of the other sex (usually females), while intersexual selection (often called female choice) arises because mate choice by members of one sex (usually females) favours certain trait combinations in the other sex (usually males) (Andersson, 1994). Whereas much of the early research on sexual selection focused on traits that improve premating performance for both intra- and intersexual selection, the recognition that sexual selection continues after mating has stimulated much research on the mechanisms and consequences of *sperm competition* (the competition between sperm for the fertilization of ova, Parker (1970a) and *cryptic female choice* (any female-controlled trait or process that influences the outcome of sperm competition, Eberhard (1996)).

In spite of this research focus, the evolutionary consequences of postcopulatory sexual selection remain poorly resolved. This is partly because, unlike premating sexual selection, many of the crucial events are concealed within the reproductive tracts of females and therefore less amenable to direct observation and manipulation. In addition, postcopulatory sexual selection involves several individuals (i.e., a female and at least two competing males), each of which may have multiple interests in the outcome of selection that may or may not be congruent with the interests of the others. These competing interests interact in complex ways, and there are numerous examples of manipulative interactions in which behaviours or structures in one individual have come about in part via manipulation by another individual (Arnqvist and Rowe, 2005; Blanckenhorn et al., 2007). As a consequence, disentangling the selective basis and functional significance of traits that may have evolved in the context of postcopulatory sexual selection is difficult, even in very well studied systems. There is a clear need for studies of the mechanisms mediating the outcome of reproductive interactions, and for any theoretical work which can clarify the most productive avenues for such research.

The yellow dung fly (*Scathophaga stercoraria*) is a model system for research on post-copulatory sexual selection since the early 1970s (Parker, 1970a,b). Males congregate on dung pats to which gravid females are attracted for the purpose of oviposition (Parker, 1970b), and compete to copulate with these females. Although females do not appear to have any significant control over the identity of their mates at the oviposition resource (Parker, 1970a,b), they do seem to retain

some degree of control over insemination (Hosken et al., 2001). Females assist sperm movement from the intromittent organs to the primary site of sperm storage, as evidenced by experiments featuring female anesthesia (Bernasconi and Hellriegel, 2002) and radiolabelling techniques (Simmons et al., 1999). More intriguingly, females appear to be able to sort sperm in their multiple sperm storage organs (Bussière et al, in review, Demont et al, unpublished) perhaps in order to manipulate the paternity of their offspring depending on the predicted environmental conditions larvae will face (Ward, 2000, 2007).

Although there is strong selection on males to achieve insemination success, (Parker, 1970a;

Figure 1: A male yellow dung fly (source: digital-nature-photography.com).

Parker and Simmons, 1991; Simmons and Parker, 1992; Parker and Simmons, 1994; Simmons et al., 1999), there is nevertheless considerable variation in the relationship between male traits and success in paternity (Simmons and Siva-Jothy, 1998). Such variation might be partly attributable to female adaptations designed to retain control over sperm movement (Hosken et al., 1999; Arthur et al., 2008). For example, Hosken et al. (1999) have suggested that the convoluted nature of the spermathecal ducts may serve to restrict sperm movement to the spermathecae and thus assist female control over insemination success. Similarly, the curvature of ducts, acting in concert with the spermathecal invagination (Hosken and Ward, 2000) may play a prominent role in female mediated sperm transport by changing the rates of sperm flow in curved ducts relative to straightened ones. Documenting the role of these putative adaptations for controlling sperm flow is made difficult both by the small scale of the structures involved and by the potential interactions between males and females that might influence the outcome of sexual interactions.

In **Chapter 1** we fully derive the Navier-Stokes equations as they govern fluid flow based on a set of assumptions. We give a complete analysis of parameters and mathematical treatment of these equations and deduce the problem to solve to simulate sperm flow. Once the governing system of differential equations is stated, the approach of mixed variational problems and the numerical method of finite elements are introduced to solve the discretized problem. We implemented custom the software BioJCFD (Wüst, 2009) that implements the derived governing method. We give an overview of features and programming concepts of this simulation software.

The project in **Chapter 2** presents the first approach we made to model the sperm flow of the yellow dung fly: we describe fluid flow of a homogeneous fluid in a two-dimensional longitudinal cross-section of a dung fly duct. Although we model the real situation only roughly, we sharply deduce a list of assumptions and simplifications that we made compared to the real situation. We perform systematic parameter tests to find the effect sizes of duct length, duct width, duct wall

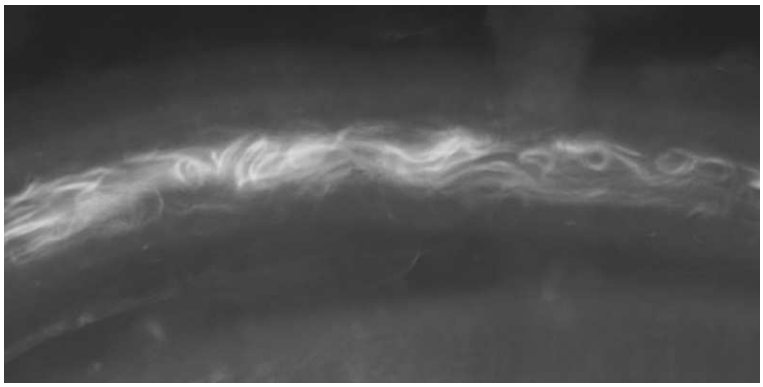

Figure 2: Cross section of a spermathecal duct with sperm filaments (source: Sonja Sbilordo, Zürich).

roughness and duct curvature to the flow rate of the seminal fluid. The results guide to further model refinements if the present model fails being validated.
As one major model refinement we present the modelling of individual sperm filaments in the seminal fluid. Since the sperm filaments are thin but very long (about a third of the total duct length), the effect of individually modelled interacting filaments compared to a homogeneous compound may play an important role in sperm displacement. We therefore derive the model of a flexible filament in **Chapter 3**. The governing forces are motivated and described. A method is presented to estimate the resistance to stretching and bending given a viscous coefficient.
Chapter 4 presents a method to model the fluid dynamics of a single immersed filament flowing through the spermathecal duct. The filament mechanics are coupled to the flow equations using the immersed boundary technique. After deducing all the parameters for the simulation, we approach the question of the influence of the presence of a single filament by repeating the meaningful tests of Chapter 2.
To control the appropriateness of the computational simulations we present an empirical laboratory experiment in **Chapter 5**. We mate male yellow dung flies with three non-sibling females each for 20 minutes. Then we measure all morphological parameters and the number of sperm in each spermathecae. From the distribution of the sperm over the spermathecae tested against the measured morphology, we get insight in the effect of the parameters in this real situation. We compare the results to those of Chapter 2, discuss model differences and suggest other putative mechanisms motivated by the results being candidates for further model refinements. From the nesting of our design we deduce the effects in a variance component analyze.
The conclusions of **Chapter 6** consist of new consolidated findings about the process of sperm displacement in yellow dung flies implied by the computational simulation and its empirical validation. We discuss advantages and limitations of the approach of using computational mathematics to model the fluid dynamics of yellow dung fly sperm flow.

Reading guidelines

Since several different scientific fields are part of this project the reader may consider the following note. There are mathematical parts and biological parts using their jargon. The goal is not to present a text that is readable with no precognitions. Besides giving the main ideas in an introduction, in every such part there are references to sources for interested readers from other fields.

1

Basics and Tools

For a computer-based flow simulation one needs concrete equations that govern the flow. The procedure is to commit oneself to a set of laws and assumptions, so that the resulting, simplified fluid flow can entirely be described with mathematical equations. We deduce such equations from physical laws and introduce the mathematical and numerical methods ensuring the existence of a computational, unique solution for the use in an algorithm realised in the implementation.

1.1 Physical Derivation of the governing Flow Equations

1.1.1 Derivation of the Navier-Stokes Equations

Let $\Omega \in \mathbb{R}^d$ a domain occupied with a fluid. Fluids are divided in *liquids* and *gases* where the main difference considering material properties is their compressibility. The shape of Ω may depend on time. On a molecular scale the mass of the material of a fluid is far from being smeared uniformly over the occupied volume. We shall however suppose that the macroscopic behaviour is the same as if they were perfectly continuous in structure and quantities as mass and momentum will be regarded spread uniformely over that volume. This assumption is called *continuum hypothesis* and is very common in fluid modelling.

The Material Derivative

Let us consider a single fluid particle in a steady flow field at position x_0. This material element may experience an acceleration through moving to a position where the fluid velocity u is different. Then $\partial u/\partial t$ is *not* the acceleration of that particle at position x_0 and time t, because the particle is at that position only instantaneously.
Considering δt small, we find by Taylor expansion

$$\delta u = u\left(x_0 + u\delta t, t + \delta t\right) = u(x_0, t) + \delta t \left(\frac{\partial u}{\partial t} + \left(u \cdot \nabla\right) u\right) + O\left(\delta t^2\right). \tag{1.1}$$

It follows the particle acceleration is composed by a *local rate* $\partial u/\partial t$ and a *convective rate* $(u \cdot \nabla)\, u$. The acceleration of a fluid element at (x, t) is

$$a(u,t) = \frac{\partial u}{\partial t} + (u \cdot \nabla)\, u.$$

Definition 1.

$$\frac{D}{Dt} := \frac{\partial}{\partial t} + (u \cdot \nabla)$$

is the material derivative.

The Reynolds Transport Theorem

The material derivative is orientated to the material while the local derivative is spatially orientated. One has to distinguish two frames of reference.

Lagrangian specification The Lagrangian specification is the material oriented frame where mass is considered as moving particles. The description of the fluid is always relative to the fluid. The focus is as sitting on a particle.

Eulerian specification In the Eulerian specification one has a spatially fixed external viewpoint. The fluid is considered as a spatial distribution of fluid quantities.

In our derivation theory we express the laws in Lagrangian specification. An elegant way to transform these formulations into the Eulerian frame is given by the Reynolds Transport Theorem:

Theorem 1. *Let $\Omega(t)$ be an arbitrary fluid material volume and $F(x,t)$ a scalar or vector function of position and time. If*

$$\int_{\Omega(t)} F(x,t) d\Omega$$

is well-defined, it follows that

$$\begin{aligned} \frac{D}{Dt}\int_{\Omega(t)} F(x,t) d\Omega &= \int_{\Omega(t)} \left(\frac{DF}{Dt} + F \nabla div u \right) d\Omega \qquad (1.2) \\ &= \int_{\Omega(t)} \left(\frac{\partial F}{\partial t} + div(uF) \right) d\Omega. \qquad (1.3) \end{aligned}$$

Proof. Let define the map from the domain in the Eulerian frame Ω_0 to the Lagrangian domain $\Omega(t)$. J is the functional determinant of the map. Transforming the left hand side of (1.2) we get

$$\frac{D}{Dt}\int_{\Omega(t)} F(x,t) d\Omega = \int_{\Omega_0} \frac{D}{Dt}(FJ) d\Omega_0$$

After using the product rule we transform the sum back

$$\begin{aligned} \int_{\Omega_0} \frac{D}{Dt}(FJ) d\Omega_0 &= \int_{\Omega_0} \left(\frac{DF}{Dt} J + F \frac{DJ}{Dt} \right) d\Omega_0 \\ &= \int_{\Omega_0} \left(\frac{DF}{Dt} + F \mathrm{div} u \right) J d\Omega_0 \\ &= \int_{\Omega(t)} \left(\frac{DF}{Dt} + F \mathrm{div} u \right) d\Omega_t. \end{aligned}$$

This proves the first part. The second equation we proof by using the definition of the material derivative and the divergence theorem

$$\begin{aligned}\int_{\Omega(t)} \left(\frac{DF}{Dt} + F\text{div}u\right) d\Omega_t &= \int_{\Omega(t)} \left(\frac{\partial F}{\partial t} + u \cdot \nabla F + F\text{div}u\right) d\Omega_t \\ &= \int_{\Omega(t)} \left(\frac{\partial F}{\partial t} + \text{div}(uF)\right) d\Omega. \quad \square\end{aligned}$$

The Conservation of Mass

Consider a closed surface A (fixed in position) which encloses a volume Ω entirely occupied by a fluid. In absence of fluid sources the mass of the fluid is conserved. This can be expressed by

$$\frac{d}{dt}\int_\Omega \rho d\Omega = -\int_A \rho u \cdot n dA, \tag{1.4}$$

where $\rho = \rho(x,t)$ is the fluid density and n the unit outward normal. The left hand side of (1.4) describes the change of the mass of enclosed fluid by A. The right hand side of (1.4) is the negative net rate at which mass is flowing out across A. This two quantities have to be equal in order to conserve mass. We transform (1.4) to a simpler equation. For the left hand side we use the chain rule to find

$$\begin{aligned}\frac{d}{dt}\int_\Omega \rho d\Omega &= \frac{\partial}{\partial t}\int_\Omega \rho d\Omega + \frac{\partial}{\partial x}\int \rho d\Omega \, \frac{\partial x}{\partial t} \\ &= \int_\Omega \frac{\partial}{\partial t}\rho d\Omega.\end{aligned}$$

In the last step we used that the Volume Ω is fixed in time. We apply the Gauss Theorem on the right hand side and get

$$\int_\Omega \frac{\partial}{\partial t}\rho d\Omega = -\int \text{div}(\rho u) d\Omega$$

and hence Ω was arbitrary

$$\frac{\partial \rho}{\partial t} + \text{div}(\rho u) = 0. \tag{1.5}$$

Equation (1.5) is known as *continuity equation* or *mass-conservation equation*.
If the density of a fluid is constant it is call *incompressible*. The continuity equation then simplifies to

$$\text{div}(u) = 0.$$

Under usual conditions liquids are in general incompressible. Gas flows are usually compressible but at low speeds assuming incompressibility can yield a good approximation.

The Conservation of Momentum

Newtons second law formulates that the change of momentum is equal to the sum of applied forces. We can write this as

$$\frac{D}{Dt}\int_\Omega \rho u dx = F_V + F_S, \tag{1.6}$$

where F_V denotes the *volume forces* and F_S the *surface forces* acting on the fluid.
Volume forces such as gravity are proportional to the fluid density and can be described as

$$F_V = \int_\Omega \rho f_V dx.$$

Surface forces act on surfaces and are proportional to the surface area. The force on the surface is composed to a product of the so called *stress tensor* $\sigma \in \mathbb{R}^{d\times d}$ and the unit outward normal n. With the Gauss Theorem we find

$$\begin{aligned} F_S = \int_\Omega f_S dx &= \int_\Omega \tau n dx \\ &= \int_\Omega \mathrm{div}(\tau) dx. \end{aligned} \tag{1.7}$$

The stress tensor σ contains an isotropic part $-pI$, where p is the hydrostatic pressure, and a viscous part τ given by

$$\tau = \lambda \mathrm{div}(u) I + 2\mu D(u),$$

where $\lambda := -\frac{2}{3}\mu$ is the *bulk viscosity*, μ the *dynamic viscosity* and $D(u) := \frac{1}{2}\left(\nabla u + \nabla u^T\right)$ the *rate of strain tensor*. For the stress tensor we get

$$\sigma = -pI + \lambda \mathrm{div}(u) I + 2\mu D(u).$$

Fluids that fit the approach of linear stress-strain dependence assumed in (1.1.1) are called *Newtonian fluids*. Gases and low molecular-weight liquids are Newtonian fluids.
For replacing the stress tensor in (1.7) we must compute divergence of the stress tensor.

$$\begin{aligned} \sigma_{ij} &= -p\delta_{ij} + \lambda \mathrm{div}(u)\delta_{ij} + 2\mu\left[\frac{1}{2}\left(\frac{\partial u_i}{\partial x_j} + \frac{\partial u_j}{\partial x_i}\right)\right] \\ \frac{\partial \sigma_{ij}}{\partial x_j} &= -\frac{\partial p}{\partial x_j}\delta_{ij} + \lambda \frac{\partial \mathrm{div}(u)}{\partial x_j}\delta_{ij} + 2\mu\left[\frac{1}{2}\left(\frac{\partial u_i}{\partial x_j} + \frac{\partial u_j}{\partial x_i}\right)\right] \\ \left(\mathrm{div}(\sigma)\right)_i &= -\frac{\partial p}{\partial x_j} + \lambda \frac{\partial \mathrm{div}(u)}{\partial x_j} + \mu \triangle u_i + \mu \frac{\partial \mathrm{div}(u)}{\partial x_i}. \end{aligned}$$

Replacing λ and using vector notation yields the following expression

$$\mathrm{div}(\sigma) = -\nabla p + \frac{\mu}{3}\nabla \mathrm{div}(u) + \mu \triangle u.$$

In order to simplify the left hand side of (1.6), we introduce a differentiated form. Using the Transport Theorem we get

$$\begin{aligned} \frac{D}{Dt}\int_\Omega \rho u d\Omega &= \int_\Omega \frac{D(\rho u)}{Dt} + (\rho u)\mathrm{div}(u) d\Omega \\ &= \int_\Omega \frac{D\rho}{Dt}u + \rho\frac{Du}{Dt} + (\rho u)\mathrm{div}(u) d\Omega \\ &= \int_\Omega -(\rho u)\mathrm{div}(u) + \rho\frac{Du}{Dt} + (\rho u)\mathrm{div}(u) d\Omega \\ &= \int_\Omega \rho\frac{Du}{Dt}. \end{aligned}$$

The differentiated form of Equation (1.6) is thus

$$\rho\frac{Du}{Dt} = \rho f_V - \nabla p + \frac{\mu}{3}\nabla\mathrm{div}(u) + \mu\triangle u. \tag{1.8}$$

This is the *conservation of momentum equation*. An alternative form is obtained by dividing by ρ and introducing the *kinematic viscosity* $\nu := \mu/\rho$

$$\frac{Du}{Dt} = f_V - \frac{1}{\rho}\nabla p + \frac{\nu}{3}\nabla\mathrm{div}(u) + \nu\triangle u. \tag{1.9}$$

In the incompressible case the density is no longer an unknown and the system is complete by $d+1$ equations and $d+1$ unknowns. In the compressible case we have one additional unknown. Therefore another conservation constraint is required. We will use the incompressible equations so we give the remaining conservation law only as a result. For a complete derivation see Baccetti et al. (1970).

The Conservation of Energy

The conservation of energy is governed by

$$\rho c_p\frac{DT}{Dt} = \beta T\frac{Dp}{Dt} + \psi + \mathrm{div}(k\nabla T) + \rho q, \tag{1.10}$$

where

c_p	is the specific heat at constant pressure,
$T(x,t)$	the temperature,
β	the volume thermal expansion coefficient,
ψ	the dissipation,
k	the heat conduction coefficient,
q	the internal heat production.

Using $T(x,t)$ we have another unknown. To balance the system we assume the law of perfect gas

$$p = p(\rho, T) = \rho RT. \tag{1.11}$$

The compressible Navier-Stokes Equations

The complete system of the compressible Navier-Stokes equations are given by

$$\begin{aligned}
\frac{\partial\rho}{\partial t} + \mathrm{div}(\rho u) &= 0\\
\rho\frac{Du}{Dt} &= \rho f_V - \nabla p + \frac{\mu}{3}\nabla\mathrm{div}(u) + \mu\triangle u\\
\rho c_p\frac{DT}{Dt} &= \beta T\frac{Dp}{Dt} + \psi + \mathrm{div}(k\nabla T) + \rho q\\
p = p(\rho, T) &= \rho RT,
\end{aligned}$$

where the unknowns are

$u(x,t)$	velocity
$p(x,t)$	pressure
$\rho(x,t)$	density
T	temperature

To make it a mathematically well-posed problem we add canonical *boundary conditions*

$$\begin{array}{l} u = 0 \\ T = T_b \end{array} \quad \text{on } \partial\Omega,$$

and *initial conditions*

$$\begin{array}{l} \rho(0) = \rho_0 \\ u(0) = u_0 \\ T(0) = T_0 \end{array} \quad \text{in } \partial\Omega.$$

Beside the use of the standard type of boundary and initial conditions, this is the general form of the compressible Navier-Stokes equations. From this general formulation multiple special cases can be derived. We shortly discuss the *stationary* case and the *inviscid* case and set our focus on the *incompressible* case which we use in further model descriptions.
The criterion whether a problem is time-dependent or stationary is mostly a question of the specification. Modelling a ship driving in the ocean at constant speed can either be described from the shore as time-dependant (Eulerian specification) or from the boat as a stationary problem (Lagrangian specification). However to solve a time-dependent problem one requires much more mathematical methodology.
The inviscid case leads to a first order PDE called *Euler equations*. Its steady, incompressible case leads to potential flow $u = \nabla\Psi$ and the problem is reduced to the Laplace problem $\triangle u = 0$.

The incompressible Navier-Stokes Equations

If we assume the density to be constant the equations reduce to

$$\begin{aligned} \operatorname{div}(u) &= 0 && (1.12) \\ \rho\frac{Du}{Dt} &= \rho f_V - \nabla p + \mu\triangle u, && (1.13) \end{aligned}$$

where the unknowns are

$$\begin{array}{ll} u(x,t) & \text{velocity} \\ p(x,t) & \text{pressure} \end{array}.$$

Again we add suitable *boundary conditions*

$$u = 0 \quad \text{on } \partial\Omega,$$

and *initial conditions*

$$u(0) = u_0 \quad \text{in } \partial\Omega.$$

Since the density is constant and known, we do not need the energy conservation constraint. The energy equation decouples and can be solved separately if needed. The energy is, as typically for viscous flows, monotonically decreasing due the friction loss due to viscosity.

Dividing (1.13) by the fluid density ρ and replacing the material derivative, we can rewrite the Navier-Stokes equations to another common form:

$$\frac{\partial u}{\partial t} - \nu \triangle u + (u \cdot \nabla)u + \frac{1}{\rho}\nabla p = f. \tag{1.14}$$

Before we derive the custom equations for our fly model system, we describe the involved parameters in detail. For the simulations we require concrete values for all fluid property quantities. This is the interface between the mathematical model and the application.

1.1.2 Physical Quantities in the Navier-Stokes Equations

In this section we describe all quantities appearing in the incompressible Navier-Stokes equations. As derived in the previous section, incompressible fluid flow is described by

$$\begin{aligned} \frac{\partial u}{\partial t} - \nu \triangle u + (u \cdot \nabla) u + \frac{1}{\rho} \nabla p &= f \text{ in } \Omega \\ \operatorname{div} u &= 0 \text{ in } \Omega. \end{aligned} \tag{1.15}$$

We group the quantities appearing in (1.15) into initial quantities required to start the simulation and unknown quantities that result as the solution of the problem from the simulation.

Initial Quantities

symbol	name	SI unit	common units	description
μ	dynamic viscosity	$kg/(m \cdot s)$	$1\ poise := 1\ g/(cm \cdot s)$	The (dynamic) viscosity can be thought of as an internal friction.
ν	kinematic viscosity	m^2/s	$1\ stokes := 1\ cm^2/s$	ν is the viscosity relative to the density ($\nu = \mu/\rho$).
ρ	density	kg/m^3	$1\ kg/l = 1\ g/cm^3$	The density is the mass per volume ratio.
f	forces	$m \cdot kg/s^2$	$1\ N := 1\ m \cdot kg/s^2$	f denotes all the forces acting on the fluid. Typical forces are gravity or electromagnetic forces.
v_{inflow}	inflow velocity	m/s		The inflow is given as a vector field defining direction and length of the velocity on the specified parts of the boundary.
v_{initial}	initial velocity	m/s		This is the velocity field on the complete domain at time $t = 0$.

Unknown Quantities

symbol	name	SI unit	common units	description
$u(x,t)$	velocity	m/s		The velocity is one part of the solution of (1.15). It denotes the velocity (as a vector) depending on the position and the time.
$p(x,t)$	pressure	$kg/(m \cdot s^2)$	$1Pa := 1N/m^2$	The pressure is the other part of a solution of (1.15). The pressure is a scalar value depending on position and time.

The main task of the simulation software is to solve a problem of the form

Problem 1. *Given a set of initial conditions (involving initial quantities) and boundary conditions, find a solution* $(u(x,t), p(x,t))$ *of system (1.15).*

Initial and boundary conditions will be described in detail in Section 1.2. Before we complete the formulation of the problem by introducing the mathematical model, we give an overview to flow characteristics from the fluid dynamics point of view and its connection to the derived equations.

1.1.3 Flow Characterisation

The difference of the flow behaviour of two systems (e.g. water flow and honey flow while stirring in a cup) has a big influence on the mathematical and numerical models to be used. Therefore it is important to have a precise knowledge of the Reynolds number, a flow characterisation parameter that we introduce in this section. The viscosity is one of its determining factors.

Viscosity

Imagine two plates and a fluid between them. Moving the upper plate, a shear stress is exerted on the fluid. Viscosity is a measure of the resistance of a fluid which is being deformed by such stress. Viscosity can be viewed as the thickness of a fluid or the fluid friction describing the resistance of a fluid to flow. Where air, gases and water are thin, having a low viscosity, motor oil, ketchup and honey are very thick, viscous fluids.

Example 1. *Knowing the dynamic viscosity and the density of water at 20 degrees, we get*

$$\nu_{water} = \frac{\mu_{water}}{\rho_{water}} \approx \frac{1\ centiPoise}{1\ g/ml} = \frac{0.01\ g/cm \cdot s}{1\ g/cm^3} = 0.01\ cm^2/s = 0.01\ stokes.$$

The following fluids are more viscous than water:

$$\begin{aligned} \nu_{olive\ oil} &\approx \frac{81\ centiPoise}{0.9\ g/ml} = 0.9\ stokes, \\ \nu_{honey} &\approx \frac{1000\ Poise}{1.4\ g/ml} = 714\ stokes, \\ \nu_{rt} &\approx \frac{10\ centiPoise}{1\ g/ml} = 0.1\ stokes, \end{aligned}$$

where ν_{rt} denotes the viscosity of the seminal fluid in the reproductive tract of the female yellow dung fly (which we model later).

The Reynolds Number

Definition 2. *The Reynolds-Number is defined as*

$$Re = \frac{L \cdot U}{\nu}, \tag{1.16}$$

where ν is the kinematic viscosity of the fluid, L is a characteristic length and U a characteristic velocity of the system. One common chioce for U is the average inflow velocity. The representation of the characteristic length L is not so obvious. A common choice is the average diameter of the flow domain.

It follows that the Reynolds number has no dimension. Viscosity is reciprocally proportional to the Reynolds number: Flow at high Reynolds numbers mean low viscosity. Very viscous fluids lead (in the same system) to flows at low Reynolds numbers. Moreover, the Reynolds number denotes an objective value for the flow behaviour of a system. Whenever two systems have same Reynolds numbers the flow behaviour is exactly the same. There is a bound that divides the flow behaviour in two characteristic flow types: At bigger Reynolds numbers, we have to deal with chaotic, stochastic property changes and vortices (turbulent flow), where at lower Reynolds numbers we the fluid flows in parallel layers (laminar flow). For pipe flow as discussed in this thesis, this bound is known to be approximately 2300.

Example 2. *Imagine we have water flowing through a pipe with diameter* $10\ cm$ *at a speed of* $1\ cm/s$. *Now we are putting an obstacle into the pipe. The Reynolds number of this system is*

$$Re = \frac{L \cdot U}{\nu} = \frac{10\ cm \cdot 1\ cm/s}{0.01\ stokes} = \frac{10\ cm \cdot 1\ cm/s}{1\ cm^2/s} = 0.1. \tag{1.17}$$

We conclude that this flow is strongly laminar and we do not expect any vortices in our pipe. Suppose we are interested in creating a system with exactly the same flow behaviour but with olive oil flowing through the pipe. What changes lead to the same Reynolds number? Freezing the Reynolds number at 0.1 and raising the viscosity from 0.01 stokes (water) to 0.9 stokes (olive oil), we have two choices: Either we increase the diameter of the pipe (and the obstacle) by the factor 90 to $9\ m$, *or increasing the speed of the fluid by factor 90 to* $90\ cm/s$. *On the other hand letting the fluid be the same in two different pipes, one as described above and one say with diameter* $1\ \mu m$, *the flow behaviour is totally different, since the Reynolds numbers are different.*
Finally we get back to the water calculation example (1.17). Where can water flow to be expected more chaotic, in a small or in a big system? Can flowing water ever get turbulent? We make the calculation for a really big ship in a channel (where one can observe vortices). This flow is highly turbulent:

$$Re = \frac{L \cdot U}{\nu} = \frac{50\ m \cdot 10\ m/s}{0.01\ stokes} = \frac{50000\ cm \cdot 10000\ cm/s}{1\ cm^2/s} = 5 \cdot 10^8. \tag{1.18}$$

Parameters of the Fly Model System

For a homogeneous representation of the fluid we present the estimated parameters in this section. For details on how we found them see Section (2.3). The parameters for the filaments simulations are presented in Chapter 3.

Model parameter	Estimated quantity
density (ρ)	$1\ g/cm^3$
dynamic viscosity (μ)	$0.1\ poise$
kinematic viscosity (ν)	$10^7\ \mu m^2/s$
inflow velocity (U)	$2\ \mu m/s$

Table 1.1: Estimated physical quantities for dung fly seminal fluid. The values are either deduced from other species or approximated by measurements described in Chapter 2

According to the definition (1.16) we get for the Reynolds-number

$$\mathrm{Re} = \frac{L \cdot U}{\nu} = \frac{13.5 \cdot 2}{10^7} \approx 10^{-6}. \tag{1.19}$$

The fact that the Reynolds-number is that small simplifies the mathematical modelling of the sperm flow. To see this, the equations are scaled to be non-dimensional. In the next section we follow that steps to find the governing equations for dung fly sperm flow.

1.2 Mathematical Model

Stating a mathematical problem means to choose the governing equations in a suitable form, equip them with boundary and initial conditions and find the proper function spaces for the solution making the problem uniquely solvable. Our aim is to end up with a mathematical problem that describes the flow of the seminal fluid.

1.2.1 Nondimensionalization

In order to simplify, we transform the derived equation system to a nondimensional form. We introduce dimensionless reference values according to characteristic problem quantities:

$$\begin{aligned} x &= L\tilde{x} \\ u &= U\tilde{u} \\ t &= \frac{L}{U}\tilde{t} \\ \rho &= \rho_r\tilde{\rho} \\ p &= \rho_r U^2\tilde{p}. \end{aligned}$$

Replacing the original variables in (1.13), we get

$$\begin{array}{rccccccccc} & \frac{\partial U\tilde{u}}{\partial\tilde{t}} & - & \nu\triangle_x U\tilde{u} & + & (U\tilde{u}\cdot\nabla)U\tilde{u} & + & \frac{1}{\rho}\nabla_x(\rho_r U^2\tilde{p}) & = & f \\ \Leftrightarrow & U\frac{\partial\tilde{u}}{\partial\tilde{t}}\frac{\partial\tilde{t}}{\partial t} & - & U\nu\triangle_{\tilde{x}}\tilde{u}\left(\frac{\partial\tilde{x}}{\partial x}\right)^2 & + & U^2(\tilde{x}\cdot\nabla)\tilde{u}\frac{\partial\tilde{x}}{\partial x} & + & \frac{\rho_r U^2}{\rho}\nabla_{\tilde{x}}\tilde{p}\frac{\partial\tilde{x}}{\partial x} & = & f \\ \Leftrightarrow & \frac{U^2}{L}\tilde{u}_{\tilde{t}} & - & \frac{\nu U}{L^2}\triangle_{\tilde{x}}\tilde{u} & + & \frac{U^2}{L}(\tilde{x}\cdot\nabla)\tilde{u} & + & \frac{U^2}{L\tilde{\rho}}\nabla_{\tilde{x}}\tilde{p} & = & f. \end{array}$$

Multplying with $\frac{L}{U^2}$ yields

$$\tilde{u}_{\tilde{t}} - \frac{\nu}{LU}\triangle_{\tilde{x}}\tilde{u} + (\tilde{x}\cdot\nabla)\tilde{u} + \frac{1}{\tilde{\rho}}\nabla_{\tilde{x}}\tilde{p} = \frac{L}{U^2}f.$$

Finally defining $\tilde{f} := \frac{L}{U^2}f$, using $\mathrm{Re} = \frac{LU}{\mu}$ and dropping the tilde symbols we get the dimensionless form of equation (1.15)

$$u_t - \frac{1}{\mathrm{Re}}\triangle u + (u\cdot\nabla)u + \frac{1}{\rho}\nabla p = f. \tag{1.20}$$

The dimensionless form of the Navier-Stokes equations has advantages when the given quantites are of different order. Numerically this prohibits problems due to bad condition numbers of the mass matrix.
Now we apply the knowledge of the parameter values from Table 2.1 to simplify the concrete system for the case of the seminal fluid.

Governing Equations of the Dung Fly Model

Multiplying equation (1.20) with the Reynolds number we get

$$\text{Re}\,(u_t + (u \cdot \nabla)u) - \triangle u + \frac{\text{Re}}{\rho}\nabla p = \text{Re}\; f.$$

Scaling f and p with the Reynolds number is straightforward. Since th convective term $(u \cdot \nabla)u$ and the time derivative u_t are scaled by Re but the diffusion term $\triangle u$ is not, there is a different order of the size of Re. Now in our case the Reynolds number is 10^{-6}. In such a case the effect of the convective term is neglectabe and we get the time-dependant linear *Stokes equations*

$$\text{Re}\; u_t - \triangle u + \nabla \tilde{p} = \tilde{f}.$$

The term Re u_t can also be neglected. The flow cannot capture the changes of the right hand side in a manner that inertia can play a role, especially because there are no high frequent changes to be expected in the function $f = f(t)$. Hence we get the inertia-less time-independent *Stokes equations*

$$\begin{aligned} -\triangle u + \nabla \tilde{p} &= \tilde{f} \\ \text{div} u &= 0. \end{aligned} \tag{1.21}$$

To state the mathematical problem we need boundary conditions. Since the problem is no longer time-dependant, we do not need initial conditions.

The derived equations need to be equipped with boundary condition that suit the situation of seminal fluid flowing through a spermathecal duct. Therefore we divide the boundary Γ in three distinct parts:

- an inflow boundary part Γ_{in} where the fluid enters the domain
- an outflow boundary part Γ_{out} where the fluid exits the domain
- a wall boundary part Γ_{wall} where the fluid can neither enter nor exit

We introduce mathematical criterions for these conditions: Every solution (u, p) has to fulfill

$$u = u_{in} \quad \text{on } \Gamma_{in} \tag{1.22}$$

$$(\nabla u - p) \cdot \mathrm{n} = 0 \quad \text{on } \Gamma_{out} \tag{1.23}$$

$$u = 0 \quad \text{on } \Gamma_{wall}. \tag{1.24}$$

For the inflow (1.22) we give a function $u_{in} = u_{in}(x)$, $x \in \Gamma_{in}$ determining the inflow velocity. The outflowing fluid has no component parallel to the outflow edge (1.23). This condition is the "natural" outflow boundary condition and has shown to be well-suited for such problems (e.g. Turek (1994)). At the wall boundary the fluid cannot move. This restriction (1.24) is called the homogeneous Dirichlet boundary condition.

Let Ω be the domain of the spermathecal duct. We transform the problem to have only two different boundary conditions. Γ_{in} and Γ_{wall} are Dirichlet type boundary condition. We therefore set $\Gamma_D := \Gamma_{in} \cup \Gamma_{wall}$. The outflow boundary will be denotes by Γ_N since it is a Neumann type boundary. Let u_0 be a function on Ω that fulfills the inflow condition on Γ_{in} and the wall condition on Γ_{wall}. Then the problem changes to:

Problem 2. *Find* $(\tilde{u}, p) \in \left(C^2(\Omega) \cap C^0(\bar{\Omega}) \cap C^1(\Omega \cup \Gamma_N), \mathbb{C}^1(\Omega) \cap C^0(\Omega \cup \Gamma_N)\right)$ *such that*

$$-\triangle \tilde{u} + \nabla p = f + \triangle u_0 \quad \text{in } \Omega \tag{1.25}$$

$$div\ \tilde{u} = div\ u_0 \quad \text{in } \Omega$$

$$\tilde{u} = 0 \quad \text{on } \Gamma_D \tag{1.26}$$

$$(\nabla \tilde{u} - p) \cdot n = 0 \quad \text{on } \Gamma_N. \tag{1.27}$$

Since in general it is not possible to analytically find a solution of this equations in this continuous form, we introduce the framework of *mixed variational problems* (Girault and Raviart (1979)) to handle Problem 2.

1.2.2 The Abstract Variational Problem

Let X and M be real Hilbert spaces with continuous bilinear forms

$$\mathbf{a} : X \times X \to \mathbb{R} \text{ and } \mathbf{b} : X \times M \to \mathbb{R}$$

and norms

$$\|\mathbf{a}\| := \sup_{0 \neq u, v \in X} \frac{\mathbf{a}(u,v)}{\|u\|_X \|v\|_X} \text{ and } \|\mathbf{b}\| := \sup_{0 \neq u \in X, 0 \neq p \in M} \frac{\mathbf{b}(u,p)}{\|u\|_X \|p\|_M}.$$

With the corresponding dual spaces X′ and M′ we can formulate the following mixed formulation problem

Problem 3. *Given* $f \in X'$ *and* $g \in M'$*, find* $(x, p) \in X \times M$ *such that*

$$\begin{array}{lll} \mathbf{a}(u,v) + \mathbf{b}(v,p) & =< f, v > & \forall v \in X \\ \mathbf{b}(u,q) & =< g, q > & \forall q \in M. \end{array}$$

Theorem 2 states a criterion for the existence and uniqueness of a solution to this variational problem (Girault and Raviart (1979)).

Theorem 2. *Let* X *and* M *be real Hilbert spaces,* $\mathbf{a} : X \times X \to \mathbb{R}$ *and* $\mathbf{b} : X \times M \to \mathbb{R}$ *continuous bilinear forms with the following properties:*

- $\mathbf{a}$ *is coercive, i.e. there is a constant* $\alpha > 0$ *such that*

$$\mathbf{a}(u,u) \geq \alpha \|u\|^2 \ \forall u \in X$$

- $\mathbf{b}$ *fulfills the inf-sup condition*

$$\inf_{0 \neq p \in M} \sup_{0 \neq u \in X} \frac{\mathbf{b}(u,p)}{\|u\|_X \|p\|_M} \geq \beta > 0$$

Then the general mixed formulation Problem 3 has a unique solution $(u, p) \in X \times M$ *and*

$$\|u\|_X + \|p\|_M \leq C \|f\|_{X'},$$

where C *is a constant depending only on* α*,* β *and* $\|a\|$*.*

1.2.3 The Weak Stokes Problem

Let $\mathrm{W}_p^m(\Omega)$ denote the Sobolev space of L^p-functions with weak derivatives up to order $m \in \mathbb{N} \cup \{0\}$ in $\mathrm{L}^p(\Omega)$, $p \in \mathbb{N} \cup \{\infty\}$. For the case $p = 2$, these spaces are Hilbert spaces and denoted by $\mathrm{H}^m(\Omega)$. Then we introduce the notation

$$\begin{array}{lll} & \|\cdot\|_{m,p,\Omega} \quad (|\cdot|_{m,p,\Omega}) & \text{for the norm (seminorm) in } \mathrm{W}_p^m(\Omega), \\ & \|\cdot\|_{m,\Omega} \quad (|\cdot|_{m,\Omega}) & \text{for the norm (seminorm) in } \mathrm{H}^m(\Omega), \\ \text{and} & \langle\cdot,\cdot\rangle_{m,\Omega} & \text{for the scalar product in } \mathrm{H}^m(\Omega). \end{array}$$

The Sobolev space that contains the velocity fields of Stokes flows with homogeneous Dirichlet boundary condition is denoted by

$$H_D^1(\Omega) := \left\{ \mathbf{u} \in H^1(\Omega) : \mathbf{u}|_{\partial\Omega} = \mathbf{0} \right\}.$$

The pressure space is $L^2(\Omega)$. For a given right-hand side $\mathbf{f} \in \mathbf{H}^{-1}(\Omega) := (H_D^1(\Omega))'$, the weak formulation of (1.21) reads:

Problem 4. *Find* $(\mathbf{u}, p) \in H_D^1(\Omega) \times L^2(\Omega)$ *such that*

$$\begin{array}{llll} \mathbf{a}(u,v) & +\mathbf{b}(v,p) & =< f, v > & \forall v \in H_D^1(\Omega) \\ \mathbf{b}(u,q) & & =< g, q > & \forall q \in L^2(\Omega). \end{array} \tag{1.28}$$

with bilinear forms

$$\begin{array}{ll} \mathbf{a} : H^1(\Omega) \times H^1(\Omega) \to \mathbb{R}, & \mathbf{a}(u,v) := \int_\Omega \nabla u : \nabla v \\ \mathbf{b} : H^1(\Omega) \times L^2(\Omega) \to \mathbb{R}, & \mathbf{b}(v,q) := \int_\Omega q \, div v. \end{array}$$

Both bilinear forms are continuous and, due to Korn's inequality, the bilinear form $\mathbf{a}$ is coercive with respect to $H_D^1(\Omega)$, i.e., there exists $\alpha > 0$ such that

$$\mathbf{a}(u,u) \geq \alpha \|u\|_{1,\Omega}^2 \quad \forall u \in H_D^1(\Omega). \tag{1.29}$$

The coercivity constant α depends only on the diameter of Ω. The bilinear form $\mathbf{b}$ fulfills the inf-sup condition (Girault and Raviart, 1979, Lemma 3.2). Applying Theorem 2 we have the existence of a unique weak solution of the problem (1.28).

1.3 Numerical Method

Although we know that an unique solution of the variational problem exists does not imply that it is easy to find. The solution of most differential equations, especially those that model real processes, cannot be found analytically (e.g. Problem 2). Due to that fact a lot of numerical methods came up on how to find an approximation of the the unique solution. The currently most common method for such a problem is the *finite element method* (FEM). The are several other techniques such as the finite difference methods (FDM), finite volume methods (FVM) or spectral Galerkin methods. One of the key advantages of finite element methods is the flexibility with the domain (unstructured meshes, adaptive refinement). We present the methods base, the variational formulation followed by the discretization of the equation using finite dimensional function subspaces. For further details of the method see Girault and Raviart (1979). Then we introduce the *mini element* completing the method description which is then ready to be implemented.

1.3.1 Abstract Approximation

We state the abstract mixed variational problem:

Problem 5. *Given $f \in X'$, find $(x, p) \in X \times M$ such that*

$$\begin{array}{llll} \mathbf{a}(u,v) & +\mathbf{b}(v,p) & =< f, v > & \forall v \in X \\ \mathbf{b}(u,q) & & = 0 & \forall q \in M. \end{array} \tag{1.30}$$

with real Hilbert spaces X and M and the abstract bilinear forms $\mathbf{a}$ and $\mathbf{b}$.

The concept of abstract approximation using a *Galerkin method* is based on choosing finite dimensional subspaces X_h and M_h. We always are in the *conforming* case, meaning that $X_h \subset X$ and $M_h \subset M$ holds. To cover the general case, let $\mathcal{X}$ be a real Hilbert space containing X and X_h, and M_h a subspace of M. Under the assumption that the bilinear forms are extendable to $\mathcal{X}$, we can formulate the discrete problem. Given $f \in \mathcal{X}'$ and $g \in \mathcal{M}'$, find $(x, p) \in X_h \times M_h$ such that

$$\begin{array}{llll} \mathbf{a}(u_H,v_H) & +\mathbf{b}(v_H,p_H) & =< f, v_H > & \forall v_H \in X_H \\ \mathbf{b}(u_H,q_H) & & =< g, q_H > & \forall q_H \in M_H. \end{array} \tag{1.31}$$

The coercivity property of $\mathbf{a}$ is inherited directly from the continuous to the discrete case. The inf-sup property of Theorem 2 is not transferable from continuous to discrete. But for the existence and uniqueness of the solution, an analogous result of Theorem 2 can be proven:

Theorem 3. *Let X and M be real Hilbert spaces with discrete subspaces $X_h \subset X$ and $M_h \subset M$, $\mathbf{a} : X \times X \to \mathbb{R}$ and $\mathbf{b} : X \times M \to \mathbb{R}$ continuous bilinear forms with the following properties:*

- *$\mathbf{a}$ is coercive on X_h*
- *$\mathbf{b}$ fulfills the discrete inf-sup condition: there is a constant $\tilde{\beta} > 0$ which does not depend on h such that*

$$\inf_{0 \neq p_h \in M_h} \sup_{0 \neq u_h \in X_h} \frac{\mathbf{b}(u_h, p_h)}{\|u_h\|_{X_h} \|p_h\|_{M_h}} \geq \beta > 0.$$

Then the discrete mixed variational problem (1.31) has a unique solution $(u_h, p_h) \in X_h \times M_h$. As h goes to zero, the discrete solution converges to the continuous solution.

Since now we have finite dimensional spaces, we can formulate the equations in (1.31) as an equation system. Let $(v_i)_{i=1}^{\dim X_h}$ be a basis of X_h and $(q_i)_{i=1}^{\dim M_h}$ a basis of M_h. Using the basis representations

$$u(x) = \sum_{i=1}^{\dim X_h} u_i v_i(x), \quad \text{and} \quad p(x) = \sum_{i=1}^{\dim M_h} p_i q_i(x)$$

we get the system

$$\begin{bmatrix} A & B \\ B^T & 0 \end{bmatrix} \begin{bmatrix} u \\ p \end{bmatrix} = \begin{bmatrix} f \\ g \end{bmatrix} \tag{1.32}$$

where

$$\begin{array}{lllll} A & = & (a_{i,j})_{i,j} & = & (\mathbf{a}(v_i, v_j))_{i,j} & = & \in \mathbb{R}^{\dim X_h \times \dim X_h} \\ B & = & (b_{i,j})_{i,j} & = & (\mathbf{b}(v_i, q_j))_{i,j} & = & \in \mathbb{R}^{\dim X_h \times \dim M_h} \\ f & = & (f_i)_i & = & \left(\int_\Omega \langle f, v_i \rangle\right)_i & = & \in \mathbb{R}^{\dim X_h} \\ g & = & (g_i)_i & = & \left(\int_\Omega \langle g, q_i \rangle\right)_i & = & \in \mathbb{R}^{\dim M_h}. \end{array}$$

We reduced the Stokes problem to solving a linear equation system which is uniquely solvable under the assumption of Theorem 3. The core of the numerical method is the choice of the discrete spaces X_h and M_h. For several reasons we restrict the description and the simulations to two dimensions (see Section 2.6 for more details).

1.3.2 Two-dimensional Finite Element Approximation

Straightforward finite dimensional subspaces for X and M are the spaces of piecewise polynomials. A great advantage of this choice is that the basis function have only a local support, i.e. the matrix of the linear system (1.32) has a sparse structure and only order $\dim X_h + \dim M_h$ entries. For problems with many unknowns, matrices with mostly non-zero entries (dense matrices) cause problems due to big amounts of required storage. Additionally direct solvers using matrix decomposition techniques perform much faster for sparse matrices.
To define those linear spaces we subdivide the computational domain in a finite number of elements. We limit ourselves to triangles as elements as it is the most common choice. Under the assumption that Ω is a polygonal domain, let $\mathcal{T}_h := \{\tau_i, 1 \le i \le n\}$ be a triangulation, i.e. a subdivision of Ω into closed triangles such that

$$\bar{\Omega} = \bigcup_{\tau \in \mathcal{T}_h} \tau, \quad \text{and} \quad h := \max_{\tau \in \mathcal{T}_h} \operatorname{diam}(T), \tag{1.33}$$

where two different triangles are either disjoint, have one common edge or one common node. Additionally we define Θ_h as the set of nodes of the triangulation $\mathcal{T}_h$.

To avoid numerical instability, we have to exclude the case where any triangles have very small angles. Let B_τ be the largest ball contained in τ. Then the triangulation is called shape-regular if there exists a constant $\rho > 0$ such that

$$\rho_\tau := \frac{\operatorname{diam}(B_\tau)}{\operatorname{diam} T} \ge \rho \quad \forall \tau \in \mathcal{T}, \ \forall h > 0.$$

We define the finite element space on such grids.

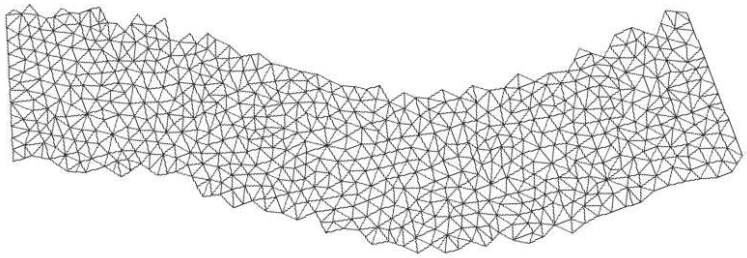

Figure 1.1: An example of a coarse finite element mesh discretizing a channel with rough boundary. Since there are no extreme angles, the shape-regularity (1.33) is fulfilled.

1.3.3 The Mini Element

There are many ways to apply the concept of finite elements to the Stokes equations. The *Mini Element* (Brezzi and Fortin (1991)) is a common, standard chioce. It uses continuous piecewise affine functions for velocity components and for the pressure, elements of

$$\mathcal{S}_{\mathcal{T}_h} := \left\{ v \in C^0 \bar{\Omega} | \forall \tau \in \mathcal{T}_h : v|\tau \in \mathbb{P}_1 \right\}.$$

Now we introduce a basis to this space, the so called *hat functions* (Fig. 1.2) as

$$\Phi_{\mathcal{T}_h} := \{\phi_z | z \in \Theta_h\}, \quad \text{where} \quad \phi_z(x) = \left\{ \begin{array}{ll} 1, & \text{if } x = z \\ 0, & \text{if } x \neq z \end{array} \right\}, \; x \in \Theta_h.$$

To fulfill the inf-sup conditions, the velocity space is enriched by *bubble functions* (Fig. 1.2) defined for each triangle τ as

$$b_\tau := 27 \prod_{z \in N(\tau)} \phi_z,$$

where $N(\tau)$ is the set of three nodes of τ. Outside of τ b_τ is zero. Defining $B_{\mathcal{T}_h} := \text{span}\{b_\tau : \tau \in \mathcal{T}_h\}$ the mini element space on $\mathcal{T}_h$ is defined by

$$\left(X_{\mathcal{T}_h}^{\text{mini}}\right)^2 \times M_{\mathcal{T}_h}^{\text{mini}} := (\mathcal{S}_{\mathcal{T}_h} \oplus B_{\mathcal{T}_h}) \times \mathcal{S}_{\mathcal{T}_h}.$$

The homogeneous Dirichlet boundary conditions are easily imposed by removing the hat functions corresponding to the nodes on the Dirichlet boundary segments. With the set of Dirichlet boundary nodes defined as $\Theta_h^{\partial\Omega}$ the space then becomes

$$\left(X_{\mathcal{T}_h}^{\text{mini},D}\right)^2 \times M_{\mathcal{T}_h}^{\text{mini}} := \left(\left\{v \in \mathcal{S}_{\mathcal{T}_h} | v(x) = 0, \; x \in \Theta_h^{\partial\Omega}\right\} \oplus B_{\mathcal{T}_h}\right) \times \mathcal{S}_{\mathcal{T}_h}.$$

A convergence result is presented in Girault and Raviart (1986): Assuming the existence of the continuous solution $(u, p) \in H^2(\Omega) \times H^1(\Omega)$, the method is convergent of order one. The error can be estimated by

$$\|u - u_h\|_{1,\Omega} + \|p - p_h\|_{0,\Omega} \leq Ch \left(|u|_{2,\Omega} + |p|_{1,\Omega}\right),$$

where the constant $C > 0$ neither depends on h, u nor p.

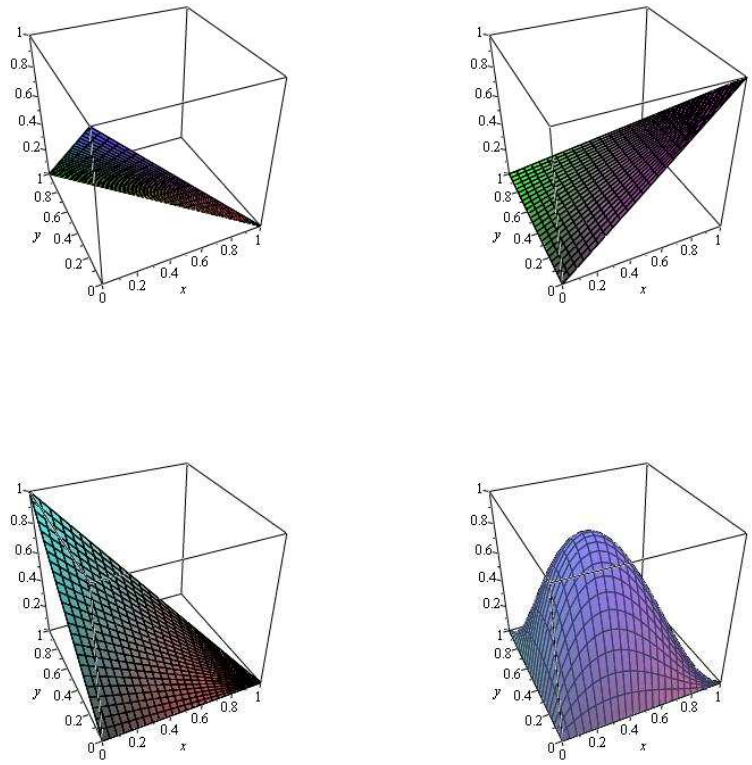

Figure 1.2: The three hat functions and the bubble function for the unit triangle.

We have now fully described the numerical method to be used to find a solution of Problem 5, as being an approximation of the solution of Problem 2. Accordingly we implemented the finite element method for our model-specific Stokes equations using mini elements. We outline a few aspects one typically has to consider for the implementation.

1.3.4 Implementation of the Numerical Method

There exist several objectives when implementing a numerical method. The first task is the selection of the method. If there are multiple applicable methods for a problem, the selection criterions usually are

Efficiency Efficiency is the combination of accuracy (how accurate is the computed solution) and speed (how much time is consumed by the performed method) of a method. In other words, the time a method requires to calculate a solution that has an error lower than a given bound is an efficiency measure.

Fitting the concrete problem Different methods have different advantages and therefore they suit better for a certain subset of problems they should be preferred for.

Implementational cost Complex methods take more time to be implemented.

Once one has choosen the method, every modular subproblem should be implemented considering the following criterions.

Fast algorithms Better approximations in general require a higher computational cost, e.g. a larger equation system has to be solved. Therefore, especially for parts of the algorithm that consume most of the simulation time, choosing efficient routines in inevitable.

Efficient program structure The architecture, as how loops are constructed or at which hierarchical level objects are created has also an influence on the simulation time and the consumed memory (this may depend on the programming language).

Computational accuracy Beside the compuational error that arises in a numerical calculation on a computer (machine precision), the numerical submethods (e.g. numerical integration) have to be chosen properly: simple methods lead to inaccurate results where complex methods are very costly.

Validity of the code To ensure that there are no mistakes in the implementation, the code must be validated. This is done by stating model problems which are constructed artificially in a way that the exact solution is known in advance.

We refer to these criterions in the following section, where we present some concepts of the implementation.

1.4 Bio-JCFD: A Software to simulate the Fluid Dynamics of the derived Model

1.4.1 Introduction

We created a program that is adapted for the biological application of dung fly sperm flow simulation (Wüst (2009)). It is written in Java and provides several interfaces to Matlab. The tests were performed on a SunFire 6800 with 32 CPUs and 144 GB RAM using shared memory parallelization.
Currently there exists big variety of free and commercial finite element software. Our intention to write the whole code on our own was to be able to have an easy extendable and customizable software. Changing bits even in most detailed parts is often hardly possible in adopted code. As soon as it comes to a method that affects certain parts of the existing algorithm it is very comfortable to have self-written code. However, there are highly optimized components in existing software impossible to implement in a moderate time frame. Therefore we included two black-box algorithms for handling the grid refinement, *Triangle* (Shewchuk, 1996, 2002) and for solving the equation system, *PARDISO* (Schenk and Gärtner, 2004, 2006). These parts are not affected by different problems differently. This chapter mainly consists of two parts: A description of the features and an insight in the implementation of the software.

1.4.2 Feature Overview

The software provides two different front-ends for the user. The *graphical user interface (GUI) front end* is a fully interactive window interface. From drawing the domain to finding the solution, the whole process is visualized on panels. Input and output interfaces are provided in dialogs. The *console front-end* is a slim way of running the software without a graphical interface. The program is controlled by parameter values that are entered by the user when starting the program in the console. One advantage of the console version is that one avoids the cost of drawing detailed grids and solutions. The parameter test series containing multiple flow simulations were run by scripts calling several instances of the console version program. An example is provided in the end of Section 1.4.2).
Those two front ends can be used in combination: One can draw a duct in the GUI version and then calculate a solution on a fine grid with the console front end to avoid additional computational cost. The concept of the two front ends are presented in detail in this section.

GUI front-end features

The graphical user interface provides three tabs at the bottom of the application window where one can switch between three panels. Every panel represents a stage of calculating the flow through a custom domain.

Following this routine the data can easily be sent to the next panel. On the other hand, input and output routines make each part (panel) independent of the main routine.

GUI Panels: The Skeleton Editor

The Skeleton Editor is a panel to create and edit Skeleton objects. The main control working with the editor is done using either the *Top-IconPanel* or the *MenuBar*. We group the actions in three subgroups: file handling, image handling and mode selection/use.
File handling provides a special data type (*.wf) that stores all details on image positioning and

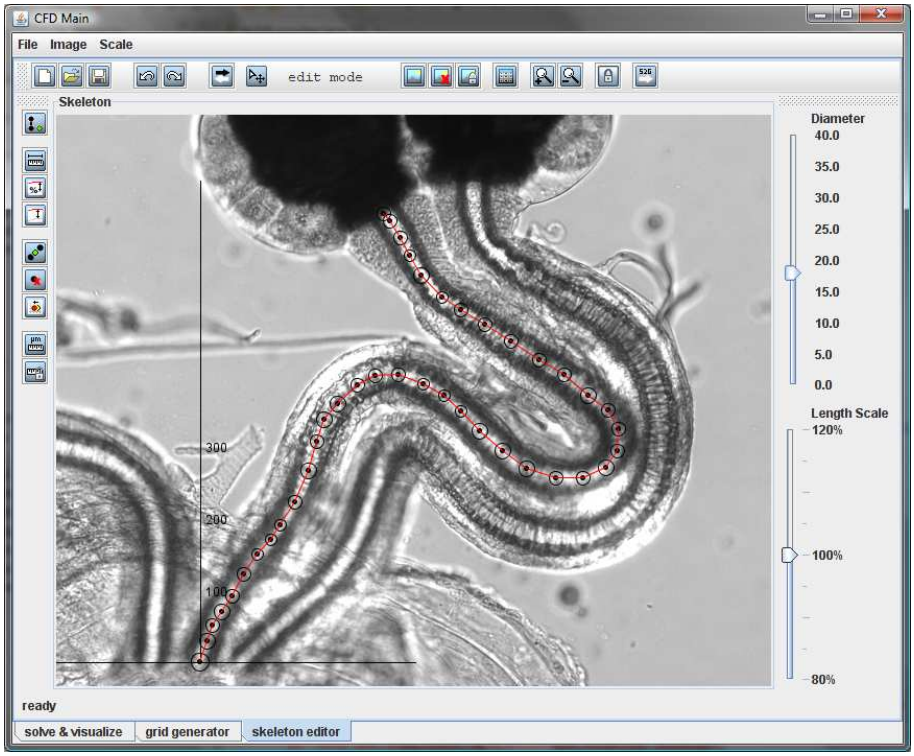

Figure 1.3: The Skeleton Editor. The drawing area contains an example of a traced image. The duct skeleton is modelled as a set of nodes with circles representing the duct diameter at that node.

drawn skeletons. Image files of the type JPG, JPEG, GIF or PNG can be inserted. The image will be attached to the background in its original resolution. There is a feature to lock the image to the background meaning that view changes as dragging and zooming will also affect the image and it will be moved and resized same as the background.
There are two working modes.

- In the *Freehand Mode* one can draw a skeleton by holding down the *CTRL*-key on the keyboard (the cross should turn green) and clicking into the drawing area. The whole feature panel (except the *new branch* button) is not available in this mode. When pressing the mouse button one can already adjust the diameter by dragging the mouse up and down.
- The *Edit Mode* is to edit the created skeletons. Beside the features in the panel on the left, one can mark nodes (*CTRL* + left click), drag nodes (*CTRL* + left click on a node and drag),

drag the drawing panel (*CTRL* + left click on the background and drag) and zoom in and out (*CTRL* + right click on the background and drag up/down). This feature is for accuracy reasons only available without having an image locked to the background.

When a Skeleton object is drawn it is transformed to a finite element grid in the grid generator panel. Skeleton objects can be saved and loaded in this panel. Detailed information about the file formats is given in Section 1.4.3.

GUI Panels: The Grid Generator

Between drawing the skeleton and solving the linear system one can specify the grid creation in this step. The Grid Generator converts Skeleton objects to Grid objects. Using the main routine, the Grid Generator is getting the skeleton from the send action of the Editor (or directly using the save/load dialog of this panel). One can apply a roughness to the boundary and create a basic grid, refine it and send the grid to the Solver Panel to do the numerical calculation of the flow. The main control working with the Editor is done again using either the *Top-IconPanel* or

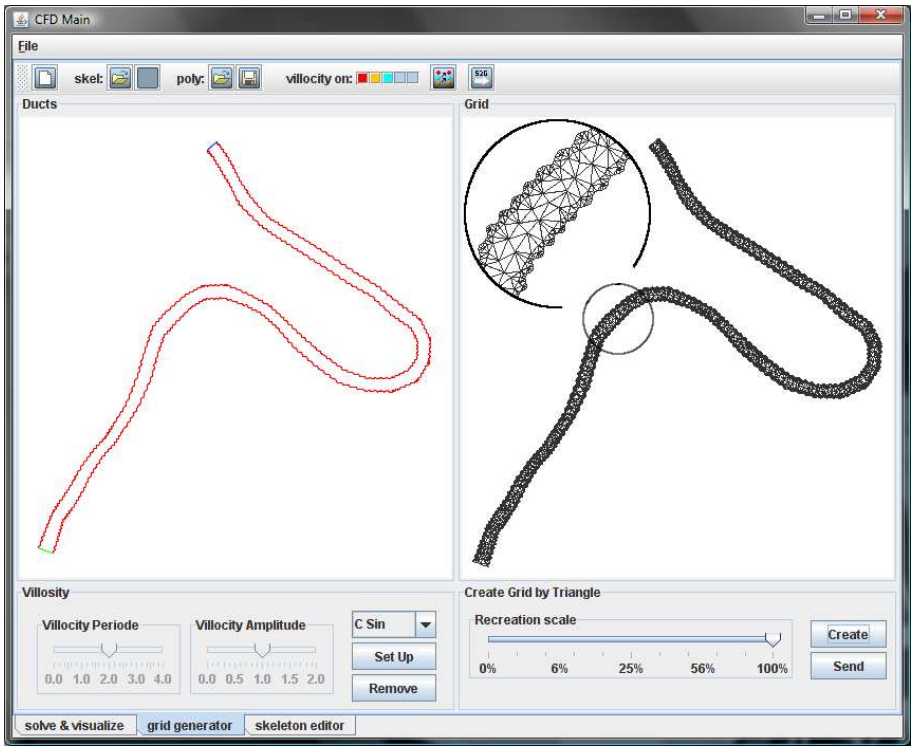

Figure 1.4: The grid generator panel. The left part shows the duct generated from the skeleton with a rough surface (microvillosity). The right part shows the grid generated from the duct on the left.

the *MenuBar*. Data input comes either from the editor panel as explained in the Editor section of by loading a Skeleton file (*.skel) or a Poly file (*.poly). While Skeleton files contain ordered node information divided in branches, Poly files are sets of marked segments (boundary parts). For details on all file types see Section 1.4.3. Loaded Skeleton objects are instantly converted to Poly

data (as visualized on the left canvas of Figure 1.4).

We implemented two approaches to model the roughness of the boundary segments (microvillosity) shown in the bottom left subpanel: a random roughness or a sine shape roughness. Period and amplitude can be entered either by a slider or an input dialog. The parts of boundary one likes to be affected by the roughness can be defined by the color tiles on the Top-IconPanel.
From the Poly data one can generate a Grid object in the right part of this panel (Fig. 1.4). The grid generation is done by an external code (*Triangle*, Shewchuk (1996, 2002)) building an unstructured, conforming mesh that conserves the boundary information. We use a maximal area restriction to refine the grid. The created finite element grid can then be used for the calculation in the solver panel by pressing the *send* button.

GUI Panels: The Solver Panel

The use of this panel is to solve the flow equations on the specified grid with the specified parameters. We provide direct in- and output routines for grid files. Either one loads a saved grid or have sent the grid from the Grid Generator panel. Then, after setting up the parameters and the choice of the solver, the discrete flow problem can be solved. We provide UMPACK (Davis and Duff, 1997, 1999; Davis, 2004a,b) for local use on any platform and PARDISO (Schenk and Gärtner, 2004, 2006) for parallel computation on our parallel machine. The assembly subpanel provides a selection of problems to solve and the usage of a solver for the equation system. The solution is visualized on the right side of the GUI. For an advanced visualization in Matlab the data is automatically exported.
For the tests of Chapter 2 we solve a stationary stokes equation with stationary inflow called *BUChannelProblem*. For the filament simulations in Chapter 4 we solve a time-dependant stokes equation with an immersed filament called *BUFilamentChannelProblem*.

The Poly Drawer Editor

The Poly Drawer panel (Fig. 1.6) is an extension to the editor that can be accessed from the menubar of the solver panel or as a standalone application. It is used similar to the editor with the difference that one draws directly Poly objects (the domain boundaries) instead of Skeleton objects. This is useful to bring up a model problem without creating or editing a text file.

Console Front-end Features

Switches are used to pass parameters to the program. These so called program arguments (Virtual Machine arguments) can be added when starting the console version of the software. The following examples show their use for several tasks. For large calculations that need a lot of memory. Therefore on uses the arguments -Xmx and -Xms that determine the heap space allocated when starting the program. The option *-cp bin* sets the classpath to the directory where the compiled class files are located, and *mathcomp.gui.cfd.JCFD* is the name of the class that is responsible for starting the routine with respect to the inserted argument values. After this class name the switches and their values can be added.
First, we present two easy examples of using the console version and the switches.

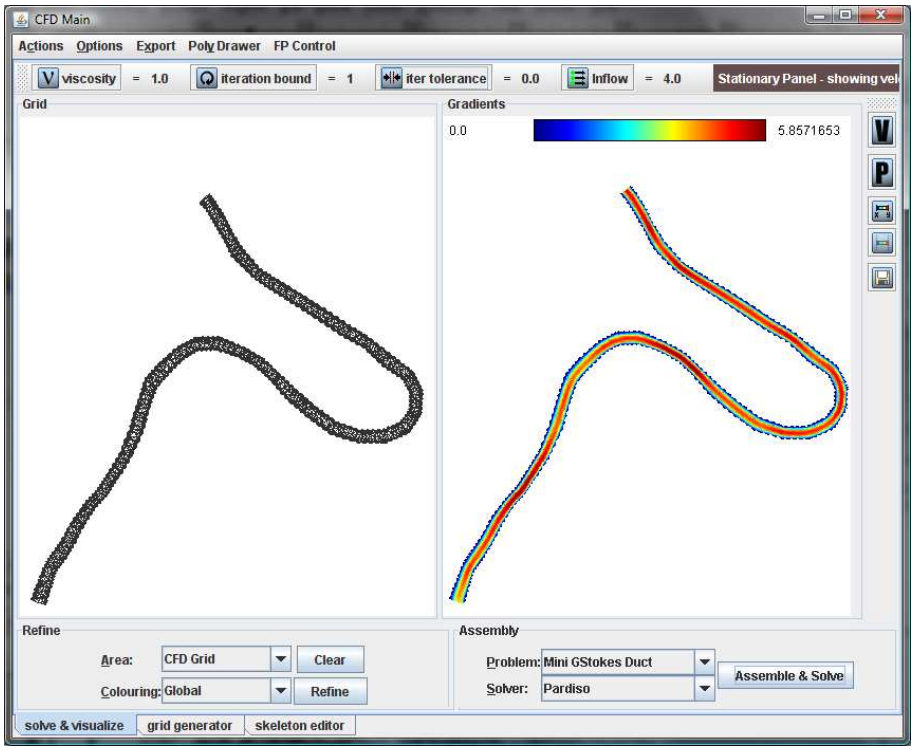

Figure 1.5: The solver panel. Left: The finite element grid. Right: The velocity weight of the approximated flow solution.

Switch	Argument	Action	if not added
-f(sourcePath)	Grid/Poly filepath	Grid/ Poly to load	Quit (must enter)
-r	int	number of red refinements	No refinements
-g	-	export grid to *localGrid.grid*	No export
-a	assembler:assemblerRun	assembler config	No assembling
-e	-	print out error calculation	No error calc
-x	export mode	export solution	No export

Table 1.2: Switches for the solving routine of the stationary flow problems.

```
1 java -Xmx1024M -Xms1024M -cp bin mathcomp.gui.cfd.JCFD -fgrids/
    square.grid -r10 -g
```

Description: The Console program JCFD is started with allocating 1GB of memory. The grid *square.grid* will be loaded and refined 10 times. After refining, the grid will be exported as *tempGrid.grid*

```
1 java -Xmx2G -Xms2G -cp bin mathcomp.gui.cfd.JCFD -fgrids/tempGrid.
    grid -aassemble.laplace.LaplaceAssembler -xscalar
```

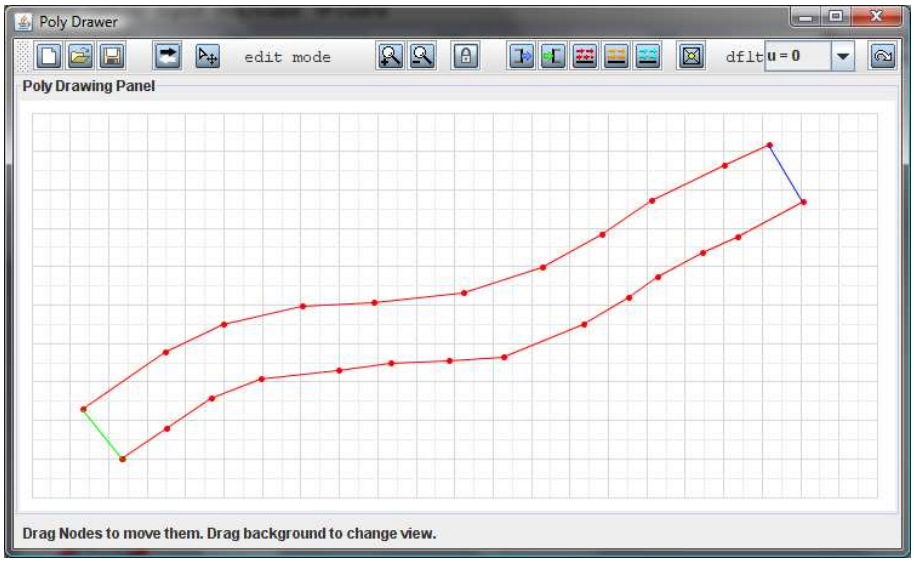

Figure 1.6: The Poly Drawer Editor. An interface to directly draw the boundary representation of a domain and generate a grid with respect to the boundaries and their boundary type indetifier.

Description: JCFD is started allocating 2 GB of memory. The previously exported grid *tempGrid.grid* will be loaded. Then the system is assembled by the class *LaplaceAssembler* and administrated by the standard AssemblerRun class (see Section1.4.6).

To run a whole series of tests we wrote shell scripts with loops over all parameters. For every single test the output is written into a text file for latter analyses. We give an example of the boundary roughness tests of the next chapter. Again, the different routines are treated parallel (different processors work on different parameter tests, where as the solving routine of every test internally parallelizes additionally.

```
1  #!/bin/bash
2  #xterm -e ls
3
4  periods=( 6 8 12 )
5  amplitudes=( 0.0 0.5 1.0 1.5 2.0 )
6
7  # grid generation
       ================================================
8
9  for per in ${periods[@]}
10 do
11     for amp in ${amplitudes[@]}
12   do
13       if [ -e "grids/k6.75_180.0_${amp}_${per}.grid" ]
14     then
15       echo "grids/k6.75_180.0_${amp}_${per}.grid already exists"
16     else
17       #echo "grids/k6.75_180.0_${amp}_${per}.grid doesnt exists"
18       java -cp bin mathcomp.gui.cfd.JCFD -K${amp}:${per} -D180 -A6
             .75
19     fi
20   done
21 done
22
23 sleep 10
24 # multirun ======================================================
25
26 for per in ${periods[@]}
27 do
28     for amp in ${amplitudes[@]}
29   do
30       if [ -e "outCART_${amp}_${per}.txt" ]
31     then
32       echo "outCART_${amp}_${per}.txt already exists"
33     else
34       echo "load grids/k6.75_180.0_${amp}_${per}.grid"
35       java -Xmx2G -Xms2G -cp bin mathcomp.gui.cfd.JCFD -aassemble.
             cfd.NSMini_BUCanal:run.NSIteratedAssemblerRun -A6.75 -
             fgrids/k6.75_180.0_${amp}_${per}.grid > outCART_${amp}_${
             per}.txt &
36       sleep 3
37     fi
38   done
39 done
```

This script runs a whole parameter series consisting of 15 independent program calls. In lines 4 and 5 the parameters ranges are defined. The first part (lines 9-21) creates the finite element grids, if they do not already exist. The second part (lines 26-39) runs the flow simulations and stores the solutions in text files.

1.4.3 Data Types

The program provides input and output routines for three file formats. A centerline representation of a channel called Skeleton, a boundary representation called Poly data and the finite element grid representation called Grid. We briefly introduce these three file formats with their application in the algorithms.

Skeleton Data Type

The class mathcomp.gui.cfd.Skeleton represents a data skeleton containing connected nodes with a radius. They can contain branchings and multiple branches. Skeleton objects can be created in the Editor tab of the launchable class mathcomp.gui.cfd.MainCFD_EMBED. By convention, Skeleton files are stored with ending *.skel*.

```
# Num Branches
2

# Branch Nodes
5 3

# Branch 0
1.836734693877551 5.918367346938822 17.4
11.63265306122449 150.40816326530617 17.4
-14.081632653061225 369.5918367346939 17.4 1
-185.51020408163265 495.7142857142858 17.4
-287.14285714285717 473.6734693877552 17.4

# Branch 1
119.38775510204081 509.1836734693878 15.2
198.9795918367347 461.4285714285715 15.2
245.51020408163265 305.91836734693885 15.2
```

The example above shows a simple example of a Skeleton file represents a main branch that has a branching at its third node. The class mathcomp.gui.cfd.Skeleton provides routines to load or write such files and to use them as Skeleton objects for further calculations.

Poly Data Type

The data type mathcomp.gui.cfd.PolyData contains of a set of nodes and a set of segments given by two nodes. Additionally every item has an optional parameter to determine its boundary type. We adopted this data structure from the external grid refinement tool *Triangle* (Shewchuk (1996, 2002)) we use. We present an example that fits the interface they provide.

```
# Nodes
4 2 0 1
1 0 0 3
```

```
2 1 0 3
3 1 2 3
4 0 2 3

# Edges
4 1
1 1 2 2
2 2 3 3
3 3 4 -2
4 4 1 3

# Holes
0
```

Skeleton objects can directly be converted to Poly Data objects by using the following Poly Data constructor:

```
   PolyData polyData = new PolyData(skeleton);
```

This routine is called for instance if one uses the mathcomp.gui.cfd.MainCFD_EMBED GUI to draw a Skeleton and send it to the Grid Generation tab by pressing the send button. To draw custom domains use the launchable mathcomp.gui.cfd.PolyDrawer class (also accessible over the menubar). One can store them as Poly file data and load it in MainCFD_EMBED's Grid Generation panel or export it directly to grids/polyDrawerGrid.grid by pressing the export button.

Grid Data Type

Files of the Grid file type have to accomplish the following structure conventions. Generally, a file has to list the nodes, the triangles and special boundaries (if necessary). We present an example of such a Grid file:

```
# Nodes
0 0 3
1 0 3
1 1 3
0 1 3

# Triangles
0 1 2
2 3 0

# Edges
0 1 3
1 2 3
2 3 3
3 1 3
```

The node coordinates are separated by whitespace where every node has its own line. Third parameter is used as boundary information. The handling is the same as for the special segments

discussed later.
Next, after an empty line, we have to specify the triangles respecting the following conventions: Every triangle gets its own line. Every triangle is defined by three nodes of the list above. The three position indices of the nodes in the list above (starting with index 0) represent a triangle. The nodes have to be itemized counterclockwise where the starting node can be chosen arbitrary. After another empty line one may mark special edges. The three numbers denote edge start node index, edge end node index and boundary type indetifier. The indentifier variable denotes the flag we use to distinguish different boundary parts (see Section 1.4.5). The conventions are shown in Table 1.3. Hence the special boundaries in the example file (all outer edges) are all homogeneous Dirichlet boundary parts.

index	description
-4	inhomogeneous Neumann boundary
-3	CFD: slip friction boundary
-2	homogeneous Neumann boundary (CFD: outflow)
-1	CFD: slip boundary
0	No Boundary, inner node
1, 2	inhomogeneous Dirichlet boundary (CFD: inflow)
3	homogeneous Dirichlet boundary (CFD: no-slip boundary)

Table 1.3: The boundary types and boundary type indetifiers

The class mathcomp.gridgeom.Grid can also represent other finite element types (e.g. rectangles). To create grids one can either write .grid files by hand, which makes sense only for simple data, or one can use the Poly Drawer to export a drawn Poly data object. If one comes from Skeleton data use MainCFD_EMBED to draw a Skeleton object, convert it to Poly data and then to a Grid. This can be done easily with GUI functions.

Beside the external grid refinement of *Triangle* (Shewchuk (1996, 2002)), we also provide a variety of grid refinements. Performing a global red refinement on a grid for instance looks like this:

```
1  GridRefiner r = new GridRefiner();
2  r.setGrid(grid);
3  r.setRefinerDesc(new GlobalRefinement());
4  r.refine();
5  Grid refinedGrid = r.getNewGrid();
```

This procedure shows the general concept of the refining model hierarchy. The identifier variable of nodes and edges are inherited to the refined grid.

1.4.4 Programming Concepts

There are many ways to implement a given algorithm. Programming concepts have to be chosen properly so that efficiency and extendability are balanced. We introduce briefly the concept of

object oriented programming since this is the governing concepts concepts of the software.

Object Orientation

Object oriented programming is widely spread and most programming languages adapted to this approach. The used language Java was developed by Sun Microsystems in 1990 and was one of the first languages that was fully platform independent. The following concepts are a common center of most object oriented programming languages. The following rough definitions are taken from the sun java tutorial website (*http://java.sun.com/docs/books/tutorial/java/concepts/*).

Object: An object is a software bundle of related state and behavior. Software objects are often used to model the real-world objects.

Class: A class is a blueprint or prototype from which objects are created.

Inheritance: Inheritance provides a powerful and natural mechanism for organizing and structuring your software.

Interface: An interface is a contract between a class and the outside world. When a class implements an interface, it promises to provide the behavior published by that interface.

Package: A package is a namespace for organizing classes and interfaces in a logical manner. Placing your code into packages makes large software projects easier to manage.

The Mapping Concept

For the treatment of matrices and vectors we introduce a new and fully custom concept developed and implemented by Philipp Thomann. Matrices and vectors are represented by maps. In the class mathcomp.la.MapVector the map maps Objects to values, whereas in the class mathcomp.la.MapMatrix it maps objects to an object-to-value-map. The real beauty of this mapping structure is, that there are no indices for the entries when filling a matrix or a vector. The few parts where indices are inevitable, one still can loop over elements or apply a fixed numbering. On the other hand, the deliverance from indices has many advances. Picture the assembly of a triangle element. This process can be done fully decoupled from the grid itself. The routine needs the matrix and the triangle. From the triangle the node objects representing the degrees of freedom are given and the values can be added to the global matrix by this (global) node object. One totally avoids any local to global routine and separate indices treatment. According to this example many parts in the simulation routine benefit in simplicity, readability and expandability from this concept.

The classes mathcomp.la.Matrix and mathcomp.la.Vector are abstract classes. For the general use they are extended by mathcomp.la.MapMatrix and mathcomp.la.MapVector. The package mathcomp.la contains the classes mathcomp.la.Index and mathcomp.la.IntegerToIndex. Creating a matrix or a vector is always done by having a set of degree-of-freedom objects (e.g. a set of Node objects). Such a set is called an Index.

```
1  Index index = new CollectionIndex(dof);
2  Matrix m = index.createMatrix();
3  Vector y = index.createVector();
```

Having created a matrix and a vector the handling is easy:

```
m.add(node1,node2,1.0);
y.add(node1,1.0);
```

Instantiating matrices and vectors can however not be done directly:

```
Matrix m = new MapMatrix(); // does not work
```

There is no implemented way to show a matrix in a full row and column way. In our applications, matrices are sparse and therefore appear in outputs as a listed maps. The MapMatrix and the MapVector classes provide a *toString()* function to get an output representation of the MapVector or the MapMatrix.
The class mathcomp.io.MatlabExport has a static function

```
public static void exportMatrix(Matrix m, String fileName)
```

to write such a list into a file. Matlab can read matrices and vectors from such files.

1.4.5 Boundary Handling

As shown in the previous section, Grid files consist of boundary information. How do those boundary types have to be treated in the assembly procedure? According to the weak formulation of the Stokes problem, for homogeneous Neumann boundary (do-nothing boundary, outflow) the nodes can be treated as common degrees of freedom. For Dirichlet boundary one has to specify the values for those parts in the code of the concrete assembler class by defining the functions on the corresponding boundary segments. The identifier of the grid file is equivalent to the String *info* in the implemented method. Implementing the boundary functions means that one can overwrite the method

```
protected double getDirichletValueAt(Node n, String bdtype)
```

of the main assembler in our concrete assembler class. We recommend to mark every boundary node and every boundary edge in the grid file (using the conventions from Table 1.3).

We present the core of the assemble.cfd.NavierStokesAssembler class, its *assembleGlobal()* method. It includes the handling of a third boundary condition: the slip boundary (no friction, no penetration).

```
public void assembleGlobal() {
  // create a set containing inflow edges
  inflowEdges = grid.getInflowEdges();

  // getting all we need for boundary calculation
  Map gridInfoMap = grid.getInfo();
  boundaryNodes = grabNodes(gridInfoMap);
  boundaryStokes = convertToStokes(boundaryNodes);

  // StokesNode to Double map for Dirichlet boundary nodes
  dirichletBoundaryValues = calcDirichletBoundary(boundaryNodes);
```

```
12
13      // Node to normal map for slip boundary nodes
14      consistentNormals = getSlipNormals(calcUnitNormals());
15
16      // creating the DOF set
17      dof = new TreeSet(GeometricComparator.getDefault());
18      createDof(grid, dof);
19
20      // create the matrix and right hand side
21      index = new CollectionIndex(dof);
22      m = index.createMatrix();
23      y = index.createVector();
24
25      // assemble elementwise by calling the assembleElement method
26      for (Iterator iter = grid.getElements().iterator();
27                iter.hasNext();) {
28        Triangle t = (Triangle) iter.next();
29        assembleElement(t);
30      }
31    }
```

In classes that extend assemble.cfd.NavierStokesAssembler this method may be overwritten, for instance because they iterate in some way. But still this method will be called multiple times inside the overwriting method. To give more insight in this idea of extending and inheriting structures we give an overview to the program hierarchy in the following section.

1.4.6 Program Hierarchy

The code is written fully object-orientated. The intention to design a program extendable for other problems (solving other elliptic differential equation numerically) leaded to the idea of stepwise extending classes. In detail this means that whatever methods are needed in multiple problems, they are moved to a general superclass of the concrete problem classes to avoid redundancy. The whole code is designed using such concepts. Not only makes it the code better readable, it is far more extendable.
Figure 1.7 shows the class tree of our Stokes problem algorithm.

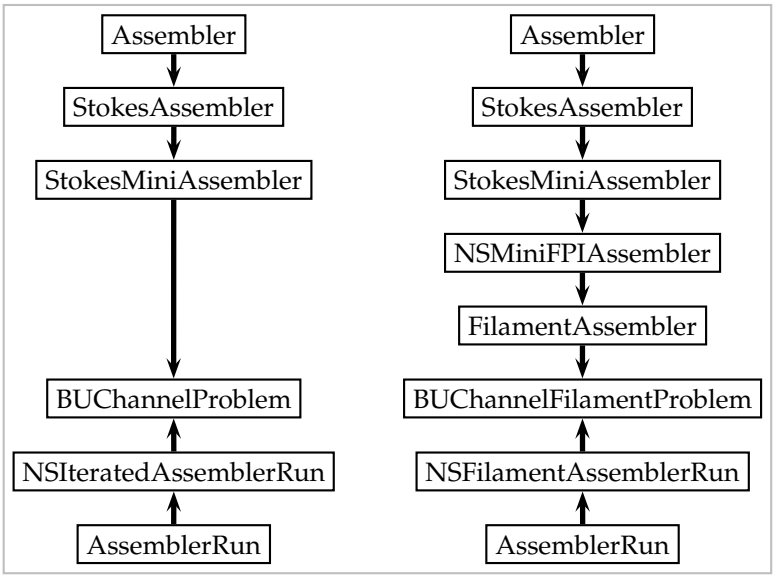

Figure 1.7: The class hierarchy of the simulations. Left: The homogeneous case of Chapter 2. Right: The case with immersed filaments of Chapter 4

The left hand side of Figure 1.7 shows the hierarchy used for the problems in Chapter 2. It includes the basic StokesAssembler class. The concrete problem is defined in the BUChannelProblem. The iterated assembleRun class is limited to one iteration since the problem is stationary. In contrast, the right hand side shows the filament problem hierarchy for Chapter 4. The Stokes equation becomes time-dependant and non-linear. Therefore the hierarchy is extended suitably. In the following section we address to this structure and why we use multiple assembler classes for one problem.

Assemblers and AssemblerRuns

The class hierarchy of the assembler classes presents as follows:

the main assembler (Assembler.java)
↓
concrete assemblers (e.g. LaplaceAssembler.java)

The *main assembler* defines basic routines, for example the piecewise assemblage of the global assemble routine. All methods in this class are inherited by subassemblers or directly by a concrete assembler. Among that, it provides constants and variables the whole assemble process has to know. Being an abstract class, the main assembler defines which methods every subassembler must implement, to be able to extend the main assembler. The *concrete assembler* class is an extension to the main assembler defining the specific properties of a problem such as boundary handling and grid selection. This structure is used for an easy extendability and low redundancy of the code. Picture two approaches to one problem. The implementation contains many common parts. According to the object-orientated programming concept one groups those common parts and introduces subclasses containing the specialized parts.
The classes starting from the bottom in Figure 1.7 are the AssemblerRun classes. They manage the main algorithm of the simulation process as for example shown in the algorithm of Section 4.4.

Simplicity without loss of Generality

Finally, after showing the power by giving concepts of extendability we show a complete example that solves a simple Laplace problem. The intention is to underline that extendability is not stringently attended by complexity.

```
1
2  public void solveCompleteSimpleExample() {
3    // load a simple grid
4    Grid testGrid = Grid.createFromFile("grids/test.grid");
5
6    // A simple Laplace-problem...
7    Assembler assembler = new LaplaceAssembler();
8    assembler.setGrid(testGrid);
9
10   // ...using the basic AssemblerRun...
11   AssemblerRun assemblerRun = new AssemblerRun();
12   assemblerRun.setAss(assembler);
13
14   // ... and load a solver
15   Solver solver = new PardisoLoader();
16   assemblerRun.setSolver(solver);
17
18   // here we call the run() method of the Runnable interface
19   // assembling and solving takes place in this method
20   assemblerRun.run();
21
22   // getting the solution as a MapVector back
23   Vector solution = assemblerRun.getX();
24 }
```

1.4.7 Extensions and Limitations

The structure of the software does not yield any limit in extending the code. An extension to a three-dimensional model is straight-forward implementation work since for channel flow the mathematical algorithms are well known. Three dimensional simulations are though much more costly in computational memory. The most important piece for such a realization, the solver, is ready for three-dimensional simulation at a state-of-the-art problem sizes (Schenk and Gärtner, 2004, 2006). It will be ongoing work to recompile the necessary modules for a 64bit architecture, because Java can only access a maximum of 4GB of memory per simulation in the 32bit version. For complicated domains (e.g. rough wall boundaries), one needs advanced numerical techniques to overcome the overwhelming demand to resolve such a domain with tetrahedrals. Concluding our object-oriented approach using only few black-box algorithms prevents from direct limitations for the next implementation steps for future model refinements.

2

Candidate Sperm Choice Adaptations in Yellow Dung Flies revealed by Fluid Dynamics Simulations

C. Wüst (A,B), S. A. Sauter (B), P. I. Ward (A), L. F. Bussière (A,C), preprint series 16-2008, Institute of Mathematics, University of Zurich

(A) Zoological Museum, University of Zurich (B) Institute of Mathematics, University of Zurich (C) School of Biological and Environmental Sciences, University of Stirling

Abstract

The mechanisms regulating sperm transfer, storage, and use in insects are unclear, even in well-studied species like the yellow dung fly (*Scathophaga stercoraria*). We use finite element methods and fluid dynamics theory to model sperm flow within female flies. With the help of software specially developed for this problem, we study four geometric aspects of female reproductive anatomy that may influence rates of ejaculate flow: spermathecal duct length, diameter, curvature, and the smoothness of the inner duct wall. In the parameter space defined by naturally observed variation in these traits, we find that spermathecal duct length and curvature have a small effect relative to duct smoothness and especially duct width. These findings will help to direct future research on the adaptive significance of variation in female reproductive tract morphology, and represent a novel contribution of fluid dynamics theory to sexual selection research.

2.1 Sperm Displacement in Yellow Dung Flies

The recognition that sexual selection continues after mating has stimulated much research on the mechanisms and consequences of sperm competition (competition between sperm for the fertilization of ova, Parker (1970a) and cryptic female choice (any female-controlled trait or process that influences the outcome of sperm competition, Eberhard (1996)). In spite of this research focus, the evolutionary consequences of postcopulatory sexual selection remain poorly resolved. This is partly because many of the crucial events are concealed within the reproductive tracts of females and therefore less amenable than premating sexual selection to direct observation and manipulation. In addition, postcopulatory sexual selection always involves several individuals (i.e., a female and at least two competing males), each of which may have interests in the outcome of selection that are not congruent with the interests of the others. These competing interests interact in complex ways, and there are numerous examples of behaviours or structures that have evolved in part via manipulation of other individuals (Arnqvist and Rowe, 2005; Blanckenhorn et al., 2007). As a consequence, disentangling the functional significance of traits that are involved in postcopulatory sexual selection is difficult, even in very well studied systems. There is a clear need for studies of the mechanisms mediating the outcome of reproductive interactions, and for any theoretical work which can clarify the most productive avenues for such research.

The yellow dung fly (*Scathophaga stercoraria*) has been a model system for research on post-copulatory sexual selection since the early 1970s (Parker, 1970a,b). Males congregate on dung pats to which gravid females are attracted for the purpose of oviposition (Parker, 1970b), and compete to copulate with these females. Although females do not appear to have significant control over the identity of their mates (Parker, 1970a,b), they influence the outcome of sperm competition (Hosken et al., 2001). Females assist sperm movement from the intromittent organs to the primary site of sperm storage, the three spermathecae, (Bernasconi and Hellriegel, 2002; Simmons et al., 1999). More intriguingly, females appear to sort sperm across their multiple sperm storage organs (Bussière et al., 2009) perhaps in order to manipulate the paternity of their offspring (Ward, 2000, 2007).

Although there is strong selection on males to achieve insemination success, (Parker, 1970a; Parker and Simmons, 1991; Simmons and Parker, 1992; Parker and Simmons, 1994; Simmons et al., 1999), the relationship between male traits and paternity varies considerably within and across studies (Simmons and Siva-Jothy, 1998). Such variation might be partly attributable to female adaptations designed to retain control over sperm movement (Hosken et al., 1999; Arthur et al., 2008). However, documenting the role of putative adaptations in sperm flow is hindered by the small scale of the structures involved and by the many potential interactions between males and females that might influence the outcome of sexual interactions.

In order to clarify which female traits might be adaptations for influencing sperm transfer, here we implement a finite elements method adapted to this specific problem. The fluid dynamics parameters describing sperm flow and the nature of the traits under study are such that a (numerical) model of two dimensional Stokes flow should give insights on the relative influence of each of these traits.

2.2 The Role of the Female Morphology in Sperm Displacement

Female insects can cause bias in the insemination success of different males thanks to properties of their reproductive anatomy (Minder et al., 2005; Miller and Pitnick, 2002). Female yellow dung flies store sperm in three (rarely four, Ward (2000)) spermathecae (Fig. 2.1) arranged into a singlet on one side of the body and two spermathecae collectively called the doublet on the opposite side (Arthur et al., 2008). Each spermatheca has an independent narrow duct through which sperm must travel to and from the site of sperm storage (Hosken et al., 1999). Since the male cannot

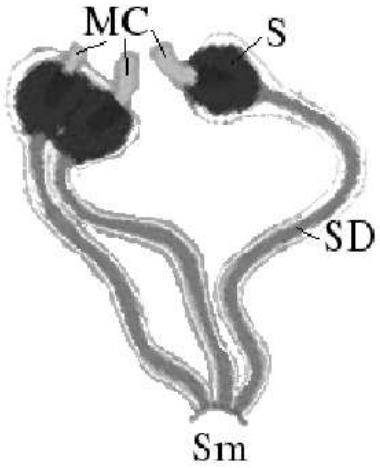

Figure 2.1: *Scathophaga stercoraria*, detail of the female genital tract (redrawn from Arthur et al. (2008)). S, spermatheca; SD, spermathecal duct; Sm, spermoraria; MC, muscular copulatrix.

deposit sperm directly into the spermathecae (Hosken, 1999), the length and width of the ducts may affect the rate of sperm storage. Moreover passage through long or narrow ducts could delay the time between insemination and storage so that other female adaptations can act to sort sperm in an adaptive manner. In addition to varying in length and width, the spermathecal ducts are also lined internally with chitin that forms circular ridges around the circumference of the ducts. This inner surface is extremely irregular because it is lined with microvilli (we will refer to this property as the duct's internal surface area), and contrasts markedly with the smooth lining of the spermathecae (Fig. 2.2) (Hosken et al., 1999). Because these microvilli could play a role in restricting fluid flow (Hosken et al., 1999), we will compare fluid flow in ducts lined with microvilli to ducts of the same width that lack these structures. A fourth putative adaptation for controlling sperm movement may be the degree of curvature exhibited by ducts. In fresh tissue preparations the ducts change shape dynamically after copulation (our own unpublished observations); they could therefore allow females to plastically modulate their response to different males. For example, by tightening the muscle attached to the spermathecal invagination females could straighten the duct and thereby potentially allow more rapid sperm flow relative to the situation in a curved duct (which is the natural resting state) (Hosken et al., 1999).

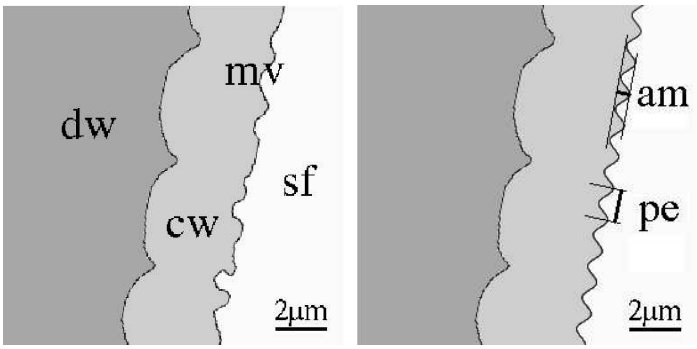

Figure 2.2: *Scathophaga stercoraria*, left: detail of the spermathecal duct wall redrawn from (Hosken et al., 1999). cw chitinous wall, dw, duct wall; mv, microvilli (increased surface area); sf, seminal fluid. right: detail of the increased surface area as modelled by sine waves for the purpose of systematically studying their effects on fluid dynamics. am, aplitude of the mv; pe, period of the mv.

2.3 Description of the Model Problem

Modelling the physics of ejaculate flow at this small scale necessarily involves making several assumptions. In this section we list several assumptions underlying the current approach, and discuss their implications briefly. We will consider some of these limitations in more detail in the discussion.

(1) The model is two dimensional. (2) The duct is modelled as a channel with common inflow- and outflow-conditions. The inflow is given as a parabolic velocity profile along the inflow edge. The direction of the outflowing fluid is limited to the direction parallel to the spermathecal ducts. (3) The fluid containing the sperm filaments is modelled as a *homogeneous fluid* with homogenous material properties. (4) The increased surface area is modelled using sine waves to simulate duct wall complexity. Mathematically, this is a straightforward parameterization of irregular boundaries. Whenever the physical properties of the fluid (e.g., *Density* and *viscosity*) cannot be directly measured, we use estimates based on other studies of dung flies or other insects. For example, in *Manduca sexta*, the hemolymph has a viscosity of 1-10 centiPoise (D. Saunders, pers. comm.). The *inflow velocity* is estimated from the fact that it takes fewer than 5 minutes for sperm to reach the spermathecae after the onset of copulation (Hosken et al., 1999). The chosen parameters are shown in Table 2.1.

Model parameter	Estimated quantity
density (ρ)	$1g/cm^3$
dynamic viscosity (μ)	$0.1poise$
kinematic viscosity (ν)	$10^7 \mu m^2/s$
inflow velocity (U)	$2\mu m/s$

Table 2.1: Estimated physical quantities for dung fly seminal fluid. The values are either deduced from other species or approximated by measurements described in section 2.3

2.4 Modelling Sperm Flow

In fluid dynamics there are two characteristic flow regimes: *laminar* and *turbulent flow*. *Laminar flow* means smooth flow in parallel layers (e.g., pressing tooth paste out of the tube) whereas *turbulent flow* always includes vortices and chaotic, stochastic property changes (e.g. water flowing around a ship). To distinguish those two regimes fluid dynamicists refer to the dimensionless *Reynolds number*:

$$\mathrm{Re} := \frac{L \cdot U}{\nu}, \tag{2.1}$$

where L is a characteristic length, U a characteristic velocity and ν the kinematic viscosity of the system. In a channel, the flow is laminar if $\mathrm{Re} < 2300$ and turbulent otherwise. For more details see Batchelor (1967). Flows at very small scales are typically strongly laminar. According to the estimates in Table 2.1 the Reynolds number of our system is 10^{-6}. Thus the system remains strongly laminar even if our estimates of fluid properties are off the mark by more than an order of magnitude. Strongly laminar flow (Stokes flow) of homogeneous fluids is well understood (Batchelor, 1967; Purcell, 1977). It becomes inertialess and is governed by the dimensionless *Stokes equations* derived from the physical laws for the conservation of mass and momentum:

$$\begin{aligned} -\Delta u + \nabla p &= 0 \\ \operatorname{div} u &= 0 \quad \text{+boundary conditions}, \end{aligned} \tag{2.2}$$

where (x, y) are the spatial coordinates, $\mathbf{u}(\mathbf{x}, \mathbf{y}) = (u_1(x, y), u_2(x, y))$ is the fluid velocity and $p(x, y)$ is the pressure in (x, y).

We use the *finite element method* in the form of the classical *Mini Element* which is a reliable approach for numerically solving the Stokes equations (Girault and Raviart, 1979; Ciarlet, 1978; Hackbusch, 1992). We use two-dimensional finite elements and discretize the spermathecal duct using $10^5 - 10^7$ elements. In order to validate our approach and apply it for the described tasks, we applied our methods to finding exact solutions for the Stokes problem in a straight two-dimensional channel (see Online Appendix A).

2.5 Numerical Experiments

We developed custom software to simulate sperm flow and determine the influence of several morphological parameters. Descriptions of the software and its implementation are provided at the following URL where the software is freely available for download (Wüst, 2009). We compare these results qualitatively with those for the analytically computed solutions of the Poiseuille flow in Online Appendix A. Our response variable is the drop in fluid pressure for a given flow rate (the difference of pressure at inflow to pressure at outflow) (problem 1). These results can easily be converted to the converse problem in which pressure drop is specified and flow rate is the response variable (problem 2) (for conversion details see Appendix A). Our objective is to determine how the flow rate depends on a single parameter when all other parameters are fixed. We begin by describing the relationship between duct length and width and the flow rate.

How duct length and duct diameter affect flow rate

The effect of duct length and diameter can be easily determined numerically. For a fixed set of parameters and a specified drop in pressure we have $\dot{Q} \sim \frac{1}{L}$, where L is the duct length. Equation (2.5) shows a cubic relationship between duct radius a and flow rate Q in two dimensions, $\dot{Q} \sim a^3$.

Effect of increased surface area in a straight duct

Assessing the effect of duct surface area and curvature is much more complex than assessing the effect of duct length and width. For the following numerical experiments we fix the following parameters in order to assess the influence of the reproductive tract curvature and roughness. For simplicity, we model a spermathecal duct $600\mu m$ long with a diameter of $13.5\mu m$. We specify the inflow using the exact solution of (2.4) and choose the centerline velocity $U_0 = 4\mu m/s$, which is equivalent to a mean inflow speed of $(8/3)\ \mu m/s$.

The increased surface area of the duct wall is modelled by superimposing a sine function. Changes in the period of the sine wave allow us to study the influence of changes in the number of microvilli in the duct wall, whereas changes in the amplitude of the sine wave allow us to change the depth of microvilli. We chose sine *period* values of $1, 1.5$ and $2\mu m$. For each of these values of period, *amplitudes* of $0, 0.5, 1, 1.5$ and $2\mu m$ were tested. The mean values for this range were suggested by an illustration in Hosken et al. (1999). For these 15 combined test-cases the observed pressure drop is plotted against the amplitude in Figure 2.3.

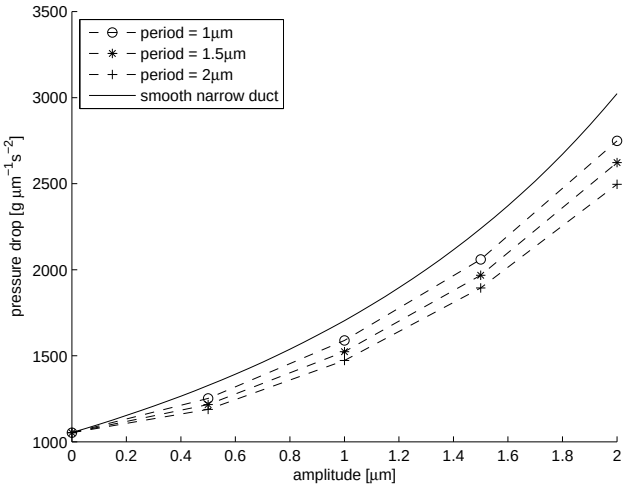

Figure 2.3: Pressure drop versus increased surface area amplitude for different periods compared with the *smooth narrow duct*. For this system, the pressure drop effect of problem 1 equates to an effect of $\approx 1/(\text{flow rate})$ in problem 2, since velocity and reduced diameter are not scaled (A). The figure illustrates the effect of curvature on the flow rate (higher values of pressure drop mean lower flow rate).

For every sine wave, the calculation featuring an amplitude of 0 (the duct with a smooth bound-

ary) is a lower bound (the case with the smallest drop in pressure). As an upper bound we consider the same smooth duct but with a reduced diameter as small as the minimal diameter of the duct with increased surface area (i.e., a duct diameter equal to the distance between microvilli on opposite sides of the duct). We call this parameter set the *smooth narrowed duct* in Figure 2.3. For a fixed sine wave amplitude, the pressure drop increases as the period decreases, and as the period approaches zero, the pressure drop approaches the value for the narrow duct. For a fixed period the pressure drop can be accurately fitted with a quadratic function. For a duct roughness similar to that shown in Hosken et al.'s (1999) micrographs (amplitude = 0.5 and period = 1.5) the pressure drop increases by a factor of about 1.15 compared to the smooth duct.

Effect of curvature in a smooth walled duct with a constant total length

To model a curved duct, we divide the centreline of the straight duct into three parts, each modelled using a Bezier curve of order 2. The total length is fixed at $600\mu m$. The curvature is parameterized by the angle α that is nearest to the inflow edge (Figure 2.4).

From the resulting smooth curve the duct boundary is obtained by orthogonal outward pro-

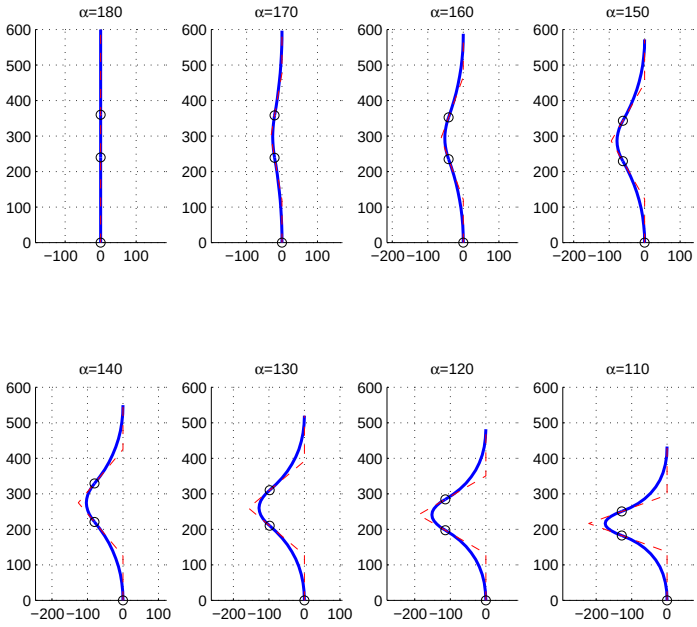

Figure 2.4: The curved duct centerline with parameter α of length $600\mu m$.

jection of the centreline. We limited the angles studied by measuring curvature angles in photographs of ducts from natural female reproductive tracts. The range we use represents the range of natural angles observed for these ducts

$$\alpha \in \{125, 130, ..., 180\},$$

where $\alpha = 180$ is the straight duct (for which the exact solution is already known).

For four different duct diameters, the effect of curvature is shown in Figure 2.5. Because the increase in relative pressure drop as the angle changes from $\alpha = 180$ to $\alpha = 125$ is only about 1.6%, we conclude that curvature does not substantially affect the flow in this parameter space. However, as predicted in the end of section 2.6, there is a slightly larger pressure loss at more acute angles (representing more curvature).
To determine the relationship between curvature and pressure drop, we use the exact solution for

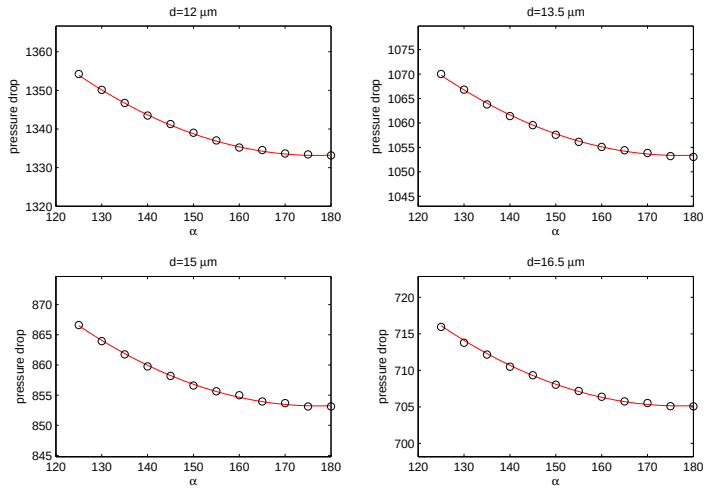

Figure 2.5: Pressure drop versus curvature parameter α for different duct diameters. The circles denote the computed results and the line denotes the function δp_{fit}. Since the pressure drop effect equates to $\approx 1/(\text{flow rate})$ there is a small effect of curvature on the flow rate (with more curvature meaning less flow).

Spermathecal duct diameter	Pressure drop increment in $\%$
$12\mu m$	1.580
$13.5\mu m$	1.610
$15\mu m$	1.580
$16.5\mu m$	1.542

Table 2.2: Percentage pressure drop from $\alpha = 180$ to $\alpha = 125$. Since pressure drop $\approx 1/(\text{flow rate})$ there is a small effect of curvature on the flow rate.

$\alpha = 180$ and a quadratic fit obtained from the computational results, and derived the following approximation in radians using $a = d/2$:

$$\delta p^2_{\text{fit}} := (p_{in} - p_{out})(a, \alpha) \approx \frac{48000}{a^2}\left(0.0186\alpha^2 - 0.1151\alpha + 1.1779\right) \tag{2.3}$$

The error $\mathbf{e_m} := \max_{a,\alpha} |\text{data}(a,\alpha) - p^m_{\text{fit}}(a,\alpha)|$ for quadratic ($\mathbf{e}_2 = 0.3002$) and cubic ($\mathbf{e}_3 = 0.3437$) fits shows that a higher order fit does not improve the approximation. This suggests that the pressure drop depends quadratically on the angle α. Equation (2.3) also shows that at fixed angle α the pressure drop depends on $1/a^2$.

Effect of curvature on flow in a duct with microvilli

As seen in the previous two tests, a rough surface affected the fluid flow by about 15% whereas the bending of the duct only resulted in a difference of about 1.6%. What is the effect of duct wall roughness in a curved duct? We increased the surface area of the same model used to study curvature, and compared it to the curved duct with smooth walls. We test the two cases $period = 1.5/amplitude = 1$ and $period = 1.5/amplitude = 0.5$ (once again, these values were obtained from micrographs of spermathecal ultrastructure (Hosken et al., 1999)). The effect on the pressure drop is approximately the same as that in figure 2.5. The drop in pressure reacts quadratically to a decrease in the angle of curvature α. As in Figure 2.3, the amplitude of the surface area has the largest influence on the fluid flow. In contrast, the curvature affects the flow only slightly; for an amplitude of $0.5\mu m$ the effect is only 1.7%, and for an amplitude of $1\mu m$ it is only 1.8%. The increase in surface area has slightly increased the effect of curvature.

2.6 Discussion

In a strongly laminar system such as the one that occurs within the reproductive tract of yellow dung fly females, our calculations suggest that a restricted duct diameter has an important effect on slowing seminal fluid flow (effect size 123.6% for a change in diameter equal to two standard deviations of natural variation). The length of the duct has a smaller influence on the flow rate (4.9% per two SDs), representing the additional time required for sperm to move into the storage organs. Whereas natural levels of spermathecal duct curvature appear to influence the flow rate of seminal fluid only slightly (with an effect size of 1.6%), increasing the roughness of spermathecal ducts has a more pronounced effect of 13.3%. However this effect is smaller than what would occur with simple duct diameter constriction (26.0%). The increased surface area of ducts lined with microvilli also slightly augments the effect of curvature, implying that these structures might act synergistically, although the combined effect is only slightly larger than that caused by microvilli alone.

In theory, these results support a possible role for the irregular duct lining with its increased surface area in augmenting female control over sperm movement and storage. However, such morphological complexity would probably not allow females to plastically manipulate the conditions of insemination (in contrast for example to muscles that might constrict ducts under neural or hormonal control). It could nevertheless provide a larger time window after intromission during which females might influence the number and location of sperm in storage by other means, for example, differential transport via female reproductive tract musculature.

Because we found the flow rate to be slower in a narrow duct than in the duct with increased surface area and the same minimum diameter, narrowing the duct would seem to be a more effective (and probably less costly in terms of structural investment) way to slow down sperm movement (Figure 2.3). Whether the increased surface area has a larger impact on sperm filaments (which

might, for example, move with greater or lesser ease through microvilli than a smooth-walled structure) than homogeneous fluid remains an open question and is the subject of ongoing work. Alternatively or additionally, it is possible that the increased surface area is related to an absorptive or secretory function such as the provision of nutrients or spermicidal compounds to the ejaculate. This function could in principle also play a role in sperm transport. For example, absorption of fluid deep within certain spermathecal ducts could create negative fluid pressure that speeds seminal fluid movement into those ducts. Evaluating these alternatives will require much more detailed information on the physiology of spermathecal ducts and ideally include empirical observations of the functional significance of increased surface area for sperm movement across females that vary in the morphology of their spermathecal ducts.
Although our results were generated by a relatively simple model, the basic behaviour of a homogeneous fluid in a stationary channel is not fundamentally different from the situation in a real stationary spermathecal duct. However, it is worth considering those aspects of our assumptions (in section 2.3) that might influence our conclusions below.

The model is two dimensional: Most of the parameters we studied are not influenced by the third dimension. The effect of all non-radial parameters such as length and curvature of the ducts remains of the same order as in two dimensions. The influence of duct diameter on the flow rate differs in three dimensions, but the magnitude of this effect is known to be of power 4 ($\dot{Q} \sim a^4$) instead of 3 (as in two-dimensions). Using a range of $d = 13.5 \pm 1.5 \mu m$ we find that the flow rate from lower bound to upper bound increases by 192% in three dimensions instead of 124% in two dimensions.

Boundary condition setting: fixed inflow, parallel outflow: This assumption is a simplification of the real situation within female dung flies, which at the current time is still not well understood: for example seminal flow within spermathecal ducts may not be constant because it may occur concurrently in both directions (Simmons et al., 1999). Furthermore, the outflowing seminal fluid in our model is collected in the spermathecae, which gradually fill in real flies, and there may be an accumulation or obstruction caused by the finite volume of the sperm storage organs. We are thus limited in extrapolating our findings to the full set of natural conditions under which ejaculates move within female yellow dung flies. Nevertheless, our findings apply at least to virgin flies with empty spermathecae. The extent to which these conditions may have selected on female morphology in the context of cryptic choice are limited, however, because relative rates of sperm movement are only likely to exert an indirect influence on female fitness if the female has mated more than once (Eberhard, 1996).

The fluid is homogeneous: The mechanics of flexible objects such as spermatozoa in fluid are difficult to describe (Cox, 1970; Shelley and Ueda, 2000). Additionally, the filaments are immersed in a flowing fluid, which requires a coupling technique for the fluid equations and the filament equations (e.g. Cortez et al. (2004)). In our model we made the simplifying assumption that the fluid is homogeneous for practical reasons. This approach provides some insight on the relationship between reproductive morphology and fluid dynamics for systems in which sperm are inactive during copulation (e.g., in some spiders, Baccetti et al. (1970)). Furthermore, for species having motile sperm during copulation it provides a preliminary view of how morphology might affect aspects of seminal fluid transfer that can be supplemented by subsequent work in which the effects of sperm filaments (and swimming sperm in particular) are more thoroughly implemented. The refinement of the model to include sperm filaments as physical objects into the flow is the subject of ongoing work.

Directions for future work

There are at least three areas that should be the subject of future research. First, the fact that we model the fluid homogeneously may be an oversimplification, especially because the sperm filaments are very long compared to the duct diameter. We hypothesize that the effect of morphology on the flow rate will increase when the filaments swimming in the fluid are modelled. Second, to understand the process of sperm transfer, we must first understand the flow of the ejaculate, but we acknowledge that modelling a system where the sperm filaments are squeezed through the duct differs in its physical description (and the best methodological approach) from a system where the sperm filaments are self-propelled. Incorporating the propulsive effects of sperm cells themselves is thus an additional challenge. Finally, laboratory experiments that examine empirically how the parameters we discuss above influence sperm movement in living flies would be useful to validate our approach and clarify where more theoretical work is needed. These additions notwithstanding, the current work has nevertheless already clarified some aspects of female reproductive anatomy (duct diameter and width) that are much more likely to be adaptations for sperm choice than others (duct curvature and internal surface area), at least in the context of controlling ejaculate flow. As such, it represents an important first contribution of fluid dynamics to studying the adaptive significance of postcopulatory interactions.

Online Appendix A: Two Dimensional Channel Flow

Consider the two-dimensional longitudinal section of a straight (and infinitely long) pipe with the y-axis as its axisymmetrical center and radius $a = d/2$. We use a Cartesian coordinate system and consider stationary flow. Note that the flow field is constant with respect to the axial component y since the pipe is infinitely long. This flow equation can be solved analytically (Batchelor (1967)), and by enforcing the *no-slip* boundary condition (the fluid at the wall cannot move) we obtain

$$u_1 = 0 \;\; u_2(\mathbf{x}) = c_1 \frac{\partial p}{\partial y} \left(x^2 - a^2\right), \tag{2.4}$$

where $c_1 := 1/2$. This is the *Poiseuille flow*. The formula shows that the axial flow profile is parabolic with a maximum at the centerline. Further, the flow velocity is proportional to the pressure gradient $\partial p/\partial y$. An important quantity of our tests is the flow rate $\dot{Q}$ which describes how much fluid is transported through a cross section per second. Mathematically

$$\dot{Q} = -c_2 a^3 \frac{\partial p}{\partial y}, \tag{2.5}$$

where $c_2 := 2/3$. This is known as *Poiseuille's law*. Using Poiseuille's law we can compute the pressure drop along a finite canal of length L with centerline velocity U_0:

$$p(L) - p(0) = L \frac{\partial p}{\partial y} = -L \frac{c_1 U_0}{a^2}. \tag{2.6}$$

Since we cannot find an exact solution for pipes of finite length, we use an inflow profile according to (2.4) to compare the numerical approximations with the exact solution in (2.6). For flow in curved pipes the equations cannot be solved analytically either. Previous analyses have usually relied strongly on numerical and physical experiments (Dean, 1927, 1928). However, these special curvature effects (centrifugal effects, vortices) can also be directly related to the Reynolds number

and since the Reynolds number is very small in our application, irregular flow effects in curved parts of the duct can be neglected. Nevertheless, fluid flow in curved tubes is affected more by friction at the wall of the duct. For our numerical experiments we therefore expect a slightly smaller flow rate in more curved tubes.

3

A Bead-Spring Model for Sperm Filament Simulation

3.1 Introduction

There exists a variety of approaches to model filaments in fluid flow. We present a decoupled formulation by introducing the mechanics of the filament itself in this chapter. The simulations are limited to straight channels with non-coupled time-independent Poiseuille flow. The coupling of the filament with the fluid flow is presented in the next chapter. For more references and an overview of the methods see Section 4.1.

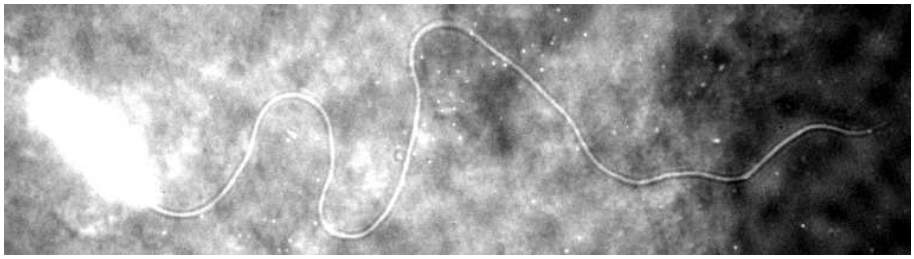

Figure 3.1: Photograph of a real sperm filament.

The modelling of sperm filaments requires a full description of the configuration and the governing forces. There exist several approaches (see Lighthill (1975) for an overview). We model the filament by a simple common bead-spring configuration as presented in Lowe (2001). The chapter is structured as follows: We describe the forces acting on the filament in Section 3.2. For the description of the model one needs material parameters stating how the material resists to bending, stretching and being dragged across the fluid.

The approach followed in Section 3.3 is to use a very simple model problem containing a filament of only three nodes to find the parameters approximately. Given the parameters we can calculate

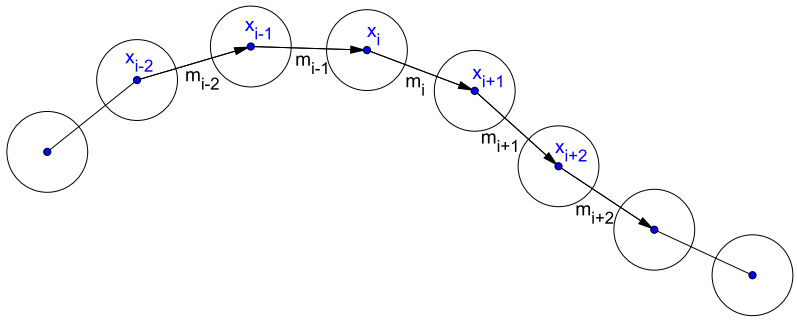

Figure 3.2: The configuration of the filament.

the exact stationary shape (or at least an approximation using a numerical method) of the simple filament. From comparing (tracing) real microphotographs we compare shapes and give set of parameters that suit to the measured shape in Section 3.4.

3.2 Modelling the Filament

We model the filament by a bead-spring configuration that also resists bending (Figure 3.1). Therefore, without any self-propulsion, we have three forces acting on the i-th bead of the immersed filament.

1. A tension force $F_{\mathcal{S},i}$ that denotes the resistance of the filament to stretching.
2. A bending force $F_{\mathcal{B},i}$ that denotes the resistance of the filament to bending.
3. A hydrodynamic or viscous force $F_{\mathcal{H},i}$ that denotes the force exerted by the fluid on the filament.

The filament has a total number of N beads. As shown in Figure 3.1, $x_i = (x_i^{(1)}, x_i^{(2)})$ denotes the coordinates of the i-th bead and $m_i = x_{i+1} - x_i$ the vector from x_i to x_{i+1}. The segment length is $l_i := |m_i|$ and $\widehat{m}_i := m_i/l_i$. For simplicity all segments have the same given equilibrium length l_0. Without a repercussion from the fluid onto the filament and in absence of active forces of the filament the shape of the filament is given by Newton's equation of motion

$$m_i \frac{dv_i}{dt} = F_{\mathcal{S},i} + F_{\mathcal{B},i} + F_{\mathcal{H},i}. \tag{3.1}$$

For the following descriptions we divide equation (3.1) by the mass m_i, including it in the individual parameters. We move on to the detailed description of those three forces.

3.2.1 The Tension Force

The tension force is deduced from the spring equation (Hooke's law), which relates the force exerted by a spring to the distance it is stretched by the spring constant $\mathcal{S}$, measured in force per

length.

$$F = -\mathcal{S}x \tag{3.2}$$

The negative sign indicates that the force exerted by the spring is in direct opposition to the direction of sperm transport. It is called a *restoring force*, as it tends to restore the system to equilibrium. The potential energy stored in a spring is given by

$$U = \frac{1}{2}\mathcal{S}x^2 \tag{3.3}$$

which comes from adding up the energy it takes to incrementally compress the spring given by the integral of force over distance. The total potential energy for our filament is then

$$U_{\mathcal{S}} = \frac{1}{2}\mathcal{S}\sum_{i=1}^{N-1}\left(l_i - l_0\right)^2 \tag{3.4}$$

Then the resulting tension force on the i-th bead is

$$F_{\mathcal{S},i} = -\nabla_{x_i} U_{\mathcal{S}} \tag{3.5}$$

describing the change of potentials when moving the i-th bead. On segment m_i we have

$$\begin{aligned}
\nabla_{x_i} U_S \mid_{m_i} &= \nabla_{x_i}\frac{1}{2}\mathcal{S}\left[\left((x_i^{(1)} - x_{i-1}^{(1)})^2 + (x_i^{(2)} - x_{i-1}^{(2)})^2\right)^{1/2} - l_0\right]^2 \\
&= \mathcal{S}(l_i - l_0)\begin{pmatrix} \frac{1}{2l_i}\cdot 2\cdot(x_i^{(1)} - x_{i-1}^{(1)}) \\ \frac{1}{2l_i}\cdot 2\cdot(x_i^{(2)} - x_{i-1}^{(2)}) \end{pmatrix} \\
&= \mathcal{S}(l_i - l_0)\,\widehat{m}_i.
\end{aligned}$$

Applying the same calculation to the segment m_{i+1} the stretching force for bead i obeys

$$\mathcal{F}_{\mathcal{S},i} = -\mathcal{S}(l_i - l_0)\,\widehat{m}_i + \mathcal{S}(l_{i+1} - l_0)\,\widehat{m}_{i+1}. \tag{3.6}$$

3.2.2 The Bending Force

We introduce a three bead bending potential (Lowe (2001)), meaning that every three connected beads form a bending potential. The two segments m_{i-1} and m_i connecting the two consecutive beads x_{i-1}, x_i and x_{i+1} define an angle φ_i. Then

$$\cos(\varphi_i) = \widehat{m}_{i-1}\cdot\widehat{m}_i.$$

The radius r_i of the unique circle passing the three beads can be found from the cosine rule

$$\frac{1}{r_i^2} = \frac{2}{l_0}(1 - \cos(\varphi_i)) \tag{3.7}$$

assuming for now that every segment has its equilibrium length l_0. The continuous total bending energy of an elastic rod is given by

$$U_{\mathcal{B}} = \frac{\mathcal{B}}{2}\int_0^L \frac{1}{r_i^2}\mathrm{ds}, \tag{3.8}$$

where $\mathcal{B}$ is the bending modulus, L the total length of the filament and s a parameter that follows the filament (Landau et al., 1996). Combining (3.7) and (3.8) we find a discretized bending energy

$$U_{\mathcal{B},i} = \frac{\mathcal{B}}{l_0}(1 - \cos(\varphi_i)), \tag{3.9}$$

and the resulting total bending energy of the filament

$$\begin{aligned} U_{\mathcal{B}} &= \sum_{i=2}^{N-1} U_{\mathcal{B},i} \\ &= \frac{\mathcal{B}}{l_0} \sum_{i=2}^{N-1} (1 - \cos(\varphi_i)). \end{aligned}$$

The bending force on bead i can be obtained again by taking the spacial derivative of the potential. Since we use the three bead potential we get

$$F_{\mathcal{B},i} = -\nabla_{x_i} \left(U_{\mathcal{B},i-1} + U_{\mathcal{B},i} + U_{\mathcal{B},i+1} \right). \tag{3.10}$$

Given the relations

$$\begin{aligned} \nabla_{x_i} \widehat{m}_i &= \frac{1}{l_i} \left(\mathbb{I} - \widehat{m}_i \widehat{m}_i^T \right) \\ \nabla_{x_i} \widehat{m}_{i+1} &= -\frac{1}{l_{i+1}} \left(\mathbb{I} - \widehat{m}_{i+1} \widehat{m}_{i+1}^T \right) \end{aligned}$$

we can give explicitly describe every term in the sum of (3.10).

$$\begin{aligned} \nabla_{x_i} U_{\mathcal{B},i-1} &= -\frac{\mathcal{B}}{l_0} \left[\widehat{m}_i \cdot \underbrace{\nabla_{x_i} \widehat{m}_{i-1}}_{=0} + \widehat{m}_{i-1} \cdot \nabla_{x_i} \widehat{m}_i \right] \\ &= -\frac{\mathcal{B}}{l_0} \left[\frac{1}{l_i} \left(\mathbb{I} \cdot \widehat{m}_{i-1} - \widehat{m}_i \widehat{m}_i^T \cdot \widehat{m}_{i-1} \right) \right] \qquad (3.11) \\ \nabla_{x_i} U_{\mathcal{B},i} &= -\frac{\mathcal{B}}{l_0} \left[\widehat{m}_{i+1} \cdot \nabla_{x_i} \widehat{m}_i + \widehat{m}_i \cdot \nabla_{x_i} \widehat{m}_{i+1} \right] \\ &= -\frac{\mathcal{B}}{l_0} \left[\frac{1}{l_i} \left(\mathbb{I} \cdot \widehat{m}_{i+1} - \widehat{m}_i \widehat{m}_i^T \cdot \widehat{m}_{i+1} \right) - \frac{1}{l_{i+1}} \left(\mathbb{I} \cdot \widehat{m}_i - \widehat{m}_{i+1} \widehat{m}_{i+1}^T \cdot \widehat{m}_i \right) \right] \qquad (3.12) \\ \nabla_{x_i} U_{\mathcal{B},i+1} &= -\frac{\mathcal{B}}{l_0} \left[\widehat{m}_{i+2} \cdot \nabla_{x_i} \widehat{m}_{i+1} + \widehat{m}_{i+1} \cdot \underbrace{\nabla_{x_i} \widehat{m}_{i+2}}_{=0} \right] \\ &= -\frac{\mathcal{B}}{l_0} \left[-\frac{1}{l_{i+1}} \left(\mathbb{I} \cdot \widehat{m}_{i+2} - \widehat{m}_{i+1} \widehat{m}_{i+1}^T \cdot \widehat{m}_{i+2} \right) \right] \qquad (3.13) \end{aligned}$$

The sum in (3.10) can then be obtained as

$$\begin{aligned} \mathcal{F}_{B,i} &= \frac{\mathcal{B}}{l_0} [\frac{\widehat{m}_{i-1}}{l_i} - \widehat{m}_i \left(\frac{\widehat{m}_i \cdot \widehat{m}_{i-1}}{l_i} + \frac{1}{l_{i+1}} + \frac{\widehat{m}_i \cdot \widehat{m}_{i+1}}{l_i} \right) \\ &+ \widehat{m}_{i+1} \left(\frac{\widehat{m}_i \cdot \widehat{m}_{i+1}}{l_{i+1}} + \frac{1}{l_i} + \frac{\widehat{m}_{i+1} \cdot \widehat{m}_{i+2}}{l_{i+1}} \right) - \frac{\widehat{m}_{i+2}}{l_{i+1}}]. \end{aligned}$$

For the beads at the beginning and the end of the filament ($i = 1, 2, N-1, N$) the formula reduced to the existing parts. In the focus of implementation the formulas (3.11)-(3.13) may be preferred for that reason.

3.2.3 The Viscous Force

For a simple chain where the beads are interpreted as balls with a given radius R we can identify the viscous force as a Stokes drag

$$\mathcal{F}_{\mathcal{H}} = 6\pi\mu R(v-u). \tag{3.14}$$

There are more detailed and complex descriptions of the viscous force. The force is time dependent and depends in addition on the instantaneous shape of the filament (Landau et al. (1996)). Both dependencies are troublesome to apply using the described model. As an advanced model we introduce an approximation using a friction tensor on each bead (Lowe (2001)). Introducing $\widehat{p}_i$ and $\widehat{n}_i$ - consistent perpendicular and consistent parallel unit vectors to each filament bead. Then the approach is given by

$$\mathcal{F}_{\mathcal{H},i} = -\gamma_i(v-u), \tag{3.15}$$

where

$$\gamma_i := \gamma_i^{\parallel}\widehat{p}_i\widehat{p}_i^T + \gamma_i^{\perp}\widehat{n}_i\widehat{n}_i^T. \tag{3.16}$$

In other words one physically represents the viscous force by means of a parallel ($\gamma_i^{\parallel}$) and a perpendicular ($\gamma_i^{\perp}$ friction coefficient. This simplification does obviously change the flow of the filament, but its influence is negligible in a context compared to all forces (Lowe (2001)).
The friction coefficients are analytically known for an infinitely slender rod (Cox (1970)) to be

$$\begin{aligned} \gamma_0^{\perp} &= \frac{4\pi\mu l_0}{\log(l/2R)}, \\ \gamma_0^{\parallel} &= \frac{\gamma_0^{\perp}}{2}. \end{aligned}$$

Friction coefficients for a slender rod differ from the infinitely slender coefficients (Hancock (1953), Purcell (1977)). However they can not be calculated analytically. For a rod of $2R/l = 1/50$ Lowe (2001)) found that numerically one has

$$\begin{aligned} \gamma^{\perp} &= 0.93\gamma_0^{\perp} \\ \gamma_0^{\parallel} &= 1.16\gamma_0^{\parallel}. \end{aligned}$$

The model as presented is validated in (Lowe (2001)). For our preliminary study in Section 3.3 we use the a simple approach. Even the approach $\mathcal{H} := 6\pi\mu R$ is troublesome at such microscales, because very fine scales in time and space are required to resolve the hydrodynamic effects. We limit ourselves to $\mathcal{H} = 10$, which was found to be a well balanced choice (see Section 3.4).

3.3 Model Problem Analysis

The intention of introducing a model problem is to start with a model of small complexity where the solution can be computed analytically. From this knowledge one may apply the numerical methods on this model problem and is able to validate implementation and the method itself. On the other hand our main intention still is to find suitable parameter sets for a full description of the filament mechanics according to our approach.

We present a model problem containing three nodes. We define the dimensions of the channel by introcucing a coordinate system with its origin at the bottom left corner of the channel an set the

diameter to 1. The filament is placed skew to a straight channel as shown in Figure 3.3 where each of the two segment has an initial length $l_0 := 1/2$, half the channel diameter. The entry region of the channel is on the x-axis and the fluid flows along the channel in the direction of the y-axis.

We use the following notation (Fig. 3.3): The filament nodes coordinates are X_1, X_2 and X_3

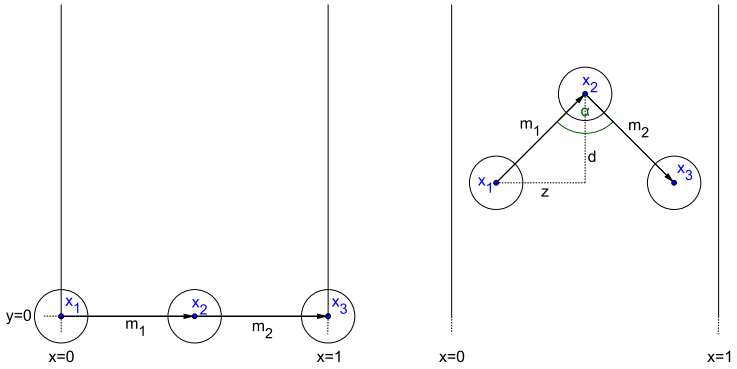

Figure 3.3: Model problem configuration of the three-node filament. Left: The initial state $t = 0$. Right: An arbitrary state.

numbered from left to right in the initial state coordinate system. The coordinates are given by where $X_i = (x_i, y_i), i = 1, 2, 3$. The segments are denoted as l_2 (from X_1 to X_2) and l_3 (from X_2 to X_3). The velocity of the node X_i, $i = 1, 2, 3$ is v_i. In the channel we have constant Poiseouille flow, concretely the velocity profile

$$u(x, y) := 4x(1 - x), \tag{3.17}$$

a parabolic profile with velocity 1 on the centerline. We recall that there is no back-coupling of the filament to the fluid for the simulations of the model problem in this chapter.

3.3.1 Analysis of the Model without Bending Forces

Without yet using a bending force we set up the system for only those two forces and already validate what we defined. We have

$$\begin{aligned}
\dot{X}_i &= v_i \\
\dot{v}_1 &= -\mathcal{H}\,(v_1 - u(X_1)) + \mathcal{S}(l_2 - l_0)\frac{X_2 - X_1}{l_2} \\
\dot{v}_2 &= -\mathcal{H}\,(v_2 - u(X_2)) - \mathcal{S}(l_2 - l_0)\frac{X_2 - X_1}{l_2} + \mathcal{S}(l_3 - l_0)\frac{X_3 - X_2}{l_3} \\
\dot{v}_3 &= -\mathcal{H}\,(v_1 - u(X_1)) - \mathcal{S}(l_3 - l_0)\frac{X_3 - X_2}{l_3}.
\end{aligned}$$

As a first step we simplify the system by combining the two material parameters and define $\omega := \mathcal{S}/\mathcal{H}$. Then the system simplifies to

$$\begin{aligned}
\dot{X}_i &= v_i \\
\frac{1}{\mathcal{H}}\dot{v}_1 &= -(v_1 - u(X_1)) + \omega(l_2 - l_0)\frac{X_2 - X_1}{l_2} \\
\frac{1}{\mathcal{H}}\dot{v}_2 &= -(v_2 - u(X_2)) - \omega(l_2 - l_0)\frac{X_2 - X_1}{l_2} + \omega(l_3 - l_0)\frac{X_3 - X_2}{l_3} \\
\frac{1}{\mathcal{H}}\dot{v}_3 &= -(v_1 - u(X_1)) - \omega(l_3 - l_0)\frac{X_3 - X_2}{l_3},
\end{aligned}$$

where the constants on the left hand side can be neglected for the case of stationary shapes. For any stationary shape, symmetry yields

$$\begin{aligned}
x_3 &= 1 - x_1 \\
y1 &= y_3 \\
x_2 &= 0.5 \\
u(X_2) &= 1 \\
l &:= l_2 = l_3.
\end{aligned}$$

The following six equations remain:

$$\begin{aligned}
\dot{x}_1 &= v_{1,x} \\
\dot{y}_1 &= v_{1,y} \\
\dot{y}_2 &= v_{2,y} \\
\dot{v}_{1,x} &= -v_{1,x} + \omega\frac{l - \frac{1}{2}}{l}\left(\frac{1}{2} - x_1\right) \\
\dot{v}_{1,y} &= -(v_{1,y} - u(x_1)) + \omega\frac{l - \frac{1}{2}}{l}(y_2 - y_1) \\
\dot{v}_{2,y} &= -(v_{2,y} - 1) + 2\omega\frac{l - \frac{1}{2}}{l}(y_1 - y_2).
\end{aligned}$$

We introduce

$$\begin{aligned}
\lambda &:= \omega\frac{l - \frac{1}{2}}{l} \\
d &:= y_2 - y_1 \\
z &:= \frac{1}{2} - x_1.
\end{aligned}$$

To extract one equation for the y-coordinate equations we write $\dot{d} = v_{2,y} - v_{1,y}$ and get

$$\begin{aligned}
\ddot{d} &= -v_{2,y} + 1 - v1, y + u(x_1) - 2\lambda d - \lambda d \\
&= (1 - 4x_1(1 - x_1)) - \dot{d} - 3\lambda d \\
&= 4z^2 - \dot{d} - 3\lambda d.
\end{aligned} \tag{3.18}$$

For the x-coordinate equation we find

$$\ddot{z} = \dot{z} - \lambda z. \tag{3.19}$$

The system now has the form

$$\begin{aligned} \ddot{d} &= 4z^2 - \dot{d} - 3\lambda d \\ \ddot{z} &= \dot{z} - \lambda z. \end{aligned}$$

We complete the system giving the following initial conditions

$$\begin{aligned} d(0) = \dot{d} &= 0 \\ z(0) &= \frac{1}{2} \\ \dot{z}(0) &= 0. \end{aligned}$$

For a stationary shape $\ddot{d} = \dot{d} = 0$ and $\ddot{z} = \dot{z} = 0$ must be fulfilled. This leads to a distinction of cases.

1. $z = 0$: In this case λd must be zero. This is either possible if $d = 0$, which leads to a trivial unphysical case, or λ must vanish. This leads to $l = d = 0.5$.
2. $\lambda = 0$: This implies $z = 0$ and we get also to the case $l = d = 0.5$.

Summary

The one stationary case possible is $z = 0$ and $l = d = 0.5$ meaning the filament is aligned along the centerline and the nodes X_1 and X_3 are at identical positions. The filament approaches the stationary shape faster or slower depending on the parameters $\mathcal{S}$ and $\mathcal{H}$. The segments are observed to cross each other in most of the tested settings in a decreasing oscillations until the stationary overlapping state is reached.

3.3.2 The Bending Forces for the Model Problem

Now we include the bending force as presented in Section 3.2.2. We denote ϑ the inner angle and t_i the vector of unit length along l_i pointing from X_{i-1} to X_i. Again for symmetry reasons we describe only the bending forces of X_1 and X_2. We get

$$\begin{aligned} F^{\mathcal{B}}_{X_1} &= \begin{pmatrix} F^{\mathcal{B}}_{x_1} \\ F^{\mathcal{B}}_{y_1} \end{pmatrix} \\ &= \frac{\mathcal{B}}{l_0}\left[\left(\frac{1}{l}t_2 \cdot t_3\right) t_2 - \frac{t_3}{l}\right] \\ &= \frac{\mathcal{B}}{l_0}\left[\left(\frac{1}{l}(-\cos\vartheta)\right)\frac{1}{l}\begin{pmatrix} z \\ d \end{pmatrix} - \frac{1}{l^2}\begin{pmatrix} z \\ -d \end{pmatrix}\right]. \end{aligned}$$

Note that $\mathcal{B}/l_0 = 2\mathcal{B}$ for the model problem. Componentwise simplified, the bending forces of X_1 are

$$\begin{aligned} F^{\mathcal{B}}_{x_1} &= -2\mathcal{B}\frac{z}{l^2}(1 + \cos\vartheta) \\ F^{\mathcal{B}}_{y_1} &= 2\mathcal{B}\frac{d}{l^2}(1 - \cos\vartheta). \end{aligned}$$

Using the same procedure one finds

$$F^{\mathcal{B}}_{y_2} = -4\mathcal{B}\frac{d}{l^2}(1 - \cos\vartheta).$$

Validation of the Bending Forces

We use three standard cases to validate the formulas.

$$\vartheta = \pi \quad : \quad (1+\cos\vartheta) = 0, d = 0 \rightarrow F^{\mathcal{B}}_{x_1} = F^{\mathcal{B}}_{y_1} = F^{\mathcal{B}}_{y_2} = 0 \tag{3.20}$$

$$\vartheta = \frac{\pi}{2} \quad : \quad F_{X_1} = \frac{2\mathcal{B}}{l^2}\begin{pmatrix} -z \\ d \end{pmatrix} = \begin{pmatrix} -\gamma \\ \gamma \end{pmatrix} \tag{3.21}$$

$$: \quad F_{X_2} = \begin{pmatrix} 0 \\ -4\mathcal{B}d/l^2 \end{pmatrix} = \begin{pmatrix} 0 \\ 2\gamma \end{pmatrix} \tag{3.22}$$

$$\vartheta = 0 \quad : \quad F^{\mathcal{B}}_{y_1} = F^{\mathcal{B}}_{y_2} = 0 \text{ but also } F^{\mathcal{B}}_{x_1} = 0! \tag{3.23}$$

The model shows a weakness for small angles ϑ here. For our purpose very acute angles are not expected and more nodes can always be added to smoothen the filament. The other validation cases for angles at least in the range $[0, \pi/2]$ yield the expected results.

3.3.3 Analysis of the Model with Bending Forces

Using the identities $\cos\frac{\vartheta}{2} = \frac{d}{l}$ and $\sin\frac{\vartheta}{2} = \frac{z}{l}$ we have

$$\begin{aligned} 2\cos^2\frac{\vartheta}{2} = 1+\cos\vartheta &= 2\frac{d^2}{l^2} \\ 2\sin^2\frac{\vartheta}{2} = 1-\cos\vartheta &= 2\frac{z^2}{l^2}, \end{aligned}$$

and we can simplify the bending forces to

$$\begin{aligned} F^{\mathcal{B}}_{X_1} &= \frac{2\mathcal{B}}{l^2}\begin{pmatrix} -z(1+\cos\vartheta) \\ d(1-\cos\vartheta) \end{pmatrix} = \frac{4\mathcal{B}}{l^4}\begin{pmatrix} -d^2 z \\ dz^2 \end{pmatrix} \\ F^{\mathcal{B}}_{X_2} &= \frac{4\mathcal{B}}{l^2}\begin{pmatrix} 0 \\ -d(1-\cos\vartheta) \end{pmatrix} = \frac{8\mathcal{B}}{l^4}\begin{pmatrix} 0 \\ -dz^2 \end{pmatrix}. \end{aligned}$$

We include these forces to the analysis. The six governing equation for the filament including bending forces are given by

$$\dot{x}_1 = v_{1,x} \tag{3.24}$$

$$\dot{y}_1 = v_{1,y} \tag{3.25}$$

$$\dot{y}_2 = v_{2,y} \tag{3.26}$$

$$\dot{v}_{1,x} = -\mathcal{H}v_{1,x} + \mathcal{S}\frac{l-\frac{1}{2}}{l}z - \frac{4\mathcal{B}}{l^4}d^2 z \tag{3.27}$$

$$\dot{v}_{1,y} = -\mathcal{H}(v_{1,y} - u(x_1)) + \mathcal{S}\frac{l-\frac{1}{2}}{l}d + \frac{4\mathcal{B}}{l^4}dz^2 \tag{3.28}$$

$$\dot{v}_{2,y} = -\mathcal{H}(v_{2,y} - 1) - 2\mathcal{S}\frac{l-\frac{1}{2}}{l}d - \frac{8\mathcal{B}}{l^4}dz^2. \tag{3.29}$$

Defining

$$\gamma := \mathcal{S}\,\frac{l-\frac{1}{2}}{l} \text{ and } \delta := \frac{4\mathcal{B}}{l^4},$$

the Equations (3.27)-(3.29) simplify to

$$\begin{aligned}
\dot{v}_{1,x} &= -\mathcal{V}v_{1,x} + \gamma z - \delta d^2 z \\
\dot{v}_{1,y} &= -\mathcal{V}v_{1,y} + \mathcal{V}u(x_1)) + \gamma d + \delta d z^2 \\
\dot{v}_{2,y} &= -\mathcal{V}(v_{2,y} - 1) - 2\gamma d - 2\delta d z^2.
\end{aligned}$$

With the same derivation as without bending forces, we find the system

$$\begin{aligned}
\ddot{d} &= -\mathcal{H}\dot{d} + 4\mathcal{H}z^2 - 3\gamma d - 3\delta d z^2 \\
\ddot{z} &= -\mathcal{H}\dot{z} - \gamma z - \delta d^2 z \\
d(0) = \dot{d} &= 0 \\
z(0) &= \frac{1}{2} \\
\dot{z}(0) &= 0.
\end{aligned}$$

For a stationary shape we demand again $\ddot{d} = \dot{d} = 0$ and $\ddot{z} = \dot{z} = 0$. It remains

$$4\mathcal{H}z^2 = 3\gamma d + 3\delta d z^2 \tag{3.30}$$

$$z\left(\gamma - \delta d^2\right) = 0. \tag{3.31}$$

Determining a stationary state becomes more difficult. Equation (3.31) can be used to make a distinction of cases

1. $z = 0$: This is the unphysical case we mentioned in (3.23).
2. $z > 0$: In this case Equation 3.31 yields $\gamma - \delta d^2 = 0$. Calculations using Equation 3.31 do not give an easy possibility to determine the parameters for the stationary case.

For the upcoming simulations we use the Runge-Kutta method to solve the system of ordinary differential equations, in order to find the stationary shapes of the filament.

3.4 Determining a Tuple of Suitable Parameters

We analyzed over a 100 dead sperm filaments looking for the smallest angles. We use the findings to derive suitable material parameter tuples for the filament simulation. Our approach is to fit

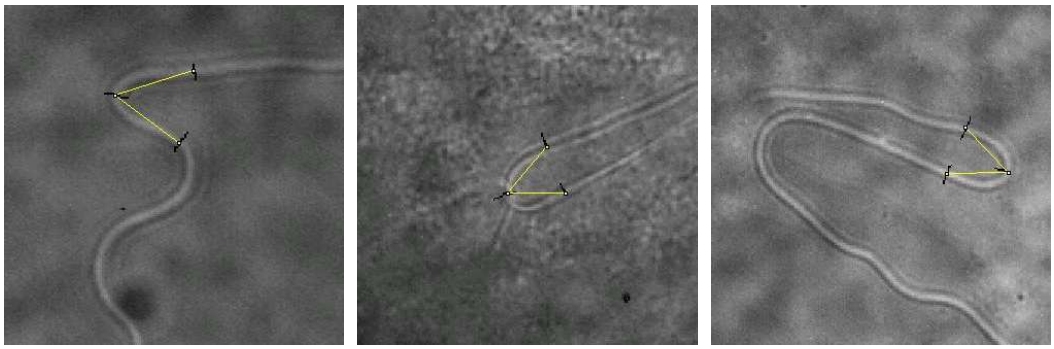

Figure 3.4: The three smallest angles observed from 100 sperm filaments with interpolated three-node filament of segment length 0.5. The zoom is not the same for the three images. The measured angles are shown in Table 3.1

this angle to the mostly bent part of a three-node filament of the length of one duct diameter. We imply that the state of the photographed filament reaches the degree of natural bending and that the same state is also enforced by exposing a filament of length duct radius to Poiseuille flow. The three smallest angles are shown in Table 3.1 and Figure 3.4. Considering these angles, $\alpha_0 := 0.828$

picture number	angle (deg)	angle (rad)
1	54.10	0.944
2	50.19	0.876
3	47.44	0.828

Table 3.1: Measured angles of the three images in Figure 3.4

is found to be an approximation of the most extreme bending the filaments can express in flowing seminal fluid. We are aware that the photographed filaments were not flowing at constant speed in a spermathecal duct. Therefore we emphasize that this is an approach to find approximations of the real material parameters. Our approach is solve the previously described model problem, concretely equations (3.24)-(3.29) and find those parameter tuple that lead to a stationary bending suitable to α_0. A required restriction to the parameter tuple is, that its stationary state cannot exceed a stretched filament length so that the outer corners of the three-node-filament overlaps with the duct boundary. Mathematically, for the segment length l

$$l < \frac{0.5}{sin(\alpha_0/2)} \approx 1.243 \tag{3.32}$$

must hold. Since we know the material of the filaments to be fairly stiff, from the simulations we detected the bound where the stretching is low enough not to influence the process substantially.

Stationary Shape Analyse for $\mathcal{H} = 10$

Although we know that the appropriate constant $\mathcal{H}$ is expected to be bigger (Section 3.2.3), there are computational challenges to resolve the arising effects. Since it imposes already a near inertia-less behaviour to the filament, we restrict the analysis to $\mathcal{H} = 10$ (Buck, 2009). Every simulation consisted of 2000 Runge-Kutta steps at step size 0.01. After these 20 time units, our observations ensure that this is an appropriate approximation to the stationary shape.

Figure 3.5 shows angles and segment lengths of stationary shapes of the parameter test. The angle plots are used to determine candidate parameter triples $(\mathcal{S}, \mathcal{H}, \mathcal{B})$, where the segment plots are used to ensure condition (3.32). The stationary angles increase when $\mathcal{S}$ increases (the filament segments are stiffer). The dependence shows an exponential behaviour (3.5) that was found to be almost stationary for $\mathcal{S} > 100$. The stationary angles also increase nearly linear when $\mathcal{B}$ increases (more resistance to bending). We are mostly interested in those parameter tuples that lead to a

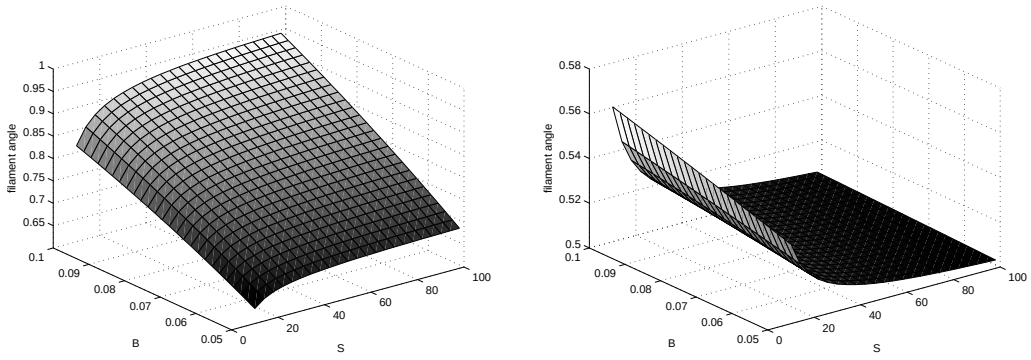

Figure 3.5: Stationary shape analysis results for $\mathcal{H} = 10$. The left plot shows the resulting stationary angle, the right plot shows the stationary segment length.

stationary angle of 0.828. Therefore we fit the corresponding isoline of the left figure in (3.5) to an function that describes the relation of $\mathcal{S}$ to $\mathcal{B}$ concisely. The fitting is shown in Figure 3.6. The resulting regression equations are

$$\mathcal{B}_{\text{linear}}(\mathcal{S}) = 10^4 * (0.767\mathcal{S} - 859.325) \tag{3.33}$$

$$\mathcal{B}_{\text{quadratic}}(\mathcal{S}) = 10^4 * (0.012\mathcal{S}^2 + 3.280\mathcal{S} + 951.466) \tag{3.34}$$

$$\mathcal{B}_{\text{exponential}}(\mathcal{S}) = 0.0753 + 0.0641 * e^{-\mathcal{S}/12.5265} \tag{3.35}$$

For the range of $\mathcal{S} \in [10, 200]$ we found suitable parameter triples

$$(\mathcal{S}, \mathcal{H}, \mathcal{B}) = (\mathcal{S}, 10, \mathcal{B}(\mathcal{S}))$$

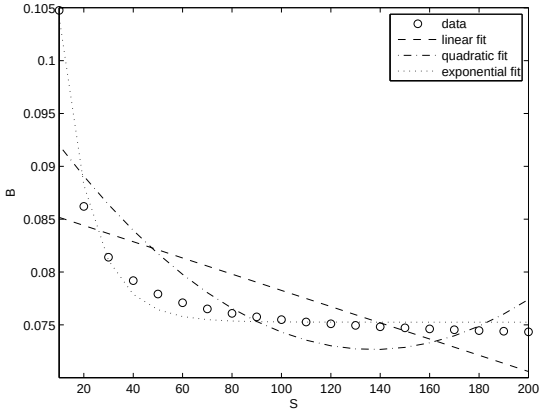

Figure 3.6: Linear, quadratic and exponential fit for the filament angle 0.828.

3.5 Discussion

We recommend the tuple

$$(\mathcal{S}, \mathcal{H}, \mathcal{B}) = (100, 10, 0.075) \tag{3.36}$$

for the simulations of a single filament in the described model. Providing an insight into how the filaments behave in our flow based on this material tuple see Figure 3.7. It shows how the

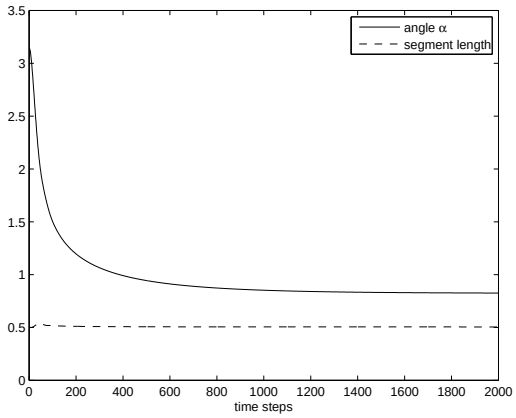

Figure 3.7: The time-dependent shape of the simple filament in a straight channel simulation. The upper curve shows the change of angles in time starting from the initial shape (3.3). The lower curve shows the segment lengths at every time step.

filaments shape (angle and segment length) changes in time. The filaments initial position is horizontal as shown in Figure 3.2. The angle gets smaller and due to the flexibility the segments get longer until bending and stretching resistance and hydrodynamic forces lead to a stationary state.

For bigger parameters $\mathcal{B}$ and $\mathcal{H}$ the stationary condition is achieved much faster.

We recall that the described model is a rough simplification. We build this simple model system to get hand on a suitable parameter tuple. We point out two considerable weaknesses of this choice. On the one hand we used a very simple procedure to find an approximation of the tuple which may be a too rough choice compared to the real values. On the other hand, we omit the force acting from the filament back onto the fluid in this model. The parameters have to be adapted when back-coupling the equations. We discuss in Chapter 4 if the parameters are substantially affected, based on the same experiments solving the back-coupled equations. Nontheless we derived parameter candidates that are ubiquitous for performing simulations in order to achieve new findings that can be compared to the results of Chapter 2.

4

Modelling the Fluid Dynamics of an Immersed Filament

4.1 Introduction

Analyzing the fluid dynamics of a flexible, swimming filament (or fiber) is very challenging, even when an organism's waveform is assumed to be known in advance. In the case of microorganism motility, the low Reynolds number does simplify the mathematical analysis since the equations of fluid mechanics in this regime are linear (1.21). Modelling filaments also at high Reynolds numbers is realised in several applications (Götz et al., 2001, 2008). However, even in the simpler case of low Reynolds numbers, the waveform of a microorganism is an emergent property of the coupled nonlinear system consisting of the organism's force generation mechanisms (active forces), its passive elastic structure (stretching and bending forces), and the external fluid dynamics.

We present a method that solves numerically the equations of motion of a fluid with immersed elastic filaments in a low Reynolds number fluid. It is based on the Immersed Boundary Method (IBM) first introduced by Charles Peskin in the early 1970s for the simulation of the fluid dynamics of heart valves. We use a finite element method for the flow calculation and the filament, which is the immersed boundary, is coupled to the system with the filament description from Chapter 3. An important feature of the method is that the grid of the domain does not have to coincide with the filament nodes, which conserves lots of computational resources.

The dynamics of slender filaments suspended in Stokes flow are fundamental to many applications in biology, physics and engineering. There exists a variety of approaches to describe this models. In our model, the filaments are represented as standalone objects. The coupled equations are treated alternately to exert the fluid force to the filaments and the other way round as shown in Cortez et al. (2004). Beside similar approaches where the filaments are also simulated as objects (e.g.Yamamoto and Takaaki (1992)) one has found many other ways to treat fluid with filaments. In Peskins approach (Peskin and McQueen, 1989), the fibers are massless and treated by modifying the stress tensor. Another promising approach called slender body theory is widely used for filament modelling (Götz and Unterreiter, 2000; Shelley and Ueda, 2000; Tornberg and Shelly, 2004). For the force representation of the filament one applies an integral equation on the filament

centerline.

For the simulations we used the same software as presented in Section 1.4. The implementation of a full model is way too complex to be done in one step of modelling. We realised a preliminary step including a first simulation study comparable to Chapter 2 for the application of yellow dung fly sperm flow. The simulations we perform are thus very simple. Nonetheless they required as a validation of the model and its implementation and as first insight on the influence of the presence of a single filament in Poiseouille flow, comparable to the results of the morphology simulations of Chapter 2. Additionally we can already show, if the back-coupling (the difference to the simulations in Chapter 3) has a pronounced effect.

This stepwise modelling procedure can be compared to the first steps of the work of Charles Peskin on the blood flow in the heart. He started on a basic two-dimensional model ending up years later with a full three-dimensional model (Peskin and McQueen, 1989).

4.2 Coupling the equations: The immersed boundary method

The immersed boundary method was introduced by Charles Peskin to model blood flow around heart valves. It has been advanced to study other problems in biofluiddynamics including three-dimensional blood flow in the heart, dynamics of the inner ear, blood flow in the kidney, limb development and deformation of red blood cells. The classic immersed boundary method introduces by Peskin designates the class of boundary methods where the calculations are performed on a cartesian grid that does not conform the shape of the immersed body. The boundary condition for the boundary of the immersed body are not imposed directly. Instead an extra term is added to the governing equations near the boundary containing the solid-fluid force interaction.

We focus on the immersed boundary method in the context of swimming microfilaments. We assume the fluid to be homogeneous and incompressible. The filaments that comprise the organisms are represented by elastic boundaries immersed in this fluid. The location of the filaments is tracked in a Lagrangian fashion by a collection of massless nodes that move with the local fluid velocity. The coordinates X_k of the filaments nodes are governed by Newton's law

$$\frac{\partial X_k}{\partial t} = V_k \tag{4.1}$$

$$m\frac{\partial V_k}{\partial t} = \sum_j F_j. \tag{4.2}$$

Passing to the limit $t \to \infty$ we get $V = u$, where u is the fluid velocity, and for the filament node positions

$$\frac{\partial X_k}{\partial t} = u\left(X_k, t\right).. \tag{4.3}$$

The effect of the immersed filament on the surrounding fluid particles is captured by transmitting the fiber stress to the fluid through a forcing function term in the momentum equation given by

$$F(x,t) = \sum_k F_k(t)\delta\left(|x - X_k|\right), \tag{4.4}$$

where δ is the Dirac δ-function. Since the nodes of the immersed filaments do no coincide with the cartesian grid points, the Dirac δ-function is not able to transfer the force from the filament onto the grid. To overcome this problem, we replace the sharp δ-function by a smoother distribution d spreading the forcing over a band of elements of the grid around the immersed filament (4.1). The forcing at any grid point x_i as a result of forces of the filament is then

$$F(x_i, t) = \sum_k F_k(t)\, d\left(|x_i - X_k|\right). \tag{4.5}$$

The velocity of the filament nodes in (4.3) is obtained by the same smooth distribution function d.

This function d therefore plays an important role since it is responsible for the transfer of filament forces to the fluid (4.5) and the feedback on the new position nodes of the immersed filament (4.3). While there are different approaches to choose d on a cartesian grid using a finite difference method, we present a straightforward mesh dependant approach of d in the finite element formulation we present in the next section.

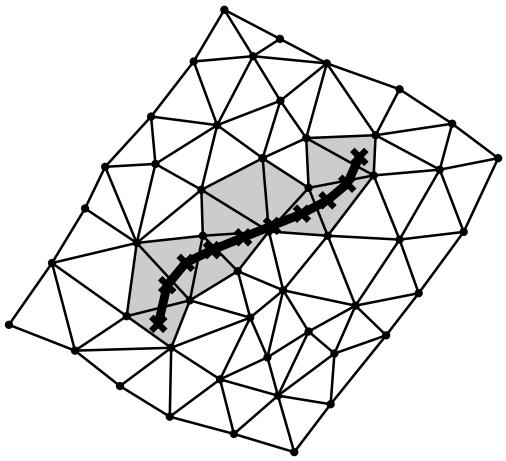

Figure 4.1: Rough visualization of an immersed boundary (thick polygonal line with crosses) that does not coincide with the finite element grid (grid in the background). The gray triangles are affected by the distribution function d

4.3 A Finite Element Formulation of the Immersed Filament Approach

We extend the stationary simulation algorithm of Chapter 1 to a time-dependent algorithm where flow and filament problems are solved alternately. This back-coupling of the filament to the flow problem is the extension to the simulations of Chapter 3.

4.3.1 Governing Equations

Let $\Omega \in \mathbb{R}^2$ be the computational domain containing a massless, elastic, immersed filament. The filament is given as a line of total length L. We represent the curve in parametric form $X(s,t)$ where $t \in [0,T]$ denotes the time and $s \in [0,L]$ denotes the arc length.
Writing the Equations (1.21) for the fluid together with the projections (4.5) and Newton's law, we have

$$\begin{array}{rcll} -\triangle u + \nabla \tilde{p} & = & F & \text{in } \Omega \\ \text{div } u & = & 0 & \text{in } \Omega \\ F(x,t) & = & \sum_k F_k(t)\delta\left(|x - X_k|\right) & x \in \Omega, t \in [0,T] \\ \dfrac{\partial X(s,t)}{\partial t} & = & V(s,t) & s \in [0,L], t \in [0,T] \\ m\dfrac{\partial V(s,t)}{\partial t} & = & \sum_j f_j. & s \in [0,L], t \in [0,T] \end{array} \tag{4.6}$$

We introduce boundary conditions and initial conditions to create a well-posed problem

$$\begin{array}{rcll} u & = & u_D & \text{on } \Gamma_D \times]0,T] \\ u(\cdot,0) & = & u_0(\cdot) & \text{in } \Omega \\ X(s,0) & = & X_0(s) & \forall s \in [0,L]. \end{array} \tag{4.7}$$

4.3.2 Variational Formulation

To get a variational formulation we must know how the term

$$\int_\Omega F(t) v dx \tag{4.8}$$

for a test function v is understood. For a sharp filament representation one can show that

$$\int_\Omega F(t) v dx = \int_0^L f(s,t) v\left(X(s,t)\right) ds \quad \forall t \in]0,T]. \tag{4.9}$$

Let us define $(F(t),v)_{IB} := \int_\Omega F(t) v dx$. The variation formulation reads then as follows:

Problem 6. *Given $f \in L^2\left(]0,L[\times]0,T[\right)$ for all $t \in]0,T[$ find $(u(t),p(t))$ in $H_0^1(\Omega)^2 \times L_0^2(\Omega)$ and $X : [0,L]\times]0,T[\to \Omega$ such that*

$$
\begin{array}{rcll}
(\nabla u(t), \nabla v) + (div\, v, p(t)) & = & (F(t), v)_{IB} & \forall v \in H_0^1(\Omega)^2 \\
(div\, u(t), q) & = & 0 & \forall q \in L_0^2(\Omega) \\
(F(t), v)_{IB} & = & \int_0^L f(s,t) v\left(X(s,t)\right) ds & \forall v \in H_0^1(\Omega)^2 \\
\dfrac{\partial X(s,t)}{\partial t} & = & V(s,t) & \forall s \in [0, L] \\
m\dfrac{\partial V(s,t)}{\partial t} & = & \sum_j f_j & \forall s \in [0, L] \\
u & = & u_D & \forall x \in \Gamma_D \\
u(x,0) & = & u_0(x) & \forall x \in \Omega \\
X(s,0) & = & X_0(s) & \forall s \in [0, L].
\end{array}
\tag{4.10}
$$

The application of the finite element method is done similar as for the stationary method in Section 1.2. For the stationary algorithm, given initial quantities and computational domain, we had to assemble the system and solve to get the solution. For the immersed boundary method the algorithm gets more complex.

4.4 FEM-based Immersed Boundary Algorithm

Suppose that at the end of time step n we have the fluid solution (u_n, p_n) on the computational grid, and the configuration of the immersed boundary points on the filaments (V_k, X_k). To advance the system by one time step, we apply the following algorithm:

1. Calculate the force densities f_k from the boundary configuration;
2. Spread the force densities to the grid to determine the forces F_k on the fluid;
3. Solve the Navier-Stokes equations for u_{n+1};
4. Move each immersed boundary point (X_k) according to Newton's law.

The initial state of the simulation is determined by the initial conditions of (4.10). One can imagine the filament being placed in the domain in its initial shape, where for the first solution the forces of the initial filament shape are already transferred to the flow equations. For the solution of the governing problem we do not expect any regularity. Therefore we apply linear methods. The discretizations should provide $\Delta t \sim h$. For our first fundamental test series, the last missing piece is to find appropriate discretization parameters for the computational simulations. Before we present the simulations, we give a small insight in the implementation of the filament algorithm.

4.5 Implementation and Configuration of the Filament Algorithm

We reflect the tasks of the presented filament algorithm in the view of its implementation.

4.5.1 Programming concepts

In step (1) the force calculation along the filament nodes is calculated. This is straightforward using the formulas and parameters deduced in Chapter 3. The spreading of the force density in Step (2) is realized through a boundary integral along the filament multiplying force density with test functions. The most challenging part of this algorithm is that the immersed boundary does not coincide with the computational boundary of the computational domain. The filament nodes are stored separately and have to be tracked with respect to the finite element grid. This process carries some geometrical challenges due to rounding errors and machine precision. When integrating along the filament (which is moving in each time step) the element edge intersection calculation as well as finding connecting elements has to be treated carefully, in the most extreme case a filament can pass from element to element without one element being the neighbour of the other. It is also possible that the filament segment nearly coincides with a grid edge. In this case we move the filament node a little bit towards the element center and restart the process.
Now that F_k is known in every node of the computational domain, the discrete equation can be solved as for the stationary case (step(3)) and the filament can easily be moved pointwise applying Newton's law (step (4)).

4.5.2 Software features

As presented in Section 1.4.2 for the stationary case, there is an implemented interface so that one can give custom simulation parameters using switches in a console command. Instead of list all switches we give a simple example.

```
java -Xmx2G -Xms2G -cp bin mathcomp.gui.cfd.JCFD
-aassemble.filament.FilamentAssembler:run.NSFilamentAssemblerRun -B0.075
-S100.0 -H10.0 -FromeB0.075S100.0H10.0 -fgrids/ductGrid.grid
```

Description: JCFD is started with 2 GB of memory. The existing grid *ductGrid.grid* and the filament data from *rome.fil* will be loaded. Then the assemble-and-solve uses the Assembler class *FilamentAssembler* and the *NSFilamentAssemblerRun* run class to simulate the filament with bending coefficient 0.075, stretching coefficient 100.0 and hydrodynamic coefficient 10.0.

See Wüst (2009) for a complete feature overview and more implementation details of the filament simulation algorithm.

4.6 Numerical Experiments

We apply the same duct shapes as in Chapter 2. Since the filaments length has a length of about a third of the total duct length, we attach an artificial part on both ends of about the length of the filament as shown in Figure 4.2. Due to stability we scale the whole system to duct length 1. This

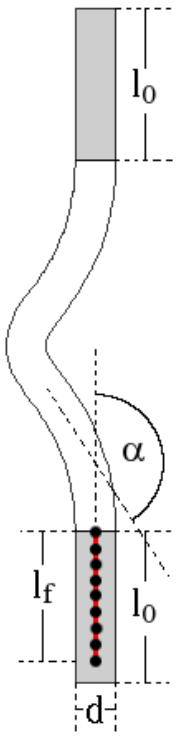

Figure 4.2: The configuration of the duct of width d for the simulation including a single filament. The artificial ends are of length l_0 are shown in grey color. As in Chapter 3, l is the duct length (centerline length) not depending on the angle α. l_f is the length of the filament.

is possible without any other adjustments since we are interested in relative effect sizes and the flow characteristics are not affected by multiplying such this scaling to the very large Reynolds number of the system.

4.6.1 Finding suitable Discretization Parameters

Beside the fixed geometrical parameters from the previous section, we must choose grid resolution, time step size and filament node number to perform the simulation algorithm. For all of these parameters, up to a certain degree where stability is granted, dividing in finer parts is better, but one has to balance those factors. This is due to the limited computational memory but also due to the growing total simulation time. Since the problem is time dependent, we have to perform all four steps of an iteration (e.g. solving the linear system) in each time step. It is not obvious how to find a good balance, because the parameters cannot be independently chosen as

experiments confirm.
As we learned from the numerical experiments in Chapter 2, when considering grids over 10^4 nodes the discretization error does not have a considerable impact in the Stokes flow setting in our smooth channel. However we expect a difference for a complicated filament immersed in the fluid imposing relatively strong forces onto the fluid. Then experiments show that a finer grid is required. We found that a grid of 10^4 nodes to be reasonably balanced to all other factors: We must choose a small time step to resolve the precise path of the filament. This is coupled to the grid resolution: A very fine grid requires a very fine time scale. For the grid of 10^4 nodes the time step we recommend is 0.01. This produces about 1500 time steps for our preliminary simulation (1500 Stokes problems to be solved). $h \sim \Delta t$ is approximately ensured.

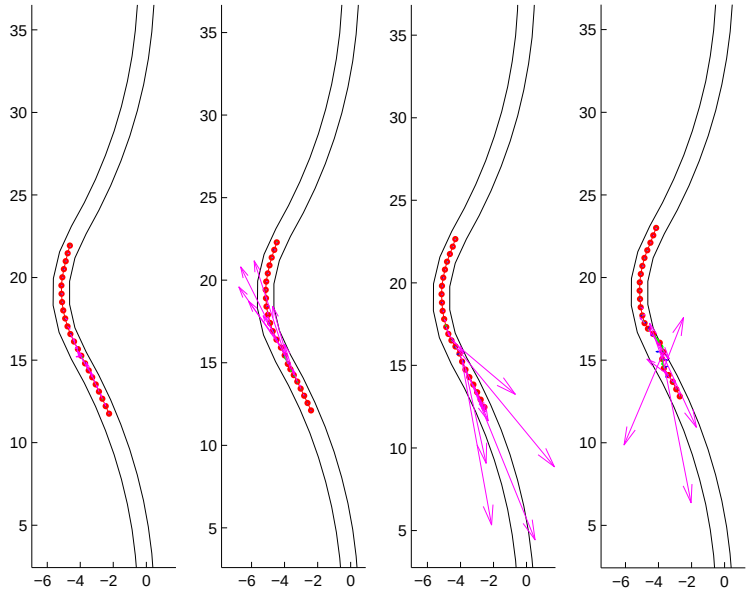

Figure 4.3: A simulation where the discretization parameters were not well balanced. At a fixed time step 0.01 we tried using a finer grid. The time step seems to be to coarse to be able to capture the emerging forces of the filament on the finer grid. The growing arrows represent the hydrodynamic forces which result in an unphysical behaviour of the filament (it exits the duct domain).

Choosing the number of filament nodes is not that related to the convergence of the method. We found that for our preliminary simulations 23 nodes seem appropriate (the equilibrium filament segment length is 0.5). It yields very close results to better resolved filaments, is less costly, and gives already the impression of a smooth filament in animations. For more complex simulations we are aware that the filament needs to be resolved much better since the equilibrium length is half of the diameter of the duct. For the kind of tests we performed it showed not to yield different results if the filament contained more nodes. An overview of the deduced parameters is shown in

parameter	variable	value
artificial area length	l_0	15
filament length	l_f	11
number of filament nodes	N_f	23
inflow velocity (unscaled)	v_{inflow}	4
grid stepsize	h	≈ 0.05
time step	Δt	0.01
stretching parameter	$\mathcal{S}$	100
bending parameter	$\mathcal{B}$	0.075
hydrodynamic parameter	$\mathcal{H}$	10

Table 4.1: Fixed parameters for the filament simulations. The grid was created to have a total of 10^4 nodes, which yields $h \approx 0.05$.

Table 4.1. For further research, suggest a proper rescaling with respect to the filament parameters and the discretization in space and time. Our preliminary work has a clear focus to validate and show the potential of the simulation software and to reveal the differences in the effects sizes compared to Chapter 2.

Deducing Requirements and first Simulations

The left figure in (4.4) shows the initial process of the filament starting in a configuration as shown in Figure 4.2 getting from zero movement to a constant movement. The solid line show the pressure drop at each time step for the filament with the parameters from Chapter 3 and from Chapter 4 on the 5000 node grid. The dashed lines are the pressure drop mean and the pressure drop from the homogeneous problem on the same grid. The acceleration of the bead-spring filament results in a cost during the first 20 time steps. On the right figure we ignore the initial behaviour and see the slight oscillatory behaviour of the pressure drop for the bead spring filament. The oscillation may be caused by too coarse parameters (time and grid discretization).

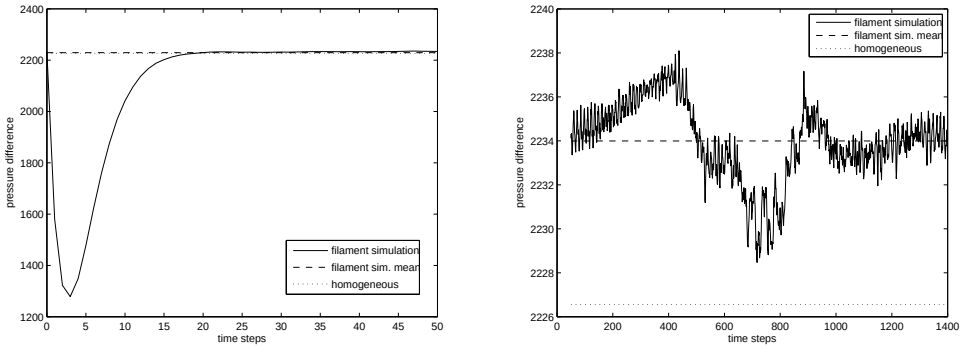

Figure 4.4: Pressure drop measurements of a simulation at the two different time intervals $[0, 50]$ and $[50, 1400]$.

The influence of the back-coupling on the model problem angles

We proposed a tuple of filament parameters in Section 3.5. We used the same parameters for an equal study with the back-coupling. The results are compared in Figure 4.5. The angles are found to be very similar and we do not have do adapt the parameters due to the back-coupling.

4.6.2 Numerical Results

The focus of the upcoming simulations is the comparison to with the tests of Chapter 2. From the knowledge of the effect sizes in the homogeneous case without a filament we can deduce the influence of the single immersed filament to the flow rate. Our main interest is gathering the total time of the filament to reach the artificial outflow area (Fig. 4.2). From those times we will again derive the effect of the morphological parameter on the process of sperm flow through the ducts. Nevertheless we will also address on the pressure difference that we measure and compare the outcome to the results of the homogeneous tests.

Effect of Duct Length

As concluded in Chapter 3, the filament takes proportionally longer to flow through a longer duct (the flow rate decreases linearly with the length of the duct). The mean pressure drop values were

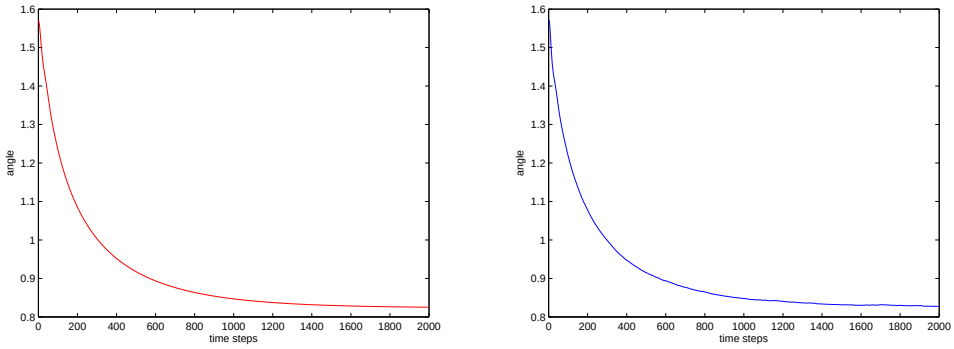

Figure 4.5: A comparing study of the angles depending on time of a simple model filament. Left: The simulation with constant Poiseuille flow. Right The simulation with back-coupling from the filament to the fluid affecting the flow field. The back-coupling does not substantially change the angles.

very close to those of the stationary problem found in Section 2.5. Measuring the time consumed by the filament to flow through the entire duct results in the same dependence to duct length as the mean pressure drop differences.

Effect of Duct Diameter

For a test series using straight ducts with different diameters as well as using a curved duct with different diameters we did find a difference in filament flow times that was proportional to the flow rate stated in Section 2.5. This is due to the fact that the filament is initially aligned with the duct and always swims close to the centerline. Remember that we also do not address to the thickness of the filament, although this may be neglected anyway since $d_{\text{fil}} : d_{\text{duct}} = 1 : 20$. The pressure drop values were very close to those found in Section 2.5.

Effect of increased surface area in a straight duct

The results in Section 2.5 together with the results of Section 4.6.2 already give strong evidence that the effect of increased surface area in the single aligned filament model does not substantially differ to the effect in the homogeneous model. Nonetheless one can imagine a difference if the filament shape is more arbitrary and the filament gets close to (or even interacts with) the rough boundary.

Effect of duct curvature in a smooth walled duct

For a change in the duct curvature we tested the same angle of the same configuration as in Section 2.5. In Figure 4.6 we show the flow times and the pressure drop means of this simulation. The effect size is found to be similar to Section 2.5. The characteristic of the time plot of Figure 4.6 can also be found in Figure 2.5.

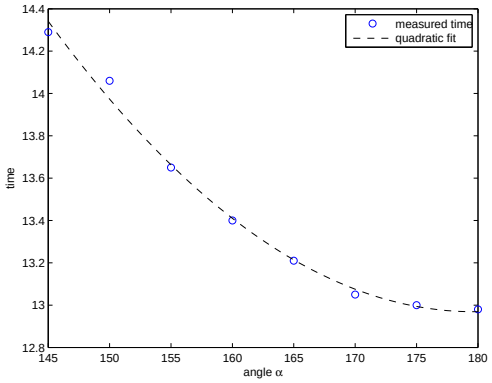

Figure 4.6: Time consumption of the filament to swim from one artificial end to the other (4.2) for different duct curvature angle α.

4.7 Discussion

The presence of an aligned single immersed filament did not substantially change the flow behaviour compared to the results of Chapter 2. We see several interesting model refinements that are inspired by this basic study. The energy that the filament consumes by changing its shape influences the flow. Therefore different initial shapes as observed from real images (e.g. waveforms) could lead to an intensified effect of the morphological parameters. It is considerable that the single filament collides with the duct wall or even gets stuck. Once a proper collision treatment is implemented, one could introduce multiple filaments that interact with each other (e.g. Zhu and Peskin (2002) successfully modelled and validated an IBM algorithm that models two interacting filaments in a soap film in two dimensions).

We did not include the filament locomotion at all. There are several approaches (e.g. Lighthill). In order to simulate the success of a self-propelled sperm filaments to reach the spermatheca there were very interesting question arising. For the uncoupled systems Buck (2009) performed simulations using motorized filaments using the approach presented in Lowe (2001).

In the literature one finds illustrations of many different duct shapes, from straight to highly compressed. We know that the ducts are flexible and certainly moving while the sperm is flowing through. Thus another putative model refinement is to include a time-dependence in the duct shape, governed by pulsating boundaries, or the muscle attached to the spermatheca.

We have found candidates for adaptive morphology parameters that influence sperm flow in yellow dung fly ducts by building the first few steps of a mathematical model. To clarify if this model already captures the main sperm transport mechanics we set up a laboratory experiment. The aim is to validate this simulation results and find new insight in the mechanics and avenues for future research.

5

How female reproductive tract morphology affects sperm movement in yellow dung flies

Christian Wüst (A,B), M.Demont (A), C.Buser (C), L.F.Bussière (A,D)

(A) Zoological Museum, University of Zurich (B) Institute of Mathematics, University of Zurich (C) EAWAG: Swiss Federal Institute of Aquatic Science and Technology (D) School of Biological and Environmental Sciences, University of Stirling

Abstract

The extent to which female structures adaptively control sperm transport and use is controversial. This is partly because few studies can unambiguously separate male and female influences on sperm storage, and there are consequently few data demonstrating a female role in biasing sperm storage. In previous work, we used fluid dynamics theory to show that some aspects of female morphology are much more likely than others to affect sperm movement within female yellow dung flies (Scathophaga stercoraria). Here we attempt to validate this theory empirically by studying how natural variation in female morphology influences sperm movement in experimentally-controlled matings, and by estimating the proportion of variation in insemination that is accounted for males and females. We found substantial variation among spermathecae in the number of sperm stored which was considerably greater than variation among males in total sperm transferred. Our analyses also confirmed a predicted substantial effect of spermathecal duct length on sperm movement. In contrast, whereas theory predicted a linear effect of duct diameter on sperm flow, we found support only for a nonlinear effect. This last result suggests several possible mechanisms that might contribute to sperm movement in these flies that await future theoretical and empirical investigation.

5.1 Introduction

Some of the most extraordinarily diverse structures in the animal kingdom are those associated with the reproductive tract (Eberhard, 1996). This fact has long been recognized by systematists, who have frequently used genitalic morphology as a means of distinguishing closely related taxa. Much of the diversity in reproductive traits is thought to arise via some form of sexual selection involving adaptive coevolutionary changes in females and their mates across species (Arnqvist, 1998). Nevertheless, exactly how female structures select on males remains controversial, especially with respect to the importance of conflicts of interest in driving coevolution.

Classic models of mate choice propose that female structures exert selection on males in order to increase female fitness, and one of the most exciting aspects of a potentially active female role in post-copulatory events was that it suggested very compelling evidence for adaptations that promote indirect fitness (e.g., good-genes sexual selection) (Eberhard, 1996). More recent arguments have focused on sexually antagonistic coevolution (i.e. sexual conflict between male and female adaptations), and they posit that direct selection on females (i.e. for increased fitness within the current generation) should be more important than indirect selection (which is only ever exerted on the offspring of a female (Cameron et al., 2003; Kirkpatrick and Barton, 1997).

Convincing evidence that a given reproductive structure in females has evolved in one of these contexts rather than the other is elusive. Several imposing challenges make evaluating these models difficult. (1) Many of the traits in question are very small, and often hidden within the bodies of the organisms even during copulation, so opportunities for direct observation are few. (2) Both direct and indirect selection hypotheses involve interactions between females and their mates, so that the traits cannot be functionally observed in isolated individuals. (3) The alternative models generate predictions that tend to differ only subtly, especially under the stable equilibrium conditions in which coevolutionary interactions for most populations are thought to exist.

Evolutionary ecologists have long argued about the nature of evidence required to overcome these challenges and convincingly separate male effects from female effects (because effects that are purely male-generated require no adaptive explanation for females). After having established a female influence, the challenge becomes determining whether this influence may have evolved in the context of sperm choice or sexually antagonistic coevolution. The most famous exchange on the subject was stimulated by Birkhead (1998) who presented three criteria for demonstrating sperm choice that were built around a classic experiment by Lewis and Austad (1994) that assigned variation in paternity across the sexes: (1) that there be variation in paternity within the population; (2) that some of this variation be attributable to males, and (3) that some of this variation be attributable to females. In a series of responses to this work, Eberhard (2000), Kempenaers et al. (2000) and Pitnick and Brown (2000) argued that these conditions were neither necessary nor sufficient for demonstrating sperm choice, and they and Birkhead (Birkhead, 2000) agreed that more studies of the mechanisms underlying sperm choice would be a very useful complement to analyses that assigned variation in paternity to one sex or the other. Since this interchange, several studies have estimated the male and female contributions to variation in paternity in several species (Tregenza et al., 2009; Wilson et al., 1997; Corley et al., 2006).

In contrast to this progress in studying the relative contributions within and between the sexes to the outcome of paternity, the mechanisms that produce this outcome remain poorly resolved even in well studied systems. Evidence is mounting that intersexual coevolution is a major force in determining genitalic diversity (House and Simmons, 2003; Presgraves et al., 1999; Wenninger

and Averill, 2006; Miller and Pitnick, 2002; Minder et al., 2005). Specifically, several papers document a clear role for intersexual conflict in driving reproductive trait evolution (Reinhardt et al., 2007; Arnqvist and Rowe, 2002; Rowe and Arnqvist, 2002). There is also some evidence consistent with sperm choice (Birkhead, 1998, 2000). These intriguing papers notwithstanding, direct evidence that genitalic diversity is promoted by adaptive sperm choice is lacking. It is not clear whether that is because demonstrating indirect benefits is inherently difficult, or because they are an uncommon cause of diversifications in female genital morphology.

As discussed in Chapter 2, our study system, yellow dung flies (Scathophaga stercoraria) are a model system for post-copulatory sexual selection. Females have three sperm storage organs, one called the singlet spermatheca, and the others the middle and outer doublet, which are located on the opposite side of the body. These organs seem to have independent musculature. The male cannot control movement of sperm into these organs, because the male intromitent organ only inserts up to the bursa copulatrix (Hosken et al., 1999). There is compelling evidence that the complex reproductive morphology of females may play a role in adaptive sperm choice . In the current study, we set out to correlate some aspects of female reproductive tract morphology with sperm storage patterns, and to conduct with a variance components analysis that partitioned sperm storage across males, females, and sperm storage organs.

In contrast to the most of the previous work on adaptive sperm choice, we focus on variance in the number of stored sperm rather than the paternity of offspring. This current study represents an attempt to achieve several aims: (1) a validation of the theoretical work described in Chapter 2, in other words to test whether the parameter effects in the theoretical work are aligned with observations of the real biological system; (2) to suggest directions for model refinements that might improve the realism of the numerical simulations; and (3) to explore variation in sperm storage within and among females as a function of male and female identity, sperm storage site, and morphological aspects of the reproductive tract. In light of these objectives, we subjected a series of females to copulations of closely controlled duration, and counted the sperm in each of the female's sperm storage organs as a function of several factors and morphological covariates. We also partitioned variation among random effects to determine the proportion of phenotypic variation accounted for by males, females, and spermathecae as well as unexplained residual variance.

5.2 Materials and Methods

Prior to the experiment, we collected fresh cow dung at our field site in Fehraltorf, Switzerland, homogenized it and froze it at -80 degrees for over two weeks to kill any invertebrates that had colonized it. We collected 75 mating pairs of yellow dung flies from the same field site, and induced oviposition in the laboratory by placing pairs in a small glass vial containing a filter paper with a small quantity of thawed dung, and transferred eggs to plastic bottles containing enough dung to prevent larval competition (at least 2 g dung per larva, Amano (1983)). At eclosion, all flies received ad libitum sugar, water, and *Drosophila* in order to bring about sexual maturity and were held at 21 degrees and 65% humidity. 21 days after eclosion, we mated 20 males to three non-sibling females each ($N = 60$ females). We interrupted copulation after exactly 20 minutes for every pair. Females were then submerged in liquid nitrogen to arrest sperm movement, and transferred to the freezer in individual tubes for subsequent dissection. We chose the duration of 20 minutes of copulation for because we wanted to ensure that all copulations proceeded for the same amount of time, so we chose a copula duration substantially shorter than the average. Our interest is primarily in the influence of morphological parameters on sperm storage, so even if the total number of sperm that reach the sperm storage organs in our study is an underestimate of per-copula sperm transfer, differences between spermathecae may nevertheless reveal the effects of morphological parameters on sperm movement.

After thawing the flies prior to dissection, we placed the flies in water and carefully removed the female reproductive tracts using forceps. We photographed the entire reproductive tract as it lay in a drop of water on a microscope cavity slide under a coverslip for later digital measurements of the predictor variables duct length (ductL), minimal duct diameter near spermatheca (ductW), minimal duct diameter near the bursa (ductZ), minimal duct diameter at the outflow into the bursa (ductV), and the spermathecal area, which was recomputed by the spermathecal volume calculation described in Appendix B. We then carefully separated the spermathecae and individually emptied them on a separate slide into a tiny drop of DAPI medium (Vectashield HardSet Mounting Medium with DAPI) for subsequent sperm counting under the fluorescent microscope. We carefully disrupted the sperm using forceps coated with Sigmacote to prevent sperm from sticking to the forceps and covered the solution with a coverslip. To ensure that the sperm were spread enough to be counted, we carefully displaced the coverslip several times before placing the slides in a light impervious box. We stored the slides in darkness at 4 degrees C until counting. At the fluorescent microscope, we counted all the sperm from each spermatheca by conducting transects of the coverslip that were the width of the field of view.

In addition to sperm counts and the morphological measures described above, we recorded the wet masses and hind tibia lengths of females (fHTL) and their male partners (mHTL). We used the image processing software ImageJ (Rasband, 2009) to measure linear distances in digital photographs captured by a camera mounted on a compound microscope. For the analysis, we used the lme function of the NLME package (Pinheiro et al., 2009) in the R Project software (R Development Core Team, 2009) to fit linear mixed models of the influence of the predictor variables on sperm number in spermathecae nested within females nested within their male mates.

For the linear mixed model analysis we applied the nesting

```
1 random=~1|mID/fID/spthNr
```

The effect of the spermatheca number within the females is a pure female effect and the number of the female in the mating line within the male is a specific male-by-female interaction but with a variation unique to the female individual. Both effects were thus captured by the model and will be explained in the variance component analyze. We log-transformed sperm counts to achieve normality, we started with a model including all quadratic terms and all the two- and three-way-interactions as the initial fit for the analysis. We then removed in a stepwise fashion the higher-order terms that resulted in the highest reduction of the AIC value of the model (using the stepAIC function of the NLME package (Pinheiro et al., 2009) for the R software R Development Core Team (2009)).

5.3 Results

We set up 50 mating tetrads (each containing one male and three, non-sibling females haphazardly selected from 60 half-sib families collected from wild females). For six of the 50 tetrads the males did not mate with any of the three females. In 16 tetrads male mated one or two females, and in 28 tetrads males mated for the full 20 minutes with all three females. In a few cases ($N = 4$) we lost material during dissection and measurements. Our analysis is therefore based on the first 20 successfully dissected and photographed complete tetrads.

We found remarkable variation in sperm storage, with an average of 423 ± 465 sperm per spermathecae. The range included a couple of spermathecae with no sperm. In three females sperm transfer was not successful at all, where in the other cases there were non-empty spermathecae along the empty ones within the females. The maximal number of sperm in a single spermatheca was a count of 1798 filaments. There was an intriguing pattern of bias in spite of this high variance, with the singlet storing 523 sperm, the middle doublet 442 and the outer doublet 293 sperm.

In the process of taking the photographs of the female anatomy we observed a previously undescribed structure at the very opening of the duct in the bursa (Fig. 5.1). Because of the resemblance of this structure to valves, we wanted to explore its possible role in regulating sperm movement even though this structure could not be seen in all preparations. For each preparation, we noted whether the structure was visible and measured the minimal diameter of the distal 'valves' for each duct (ductV), and included this as a covariate in a separate group of linear mixed models.

For the spermathecae, we observed 9 ducts with two spermatheca (these flies had 4 spermathecae) and 8 ducts with two adnated spermathecae. We flagged the ducts (spthT) and measured length and width to apply the according mathematical formula for each type to find appropriate volume approximations. We applied the cube root to volume measurements in order to have a common length scale parameter. We fitted a linear mixed-effects model by maximizing the restricted log-likelihood (Laird and Ware, 1982) but allowing for nested random effects. Our fixed effects included all the measured covariates: duct length (ductL), minimal duct diameter near spermatheca (ductW), minimal duct diameter near the bursa (ductZ), minimal duct diameter at the outflow into the bursa (ductV, if we did not observe the valves we set this equal to ductZ), male and female hind tibia length (mHTL, fHTL) and the cube root of the estimated spermathecal volume (spthVolCR). The random effects include male identity (mID), the copulation in question (fLocal, 1-3) nested within the male identity, and the spermathecal identity (spthNr) nested within copulation nested within male.

In the analysis, the resulting best model is summarized in Table 5.1, and contains two parameters that significantly predict sperm number: duct length (ductL) and the quadratic term for minimum duct diameter near the bursa (ductZ^2). The duct length has a negative parameter estimate of -0.153 meaning that the longer the duct the fewer sperm were found in the spermatheca. The ductZ^2 term has a very small -0.078 parameter estimate, indicating that the greatest number of sperm travelled through ducts of intermediate thickness.

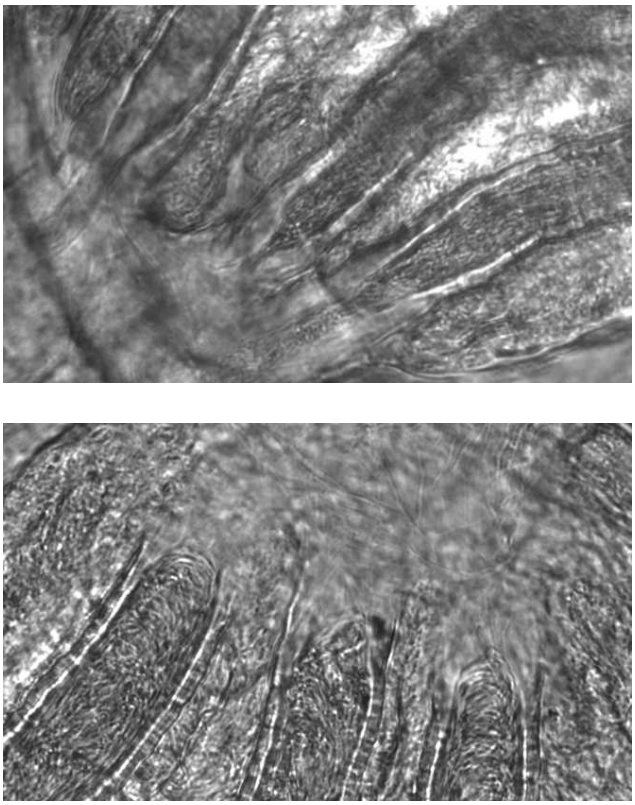

Figure 5.1: Two microphotographs that show the valve-like structure where the ducts lead into the bursa. The upper photograph clearly shown an opened valve (duct on top-left) and a closed valve (other two ducts). In the second photograph the ducts and the bursa are two separated fluid domains, separated by the valves, acting like a gate.

Variance Component Analysis

One of the advantages of the linear mixed modelling approach is that we can not only control for variation within and among females, but we can also estimate how each nesting level contributes to total variation in sperm numbers. The variance components for random effects associated with the model described in Table 5.1 are summarized in Table 5.2.

	numDF	denDF	F-value	p-value
(Intercept)	1	94	396.6435	$< .0001$
mHTL	1	17	0.0057	0.9406
fHTL	1	31	1.1127	0.2997
spthVolCR	1	94	1.2788	0.2610
ductL	1	94	6.3547	0.0134
ductZ	1	94	0.0813	0.7762
I(ductZ^2)	1	94	5.1310	0.0258
mHTL:ductL	1	94	3.6360	0.0596
fHTL:ductZ	1	94	1.6518	0.2019
ductL:ductZ	1	94	2.6532	0.1067

Table 5.1: The anova table for the minimum adequate model describing the influence of male and female phenotype on sperm transport.

	Variance Component	Percentage
Male identity	0.11077	2.79
Copulation	2.28144	57.50
Spth within Female	1.35249	34.09
Residual	0.22320	5.62

Table 5.2: The variance components for random effects in the minimum adequate model described in Table 5.1.

5.4 Discussion

We estimated sperm storage across spermathecae in a number of females and analyzed how it was affected by the phenotypes of males and females and female reproductive tract morphology.

As predicted in Chapter 2, we found that duct length has a negative linear effect on the sperm count. The effect sizes are however not directly comparable since we have apply different model involving different parameters. For the fixed inflow model described in Chapter 2 we found duct width had the largest (positive) effect on the sperm count. Our empirical analysis however showed a small but significant quadratic effect (-0.078) for the minimal duct diameter near the bursa. This relationship might be explained if the diameter changes plastically during insemination when females wish to restrict flow, perhaps using peristaltic waves of contraction along the length of the duct. Alternatively, perhaps swimming sperm move most quickly in intermediate ducts, because extremely narrow ducts are insufficiently wide for sperm swimming, but

extremely wide ducts do not allow sperm to push against the walls. In Chapter 2, the strongest effect was for duct width. Notwithstanding the complications of nonlinear effects due to effects of duct movement or sperm swimming, it is notable that we find nothing approaching the effect size predicted. This mismatch shows us that we need more insight in the sperm transport mechanisms and simultaneously refine the model to find the true mechanisms governing sperm flow in yellow dung flies.

Another possible mechanism we thought might regulate sperm flow were the newly discovered valve structures shown in Figure 5.1. We had thought these might could operate like a dynamic gate that restricts in and outflow of sperm, and that narrow gaps between valves might be associated with reduced sperm movement. We observed this structure in the impressive microphotographs in Arthur et al. (2008) (Figure 2c shows an open gate; Figure 2d shows accumulated sperm before its outflow into the bursa). However, including our static measurements in the model did not help predict sperm number. Although there is still little support for such a structure playing a strong role in sperm sorting (at least within virgin flies), it may stimulate future experiments and it could be easily included and studied in our flow simulation software.

Our nested experimental design allows us to partition the variance in sperm numbers across males and females as well as across spermathecae within females. The variation in total sperm number attributable to males is rather small, but this should not imply that there are no meaningful differences across males in sperm storage. Our analysis only partitions variation in sperm transferred, so while males seem to transfer negligibly different numbers of sperm overall as a result of their identity, it is not clear how much their performance in achieving fertilization might vary by individual. Nevertheless, this result does argue against systematic differences across males in their ability to inseminate virgin females, and is therefore a significant novel contribution of our study.

The level of nesting encoded by individual females (which accounts for 57.5% of the variance in sperm numbers) represents variation arising from the specific male-by-female interaction represented by the single mating each female experienced. Some of this variation might be unique to females, but we cannot estimate how much because we obviously could not repeat the experiments for the same female twice after dissecting her. Perhaps the most intriguing aspect of our variance components analysis is that over one third of the variation in sperm numbers is represented by the spermatheca level. Since there males cannot place their sperm directly into the spermathecae (Hosken et al., 1999), the within female component of the variance (34.1%) arguably represents female-controlled aspects of sperm sorting, which would obviously be impossible in a system with a single sperm storage organ.

We decided to disregard the sperm stored in the spermathecal ducts themselves, since we could not reliably isolate these without loss in the same way that we are confident we have done with the spermathecae. A rough calculation of the volume of fluid contained within ducts versus spermathecae vindicates our approach: the approximated volume of spermathecae is on average 10 times bigger than the volume in the duct found by our measurements. The corollary of this finding is that the spermathecal duct, while it may contain sperm, is probably primarily an adaptation for female control rather than for sperm storage itself.

We have supported a clear role for duct length in affecting sperm flow, but for other reproductive tract characters that were measurable, we were unable to support predictions based on only

passive flow. This work represents a decided step forward in determining the mechanisms underlying sperm storage biases in yellow dung flies. Obviously, much work remains, particularly in pursuing experiments and theoretical models that stray less from the natural system in terms of the number of interacting individuals and the conditions of mating and oviposition. Further, we recognize that we will ultimately need to determine biases in sperm use as well as storage, and the consequences of these biases for the fitness of females and their mates. Meanwhile, the current work is very useful in indicating which of the many possible directions for further research are likely to be the most rewarding.

6

Conclusions

Our goal is to enlighten the transport mechanics of yellow dung fly sperm flow and give directions for future experiments. We apply the novel modelling approach of numerical computer simulation to provide an insight into the mechanics of sperm flow in yellow dung flies. The arguably biggest advantage of the simulation to real experiments is the flexibility and the ease of repeatability.

We performed systematic parameter tests for a homogeneous approach. The results indicated that if this model is already appropriate, the duct diameter (and the increased surface area depth) should have an overwhelming influence on the flow rate. Duct length should be much smaller in its influence and duct curvature is almost negligible. The simple filament model reproduced the same results concerning a preliminary parameter test of a centerline-aligned filament.

The validation experiment in Chapter 5 however showed us, that there are other mechanisms beyond our currently implemented model. Although we supported a clear role for duct length, duct width was not found to have the expected impact. We suggest a variety of different mechanisms underlying these observations. From the nested design of the experiment we were able to detect female-controlled aspects of sperm sorting. Moreover a new structure was detected to be a putative mechanism to control sperm transport.

This work contributes a significant step forward in determining the mechanisms underlying sperm transport and storage in yellow dung flies. Our findings lead to a set of model refinements that we suggest as next steps (e.g. filament interaction, three dimensional model, valve modelling, moving boundaries) of finding a better, more detailed model to simulate yellow dung fly sperm flow. The implication of our research indicate a big variety of possible directions for future research in biology to precise the mechanisms of sperm transport.

Appendices

A

Deducing the Flow Rate Effect Size from the Computational Experiments

A.1 Introduction

The homogeneous formulation of the model we applied for the simulations in Chapter 2 uses a fixed inflow velocity. This is due to the simpler mathematical treatment of the governing equations instead of a fixed pressure formulation. The response variable of the computational experiments is the difference in pressure from inflow edge to outflow edge. In other words we find out how the pressure drop depends on several parameters.

A.2 The Model Problem

We consider the dimensionless Stokes equation in two dimensions on a channel of diameter $W = 2a = 1$ and length $L = 40$, given as

$$
\begin{aligned}
-\triangle u + \nabla f &= 0 \text{ in } [-1/2, 1/2] \times [0, 40] && \text{(A.1)} \\
u(x, y) &= v_{\max}\left(1 - \frac{x^2}{a^2}\right) \text{ on } \Gamma_{\text{in}} \cup \Gamma_{\text{side}} && \text{(A.2)} \\
(\nabla u - p) \cdot n &= 0 \text{ on } \Gamma_{\text{out}}. && \text{(A.3)} \\
& && \text{(A.4)}
\end{aligned}
$$

For this special case we can give the unique exact solution:

$$
\begin{aligned}
u(x, y) = u(x) &= v_{\max}\left(1 - \frac{x^2}{a^2}\right) && \text{(A.5)} \\
p(x, y) = p(y) &= \frac{2v_{\max}(L - y)}{a^2}. && \text{(A.6)}
\end{aligned}
$$

It follows that the pressure gradient is a constant:

$$\frac{\partial p(y)}{\partial y} = -\frac{2v_{\max}}{a^2}.$$

Pouseuille's law states

$$\dot{Q} = -\frac{2}{3}a^3\frac{\partial p(y)}{\partial y},$$

and other hand we know from the given inflow that

$$\dot{Q} = \int_{-a}^{a} v(x)dx = \frac{4}{3}v_{\max}a.$$

A.3 Deducing the Flow Rate Effect Size

We discuss below how each of the parameters influence the flow rate.

Duct Length

Since the pressure gradient is constant, doubling L doubles the pressure drop $p(0) - p(L) = p(0)$. Halving the inflow by halving $v_{\max}$ restores the pressure drop. Therefore we have

$$\dot{Q} \sim 1/L.$$

For the effect size calculation we we have $L = 672 \pm 17\mu m$ and find

$$c_{\text{DL}} = \frac{689}{655} = 1.0519.$$

Therefore, in the given range of two standard deviations $L_{\min} = 655$, $L_{\max} = 689$ the effect of duct length on flow rate is $1 - 1/c_{\text{DL}} = 4.9\%$.

Duct Width

Again we want to fix the pressure and compare the flow rate for different radii a. Since the pressure gradient remains the same, Poiseuilles law gives us

$$\dot{Q} \sim a^3.$$

The range in radii of two standard deviations is $a_{\min} = 11.7$, $a_{\max} = 15.3$ we have

$$c_{\text{DW}} = \frac{15.3}{11.7} = 1.3077.$$

Therfore, in this range $L_{\min} = 655$, $L_{\max} = 689$ the effect of duct length on flow rate is $1 - c_{\text{DW}}^3 = 123.6\%$.

Duct Wall internal Surface Area (the presence of microvilli)

The exact solution for these tests is not known. We know the pressure loss from the straight duct and from the narrowed duct (they are verified with the exact solution). The pressure loss of the duct with microvilli is obviousely between the two values. As for duct length we have a fixed inflow and different pressure loss values. We get analogously

$$\dot{Q} \sim 1/\text{MV}.$$

From micrographs provided by Hosken et al. (1999) reveal microvilli having an amplitude of 0.5 and a period of approximately 1.5. The software computes $p(0)_{\text{straight}} = 105.35$ and $p(0)_{\text{mv}} = 121.61$. Then, with

$$c_{\text{MV}} = \frac{121.61}{105.35} = 1.15$$

we derived the effect of roughness on flow rate to be $1 - 1/c_{\text{MV}} = 13.3\%$.

Duct Curvature

As for the duct width, the length stays at L. Again the exact formula is not known analytically. But once we have $p(0)_{\text{straight}}$ we can find the flow rate so that an equal pressure loss results for the curved duct with computational experiments. We find that

$$\dot{Q} \sim 1/\text{CURV}.$$

is a very good approximation. We compare $p(0)_{\text{straight}} = 105.35$ to $p(0)_{\alpha=125} = 107.01$ and with

$$c_{\alpha} = \frac{107.01}{105.35} = 1.0155$$

we get $1 - 1/c_{\text{CURV}} = 1.55\%$.

B

A Study on Spermathecal Volume and Sperm Number

In this appendix chapter we present a technique to approximate the volume of the spermathecae from the microphotographs we took for the study of Chapter 5. Especially the volume calculation of two intersecting spermathecae (Ward, 2000) is not obvious, since only the combined duct width and the lengths of the intersecting spermathecae can be measured. In the second part of the chapter we derive an estimate of the number of sperm filaments that fit in a single spermatheca on order to compare them to the counted numbers in Chapter 5.

B.1 Calculating the Volume of a Spermathecae

The parameters width (w) and length (l) can be extracted easily and it turns out that in general $w < l$ holds. The volume of a *ellipsoid* is given by

$$V_{\text{ellipsoid}} = \frac{4}{3}\pi \left(\frac{w}{2}\right)^2 \left(\frac{l}{2}\right) = \frac{\pi}{6} w^2 l.$$

Among the dung fly females there is variation in the number of spermathecae (Ward, 2000). Usually they have three but sometimes four spermathecae. From observations, among the two regular duct with single spermathecae, there is either one more regular spermatheca or two more regular spermathecae (Fig. B.1, right figure) or an adnated state in between (Fig. B.1, left figure).

We will estimate the volume of such two intersecting organs.

Let t be the part of the radius that is cut by the intersection. The quotient of the volume that cut by given radius and t is given by

$$Q(r,t) := \frac{V_{\text{cut}}}{V_{\text{sperical}}} = \frac{1}{4}\left(2 - 3\left(\frac{r-t}{r}\right) + \left(\frac{r-t}{r}\right)^3\right). \tag{B.1}$$

To estimate the volume of the intersecting spermathecae we do the following:

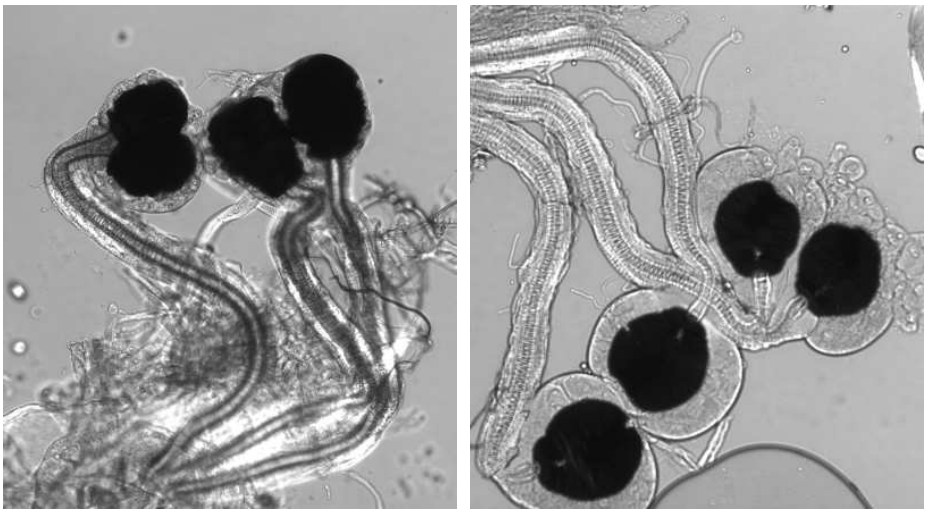

Figure B.1: Left: Three spermathecae containing an adnated pair. Right: Four separate spermathecae.

1. Measure the total width W of the adnated spermathecae and the mean length L.

2. Use the average factor $q := w_{\text{mean}}/l_{\text{mean}}$ from all non-overlapping spermatheca measurements and the identity $r = qL/2$ from the separated organs to calculate t by

$$t = 2r - \frac{W}{2} = qL - \frac{W}{2}.$$

3. Calculate $Q(r,t)$ using equation B.1 to find the estimated volume of the two intersecting spermathecae by

$$V_{\text{inters}} = 2\left(V_{\text{ellipsiod}}(1 - Q(r,t))\right)$$

B.2 An Upper Bound to the maximal Number of Sperm in a single Spermatheca

We give an upper bound to the number of sperm that can be stored at a time in a single spermatheca by calculating the quotient of spermatheca volume and single sperm volume.

B.2.1 Approach I: Cylinders in a Sphere

We model the spermatheca by a ball with diameter D and the sperm as a zylinder with length l and diameter d. Then the upper bound of the sperm number is given by

$$\mathcal{N}^{\text{Approach I}}(D,d,l) = \frac{2}{3}\,\frac{D^3}{d^2 l}.$$

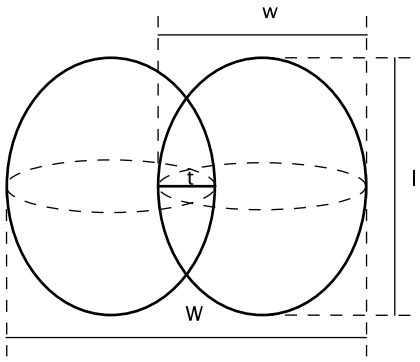

Figure B.2: The cross section of an adnated pair of spermathecae. In our measurements and the volume calculation we capture the fact that the size of the two spermathecae may also be different.

Applying the measured quantities to this simple model we get the following rough estimate of the upper bound

$$\mathcal{N}^{\text{Approach I}} = \frac{2}{3}\,\frac{(180)^3}{(2)^2 \cdot 200} \approx 3957.$$

B.2.2 Approach II: Head-Tail Object in an Ellipsoid

Let now the spermatheca be a spherical with length L and width W and the sperm a tail/head object. The tail is modelled as a cylinder with diameter d and length l_1 and the head as an ellipsoid with width w and length l_2. Then we get

$$\mathcal{N}^{\text{Approach II}}(L, W, d, l_1, w, l_2) = \frac{2}{3}\frac{LW^2}{d^2 l_1} + \frac{LW^2}{w^2 l_2}.$$

Applying the model we estimate the upper bound as

$$\mathcal{N}^{\text{Approach II}} = \frac{2}{3}\,\frac{185 \cdot (180)^2}{(2.2)^2 \cdot 180} + \frac{185 \cdot (180)^2}{(3.5)^2 \cdot 23} \approx 3700.$$

B.2.3 How the Sperm is fitted

If the sperm volume could be fitted perfectly in the spermathecae, according to our model there would be space for about 3700 sperm filaments. This is not the case since they are solid and there are spaces between filaments (filled with fluid).

To estimate how dense the filaments could be stuffed inside the spermathecae, we consider a pile of cylinders (e.g. tree trunks) stacked with aligned centerlines in every layer (Fig. B.4a). Then one would end up losing 13.4% of volume caused by spaces between the cylinders. Aligning them with alternating centerlines (Fig. B.4b) the loss is 9.3%. We included a third more realistic idea of how sperm is fitted inside a full spermathecae (Fig. B.4c, redrawn from Hosken et al. (1999)). From their observation a loss of around 15% is realistic.

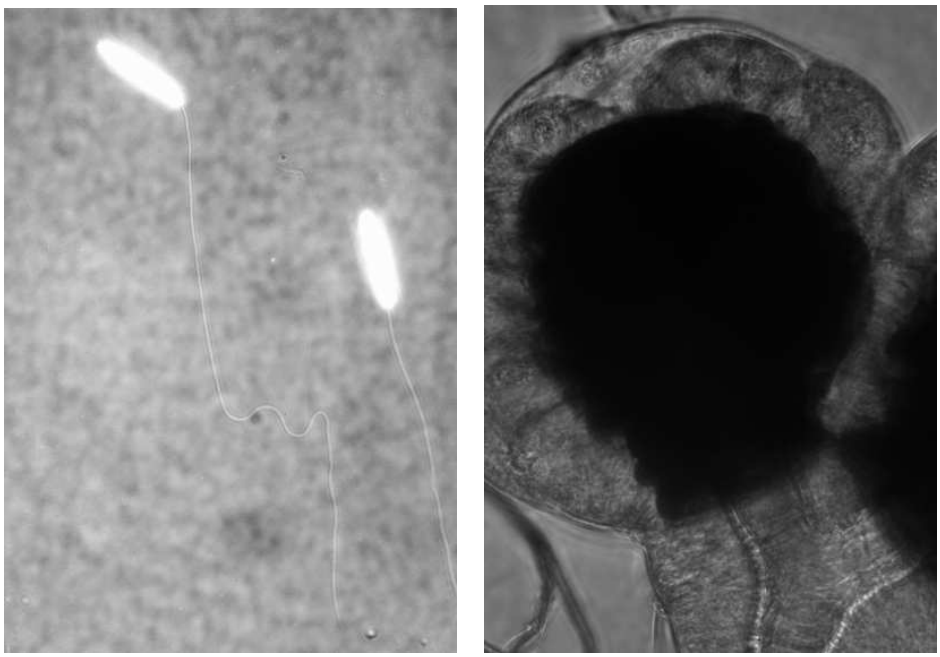

Figure B.3: A sperm filament (left) and a spermathecae (right) at the same spacial scale. The size of the head of the sperm is much smaller than shown (the glowing-like effect is caused to the marking substance and the fluorecent light).

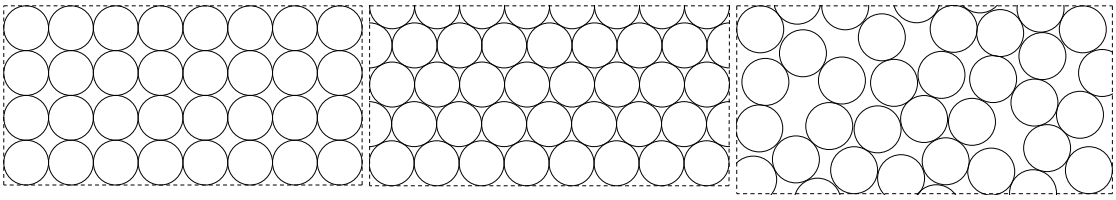

Figure B.4: Study on how sperm filaments are stuffed in a full spermathecae: (a) the centerline fit, (b) the optimal fit, (c) a realistic fit redrawn from Hosken et al. (1999).

We neglected the head shape and the fact that that the filaments are the spermatheca is an ellipsoid domain in these figures. This reduces the number in a magnitude of some percents. We conclude that due to our considerations a maximum of about 3000 sperm filaments fit in a single spermatheca. In the study in Chapter 5 we counted a maximum of 1798 sperm filaments in a single spermatheca. But due to the experiment outline, in 20 minutes the spermathecae just may not get filled entirely. Sbilordo et al. (2009) found an estimate of at least 4629 sperm contributed to the fertilization of the first clutch and 1406 sperm contributed to the fertilization of the second clutch from an experiment with multiple matings. Distributing these numbers to the three spermathecae, this leads to similar sperm numbers per spermatheca. Since sperm in such high number is hard to count approximately, the accordance of these theoretical and experimental findings contributes valuable knowledge for future experiments.

Bibliography

Amano, K. (1983). Studies of the interspecific competition in dung breeding flies. i. effects of larval density on the yellow dung fly. *Japanese Journal of Sanitary Zoology*, 34:165–175.

Andersson, M. (1994). *Sexual selection*. Princeton, N.J.: Princeton University Press.

Arnqvist, G. (1998). Comparative evidence for the evolution of genitalia by sexual selection. *Nature*, 393:784–786.

Arnqvist, G. and Rowe, L. (2002). Antagonistic coevolution between the sexes in a group of insects. *Nature*, 415:787–789.

Arnqvist, G. and Rowe, L. (2005). *Sexual conflict*. Princeton University Press.

Arthur, B., Sbilordo, S., Pemberton, A., and Ward, P. (2008). The anatomy of fertilization in the yellow dung fly *Scathophaga stercoraria*. *Journal of Morphology*, 269:630–637.

Baccetti, B., Dallai, R., and Rosali, R. (1970). The 9+3 flagellum of spider sperm cells. *Journal of Cell Biology*, 44:681–683.

Batchelor, G. (1967). *An introduction to fluid dynamics*. Cambridge University Press.

Bernasconi, G. and Hellriegel, B. (2002). Sperm survival in the female reproductive tract in the fly *Scathophaga stercararia* (L.). *Journal of Insect Physiology*, 48:197–203.

Birkhead, T. (1998). Criptic female choice: Criteria for establishing female sperm chioce. *Evolution*, 52:1212–1218.

Birkhead, T. (2000). Defining and demonstating postcopulatory female choice - again. *Evolution*, 54:1057–1060.

Blanckenhorn, W.U., A. B., Meile, P., and Ward, P. (2007). Sexual conflict over copula timing: a mathematical model and a test in the yellow dung fly. *Behavioral Ecology*, 18:958–966.

Brezzi, F. and Fortin, M. (1991). *Mixed and hybrid finite element methods*. Springer-Verlag, New York.

Buck, M. (2009). Modelling and simulation of biological filaments in channel flow. Master's thesis, Fachbereich Mathematik.

Bussière, L. F., Demont, M., Pemberton, A. J., Hall, M. D., and Ward, P. I. (2009). The assessment of insemination success in yellow dung flies using competitive PCR. *Molecular Ecology Resources*, in press.

Cameron, E., Day, T., and Rowe, L. (2003). Sexual conflict and indirect benefits. *Journal of Evolutionary Biology*, 16:1055–1060.

Ciarlet, P. (1978). *The finite element method for elliptic problems*. North Holland, Amsterdam.

Corley, L., Cotton, S., McConnell, E., Chapman, T., Fowler, K., and Pomiankowski, A. (2006). Highly variable sperm precedence in the stalk-eyed fly, Teleopsis dalmanni. *BMC Evolutionary Biology*, 6.

Cortez, R., Cowen, N., Dillon, R., and Fauci, L. (2004). Simulation of swimming organisms: Coupling internal mechanics with external fluid dynamics. *Computing in Science and Engineering*, 6:38–45.

Cox, R. (1970). The motion of long slender bodies in a viscous fluid. part 1., General theory. *Journal of Fluid Mechanics*, 44:791–810.

Darwin, C. (1859). *On the origin of species by means of natural selection*. London: John Murray.

Darwin, C. (1871). *The descent of man and selection in relation to sex*. London: John Murray.

Davis, T. (2004a). A column pre-ordering strategy for the unsymmetric-pattern multifrontal method. *ACM Transactions on Mathematical Software*, 30:165–195.

Davis, T. (2004b). Umfpack, an unsymmetric-pattern multifrontal method. *ACM Transactions on Mathematical Software*, 30:196–199.

Davis, T. and Duff, I. (1997). An unsymmetric-pattern multifrontal method for sparse lu factorization. *SIAM Journal on Matrix Analysis and Applications*, 18:140–158.

Davis, T. and Duff, I. (1999). A combined unifrontal/multifrontal method for unsymmetric sparse matrices. *ACM Transactions on Mathematical Software*, 25:1–19.

Dean, W. (1927). Note on the motion of fluid in a curved pipe. *Philosophical Magazine*, 20:208–223.

Dean, W. (1928). The streamline motion of fluid in a curved pipe. *Philosophical Magazine*, 5:673–695.

Eberhard, W. (1996). *Female control: sexual selection by cryptic female choice*. Princeton University Press, Princeton.

Eberhard, W. (2000). Criteria for demonstating postcopulatory female choice. *Evolution*, 54:1047–1050.

Girault, V. and Raviart, P.-A. (1979). *Finite element approximation of the Navier-Stokes equations*. Springer-Verlag, New York, Berlin Heidelberg New York.

Girault, V. and Raviart, P.-A. (1986). *Finite element methods for Navier-Stokes equations*. Springer-Verlag, New York.

Götz, T., Klar, A., Unterreiter, A., and Wegener, R. (2008). Numerical evidence for the nonexistence of stationary solutions of the equations describing rotational fiber spinning. *Mathematical Models & Methods in Applied Sciences*, 18:1829–1844.

Götz, T., Rave, H., Tiemeier, H., and Reinel-Bitzer, D. (2001). Simulation of the fiber spinnig process using parallel particle codes. part i: Fiber model and experiment. *Chemical Fibers International*.

Götz, T. and Unterreiter, A. (2000). An integral equation model for slender bodies in low reynolds-number flows. *Journal of Integral Equations and Applications*, 12:225–270.

Hackbusch, W. (1992). *Elliptic differential equations*. Springer Verlag, Berlin.

Hancock, G. (1953). The self-propulsion of microscopic organisms through liquids. *Proceedings of the Royal Society London A*, 217:96–121.

Hosken, D. (1999). Sperm displacement in yellow dung flies: a role for females. *TREE*, 14:251–252.

Hosken, D., Garner, T., and Ward, P. (2001). Sexual conflict selects for male and female reproductive characters. *Current Biology*, 11:489–493.

Hosken, D., Meyer, E., and Ward, P. (1999). Internal female reproductive anatomy and genital interactions during copula in the yellow dung fly, *Scatophaga stercoraria* (Diptera: Scathophagidae). *Canadian Journal of Zoology*, 77:1975–1983.

Hosken, D. and Ward, P. (2000). Copula in yellow dung flies (scatophaga stercoraria): investigating sperm competition models by histological observation. *Journal of Insect Physiology*, 46:1355–1363.

House, C. and Simmons, L. (2003). Genital morphology and fertilization success in the dung beetle onthophagus taurus: an example of sexually selected male genitalia. *Proceedings of the Royal Society B*, 270:447–455.

Kempenaers, B., Foerster, K., Questiau, S., Robertson, B., and Vermeirssen, E. (2000). Distinguishing between female sperm choice versus male sperm competition: A comment on birkhead (1998). *Evolution*, 54:1050–1052.

Kirkpatrick, M. and Barton, N. (1997). The strength of indirect selection on female mating preferences. *Proceedings of the National Academy of Sciences USA*, 94:1282–1286.

Laird, N. and Ware, J. (1982). Random-effects models for longitudinal data. *Biometrics*, 38:963–974.

Landau, L., Kosevich, A., and Lifshitz, E. (1996). *Theory of elasticity: Volume 7*. Butterworth-Heinemann.

Lewis, S. and Austad, S. (1994). Sexual selection in flour beetles - the relationship between sperm precedence and male olfactory attractiveness. *Behavioral Ecology*, 5:219–224.

Lighthill, J. (1975). *Mathematical biofluiddynamics*. Regional Conference Series in Applied Mathematics, SIAM.

Lowe, C. (2001). A hybrid particle/continuum model for micro-organism motility. *Future Generation Computer Systems*, 17:853–862.

Miller, G. and Pitnick, S. (2002). Sperm-female coevolution in drosophila. *Science*, 298:1230–1233.

Minder, A., Hosken, D., and Ward, P. (2005). Co-evolution of male and female reproductive characters across the scatophagidae (diptera). *Journal of Evolutionary Biology*, 18:60–69.

Parker, G. (1970a). Sperm competition and its evolutionary consequences in the insects. *Biological Reviews*, 45:525–567.

Parker, G. (1970b). Sperm competition and its evolutionary effect on copula duration in the fly *Scatophaga stercoraria*. *Journal of Insect Physiology*, 16:1301–1328.

Parker, P. and Simmons, L. (1991). A model of constant random sperm displacement during mating: evidence from *Scatophaga*. *Proceedings of the Royal Society B*, 246:107–115.

Parker, P. and Simmons, L. (1994). Evolution of phenotypic optima and copula duration in dungflies. *Nature*, 370:53–56.

Peskin, C. and McQueen, D. (1989). A three dimensional computational method for blood flow in the heart. i. immersed elastic fibers in a viscous incompressible fluid. *Journal of Computational Physics*, 81:372–405.

Pinheiro, J., Bates, D., DebRoy, S., Sarkar, D., and the R Core team (2009). *nlme: Linear and Nonlinear Mixed Effects Models*. R package version 3.1-92.

Pitnick, S. and Brown, W. (2000). Criteria for demonstrating female sperm choice. *EVOLUTION*, 54:1052–1056.

Presgraves, D., Baker, R., and Wilkinson, G. (1999). Coevolution of sperm and female reproductive tract morphology in stalk-eyed flies. *Proceedings of the Royal Society B*, 266:1041–1047.

Purcell, E. (1977). Life at low reynolds number. *American Journal of Physics*, 45:3–11.

R Development Core Team (2009). *R: A Language and Environment for Statistical Computing*. R Foundation for Statistical Computing, Vienna, Austria. ISBN 3-900051-07-0.

Rasband, W. (2009). *ImageJ: Image Processing and Analysis in Java*. `http://rsb.info.nih.gov/ij`.

Reinhardt, K., Harney, E., Naylor, R., Gorb, S., and Siva-Jothy, M. (2007). Female-limited polymorphism in the copulatory organ of a traumatically inseminating insect. *The Americal Naturalist*, 170:931–935.

Rowe, L. and Arnqvist, G. (2002). Sexually antagonistic coevolution in a mating system: Combining experimental and comparative approaches to address evolutionary processes. *Evolution*, 56:754–767.

Sbilordo, S., Schäfer, M., and Ward, P. (2009). Sperm release and use at fertilization by yellow dung fly females (scathophaga stercoraria). *Biological Journal of the Linnean Society*.

Schenk, O. and Gärtner, K. (2004). Solving unsymmetric sparse systems of linear equations with pardiso. *Journal of Future Generation Computer Systems*, 20:475–487.

Schenk, O. and Gärtner, K. (2006). On fast factorization pivoting methods for symmetric indefinite systems. *Electronic Transactions on Numerical Analysis*, 23:158–179.

Shelley, M. and Ueda, T. (2000). The stokesian hydrodynamics of flexing, stretching filaments. *Physica D*, 146:221–245.

Shewchuk, J. (1996). Triangle: Engineering a 2d quality mesh generator and delaunay triangulator. *Applied Computational Geometry*, 1148:203–222. `http://www.cs.cmu.edu/ quake/triangle.html`.

Shewchuk, J. (2002). Delaunay refinement algorithms for triangular mesh generation. *Computational Geometry: Theory and Applications*, 22:21–74.

Simmons, L., Parker, G., and Stockley, P. (1999). Sperm displacement in the yellow dung fly, *Scatophaga stercoraria*: an investigation of male and female processes. *The American Naturalist*, 153:302–314.

Simmons, L. and Parker, P. (1992). Individual variation in sperm competition success of yellow dung flies, *Scatophaga stercoraria*. *Evolution*, 46:366–375.

Simmons, L. and Siva-Jothy, M. (1998). *Sperm competition in insects: mechanismn and potential for selection*. Elsevier Science and Technology, UK.

Tornberg, A. and Shelly, M. (2004). Simulating the dynamics and interactions of flexible fibers in stokes flow. *Journal of Computational Physics*, 196:8–40.

Tregenza, T., Attia, F., and Bushaiba, S. (2009). Repeatability and heritability of sperm competition outcomes in males and females of Tribolium castaneum. *Behavioral Ecology and Sociobiology*, 63:817–823.

Turek, S. (1994). Tools for simulating nonstationary incompressible flow via discretely divergence-free finite element models. *International Journal for Numerical Methods in Fluids*, 18:71–105.

Ward, P. (2000). Cryptic female choice in the yellow dung fly *Scathophaga stercararia* (L.). *Evolution*, 54:1680–1686.

Ward, P. (2007). Postcopulatory selection in the yellow dung fly *Scathophaga stercoraria* (L.) and the mate-now-choose-later mechanism of cryptic female choice. *Advances in the Study of Behavior*, 37:343–369.

Wenninger, E. and Averill, A. (2006). Influence of body and genital morphology on relative male fertilization success in oriental beetle. *Behavioral Ecology*, 17:656–663.

Wilson, N., Tubman, S., Eady, P., and Robertson, G. (1997). Female genotype affects male success in sperm competition. *Proceedings of the Royal Society B*, 264:1491–1495.

Wüst, C. (2009). *JCFD: Custom flow simulation in Java*. `http://www.math.uzh.ch/compmath/jcfd`.

Yamamoto, S. and Takaaki, M. (1992). A method for dynamic simulation of rigid and flexible fibers in a flow. *Journal of Computational Physics*, 98:644–650.

Zhu, L. and Peskin, C. (2002). Simulation of a flapping flexible filament in a flowing soap film by the immersed boundary method. *Journal of Computational Physics.*, 179:452–468.